LEABHARLANN CHOLÁISTE NA TRÍONÓIDE, BAILE ÁTHA CLIATH | TRINITY COLLEGE LIBRARY DUBLIN
Ollscoil Átha Cliath | The University of Dublin

Terms and Conditions of Use of Digitised Theses from Trinity College Library Dublin

Copyright statement

All material supplied by Trinity College Library is protected by copyright (under the Copyright and Related Rights Act, 2000 as amended) and other relevant Intellectual Property Rights. By accessing and using a Digitised Thesis from Trinity College Library you acknowledge that all Intellectual Property Rights in any Works supplied are the sole and exclusive property of the copyright and/or other IPR holder. Specific copyright holders may not be explicitly identified. Use of materials from other sources within a thesis should not be construed as a claim over them.

A non-exclusive, non-transferable licence is hereby granted to those using or reproducing, in whole or in part, the material for valid purposes, providing the copyright owners are acknowledged using the normal conventions. Where specific permission to use material is required, this is identified and such permission must be sought from the copyright holder or agency cited.

Liability statement

By using a Digitised Thesis, I accept that Trinity College Dublin bears no legal responsibility for the accuracy, legality or comprehensiveness of materials contained within the thesis, and that Trinity College Dublin accepts no liability for indirect, consequential, or incidental, damages or losses arising from use of the thesis for whatever reason. Information located in a thesis may be subject to specific use constraints, details of which may not be explicitly described. It is the responsibility of potential and actual users to be aware of such constraints and to abide by them. By making use of material from a digitised thesis, you accept these copyright and disclaimer provisions. Where it is brought to the attention of Trinity College Library that there may be a breach of copyright or other restraint, it is the policy to withdraw or take down access to a thesis while the issue is being resolved.

Access Agreement

By using a Digitised Thesis from Trinity College Library you are bound by the following Terms & Conditions. Please read them carefully.

I have read and I understand the following statement: All material supplied via a Digitised Thesis from Trinity College Library is protected by copyright and other intellectual property rights, and duplication or sale of all or part of any of a thesis is not permitted, except that material may be duplicated by you for your research use or for educational purposes in electronic or print form providing the copyright owners are acknowledged using the normal conventions. You must obtain permission for any other use. Electronic or print copies may not be offered, whether for sale or otherwise to anyone. This copy has been supplied on the understanding that it is copyright material and that no quotation from the thesis may be published without proper acknowledgement.

Scanning Near-Field Microscopy of Microwave Circuits

A thesis submitted to the University of Dublin, Trinity College, in application for the degree of Doctor in Philosophy

by

Roman Kantor

Physics Department

Trinity College Dublin

October 2001

TRINITY COLLEGE
10 OCT 2002
LIBRARY DUBLIN
Thesis
6918

Declaration

This thesis is submitted by the undersigned for the degree of Doctor in Philosophy at the University of Dublin. It has not been submitted as an exercise for a degree at any other university.

Apart from the advice, assistance and joint effort mentioned in the acknowledgments and in the text, this thesis is entirely my own work.

I agree that the library may lend or copy this thesis freely on request.

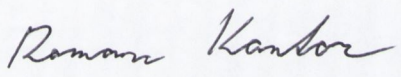

Roman Kantor

Acknowledgments

First, I would like to thank Prof. Igor Shvets for inviting me to join his excellent group and to work on an interesting project. I have enjoyed a lot of independence during past years but he was always here ready to help when something went worse. I am thankful for his support during those years.

Shane gave me a shelter after my arrival to Dublin and he still shares a house with me. He probably regrets that by now... I hope Dima, Sergei and Victor enjoyed our lunch discussions and philosophical arguments as much as I did (although it is difficult to have argument with Sergei!). I want to thank Anselm for his fabulous cakes, Vivienne for being so nice, William for his probes, Diadmaid for enjoying the spa wafers, Ciaran and Jurgen for their good mood, Luca for being Luca. And I "thank" Guido for permanently beating me in squash. A bunch of new guys - Sergio, Alex, Ken and Giuseppe - joined the group recently, I hope there will be soon an occasions to go for a pint...

My thanks go also to Michal, Nikolai and Michael for their help and contribution to the project. I am also very grateful to all the departmental staff: Tom, Marie, Michele, Susan, Elaine, John, Mick, James, Dave and others, without their everyday help we would be completely lost. I would like also to acknowledge my colleagues from my past work, especially Prof Pistora who supported my departure here.

My greatest thanks go to my family who always respected my decision whatever I have done. They have my deep love and respect.

Abstract

The topic of this thesis is the development and testing of measurement techniques for high resolution imaging of the field induced by microwave circuits in the near-field region. The theoretical aspects of the near-field acquisition are given and all alternative approaches to the practical realization of the measurement set-up are studied. The measurement system not only incorporates various instrumentation techniques used in Scanning Probe Microscopy (SPM) and microwave electronics but also incorporates new alternative techniques developed to solve the specific problems of the experiment.

The author has focused his attention on acquisition of electric field intensities induced by microwave devices. Using a microwave Vector Network Analyzer (VNA) both the amplitude and the phase of a microwave field are acquired by miniature coaxial antennas. High resolution probes were equipped with a low-noise preamplifier for efficient signal matching to the following microwave network. A new position-difference method for spatial resolution enhancement is theoretically analyzed and numerically verified using the Moment Method (MM). The effect of the resolution increase (down to about 10μm) is demonstrated on various samples and it is found that resolution achieved allows for inspection of most hybrid and many integrated circuits. Special antenna configurations are used for acquisition of all spatial components of the electric field vector. The probes are calibrated in a well-defined field standard to render quantitative description of the field intensities possible.

The scanning set-up combines motorized and piezo actuators for probe positioning. The measurement process consists of separate topography acquisition and field measurement during which the antenna is driven at specified distance above the sample surface. A newly designed topography probe

utilizes the Quartz tuning fork, commonly used in Scanning Near-Field Optical Microscopy for tip/sample separation control and which operates in the mode where a tip oscillates parallel or perpendicular to the sample surface. The topography probe allows relatively fast scanning (up to several hundreds μm/s) over rough surfaces with step-like structures. The measurement process is controlled by an in-house developed software which also allows the visualization and basic post-processing of the acquired data.

The system performance was tested on various microstrip circuits (transmission lines, filters, distributed capacitors) prepared by standard lithographic techniques for frequencies of 2-8 GHz, covering S-band and C-band communication ranges.

List of Figures

1.1 Measurement of the field intensities by small antennas 17

2.1 Radiation from a current element 22
2.2 Configurations of transmission lines 28
2.3 Field discribution above a coupled line in vertical configuration 31
2.4 Field distribution above a coupled line in the horizontal configuration 32
2.5 Field of surface charges 34
2.6 Microstrip transmission line configuration 37
2.7 Field of a microstrip transmission line 39
2.8 Contribution of the surface charge to the normal electric field intensity 41

3.1 Separate scanning of the sample topography and the field. . . 48
3.2 Standard configuration of SF tuning fork system. 50
3.3 Resonation of the tuning fork arms in standard configuration . 53
3.4 Single oscillating arm configuration 55
3.5 Resonance curve of the single oscillating arm configuration . . 56
3.6 Comparison of the tip appoach curves for standard and single oscillating arm configurations 57
3.7 Long-probe SF configuration 58

3.8 Shear-force interaction for a blunt tip 59
3.9 Influence of a surface water layer on the tip oscillation 60
3.10 Touching mode of the coupling of oscillations between the probe and the fork 62
3.11 Resonance and approach curves for touching more of oscillation coupling 63
3.12 Tapping mode of tuning-fork topography detection 64
3.13 Various interaction modes of taping SFM configuration 66
3.14 Schematics of the fork plug-in 70
3.15 Influence of the probe geometry and placement on the scanning speed 74
3.16 Topography tips and the antenna wire. 75

4.1 Short monopole antenna. 77
4.2 Electrical equivalent schematics of a short monopole 78
4.3 Electric antenna cross-section 80
4.4 Electric field antennas 82
4.5 The design of the antenna 85
4.6 Antenna response 86
4.7 Calibration units 87
4.8 Position-difference method. 89
4.9 Calculated and measured antenna signals above a cylindrical transmission line. 95
4.10 Dependency of the signal on antenna displacement 97
4.11 Probe configuration for measurement of all spatial components of the field 99

5.1 Design of the scanning system 102

5.2 Michelson interferometer and photo-detection circuit 104
5.3 Scanning control system schematics 107
5.4 Principle of the feedback function 109
5.5 Schematics of the feedback amplifier 110

6.1 Topography scan of an EPROM memory 114
6.2 Topography of a Lange coupler 115
6.3 Fast topography scanning of a silicon wafer with step structures. 116
6.4 Topography of a distrubuted PCB filter 118

7.1 Electric field of a microstrip transmission line 122
7.2 Distribution of the signals across the microstrip 123
7.3 Comparison of the measured field with calculated electric intensity 124
7.4 Topography of the capacitor 125
7.5 S_{11} scattering coefficient of the structure with a PCB capacitor 126
7.6 Effect of resolution enhancement for surface capacitor 128
7.7 Signal intensities across the fingers of the capacitor 130
7.8 Signal intensities across the signal feeding line of the capacitor 131
7.9 Fields of the capacitor for non-resonant excitation frequency . 132
7.10 Measurement of tangential field components 133
7.11 Field of a microstrip filter 135
7.12 Microstrip meander 136

A.1 Various antennas 141
A.2 Bias coupler design 142
A.3 DC bias coupler 143
A.4 Calibration units 144

A.5 User interface of scanning control software 145
A.6 Keypad for manual probe positioning 145
A.7 Scanning set-up 146

List of Tables

2.1 Field components of an infinitesimal dipole 23
2.2 Calculation of the fields of a coupled transmission line 29
2.3 Response functions of surface charges 35

4.1 Antenna components 80

Contents

1 Introduction **14**

1.1 Objectives of the work 14

1.2 State-of-the-art of microwave near-field measurements 15

2 Principles of near-field measurements **19**

2.1 Field of elementary sources 20

2.1.1 Fields of a short dipole 22

2.1.2 Electric intensity of oscillating charges 25

2.2 Models of circuit field sources 27

2.2.1 Two-wire transmission line of infinitesimal cross-section 27

2.2.2 Electric fields of surface charges 30

2.2.3 Microstrip transmission line 36

2.3 Recovery of the circuit signals 40

2.3.1 Single-layered planar circuits 40

2.3.2 Multi-layered circuits 44

3 Topography probe **46**

3.1 Shear-Force (SF) detector 49

3.1.1 Tuning fork SF oscillator 50

3.1.2 Single oscillating arm design 54

3.1.3 Touching geometry of oscillation coupling between the fork and the probe 60
3.2 Tapping mode scanning force distance control 63
3.3 Measurement of oscillation amplitude 67
3.4 Self-excitation regime of the tuning fork 68
3.5 Velocities of the probe motion 71
3.5.1 Stability of the feedback system 71
3.5.2 Scanning velocity 73
3.6 Topography tips 74

4 Electric field probes **76**
4.1 Short monopole antennas 76
4.1.1 Realization of the antennas 79
4.2 Sensitivity of the probes 82
4.2.1 Calibration of the antennas 84
4.3 Position-Difference (PD) method 88
4.3.1 Analysis of the position-difference method 89
4.3.2 Numerical and experimental verification of the method 94
4.4 Acquisition of tangential components of the field 96

5 Scanning set-up **101**
5.1 Probe displacement system 101
5.2 Scanning controller 105
5.2.1 Feedback amplifier 108
5.2.2 Scanning control and data visualization software 108
5.3 Scanning process 112

6 Topography acquisition **113**

7 Electric field intensity measurements **119**

7.1 Testing of the position-difference method 119

7.1.1 Fields of a strip line 119

7.1.2 Fields of a distributed PCB capacitor 121

7.2 Acquisition of tangential field components 129

7.3 Scanning of various samples 134

8 Conclusion **137**

8.1 Achieved results 137

8.2 Further work and improvement of the developed methods . . . 138

A Components of the scanning system **140**

Bibliography **147**

Chapter 1

Introduction

1.1 Objectives of the work

In recent decades the most significant advances in microwave technology were achieved in the development of solid-state devices and circuits. Rapid development of communication technologies is accompanied with the mass production of microwave devices. As miniaturization and low-cost production capabilities play a key role for their wide incorporation into various devices, high effort is put into the innovation of microstrip, hybrid and integrated circuits - the most common elements of communication systems.

The development of new complex microwave circuits is accompanied by a long and costly process of device testing and modifications. In many cases it is based only on the designers experience due to the lack of detail information about the device signals and the distribution of its electromagnetic field. Contemporary inspection systems of microwave circuits are usually based on the measurement of the signals on the device ports. Such measurements, in most cases only the measurement of the input and output signals, are not sufficient for characterization of the functionality of particular device subsystems. In

some cases special measurement pads are designed for direct probe coupling. Unfortunately their use is limited due to their relatively large contact areas and their influence on the circuit properties, caused by its relative high capacitance and cross-coupling with other circuit element. Additionally the load impedance of the measuring probes can change working regime of the circuits. These drawbacks effectively eliminate their use in highly miniaturized circuits - especially in MMIC (Monolithic Microwave Integrated Circuits). Due to the above mentioned reasons non-contact scanning near-field techniques may become an attractive method for circuit performance and failure testing. By analyzing the field distribution of working circuits one can evaluate not only signal coupling between circuit parts, the electromagnetic emissions of the device and other aspects of electromagnetic compatibility (EMC), but also to describe quantitatively the field sources (charges/potentials, currents)[1, 2] and the flow of the circuit signals.

1.2 State-of-the-art of microwave near-field measurements

The first demonstration of the field imaging with sub-wavelength resolution was performed by Ash and Nicholls [3]. They have used a small aperture to limit spatially the detected field, a resolution of $\sim \lambda/60$ was accomplished using microwave frequency 10 GHz. The experiment put a basis not only for sub-wavelength imaging at microwave frequencies but also in Scanning Near-Field Optical Microscopy (SNOM) where metal-coated optical fibers are mostly used for emission or collection of light. In the optical region, the tapered probes operate below the cut-off frequency resulting in a low transmission efficiency. Although various alternative probe configurations

were proposed to optimize their performance [4, 5, 6, 7, 8], for microwave frequencies conductive transmission lines (such as coaxial structures [9, 10]) are mostly used instead of waveguides with apertures to avoid the cut-off frequency limitation and for better signal matching to following microwave network.

The techniques used in scanning near-field microwave microscopy (SNMM) can be classified according to type of the source signal and the detectors used for the field acquisition. The microwave field can be generated by an external source and scattered from the sample in transmission or reflection mode, i.e. it can be generated by either the probe or the sample itself. As we will measure the field induced by active (working) microwave circuits, our considerations will be limited to the last case.

There are several possible approaches on how to detect the field induced by microwave devices or other samples. They differ by the configuration of the probes and the type of electro-magnetic interaction between the field source and the detector:

- use of aperture probes. In many cases modifications such as slit probes [11, 12] and open-ended transmission lines [13, 14] are used to increase signal matching efficiency.

- use of a metal tip to which the signal is coupled by electromagnetic interaction of the concentrated field between the sample and the sharp tip apex and by capacitance between the probe and the sample. These techniques have good resolution and much higher sensitivity than aperture probes.

- methods incorporating small antennas - short dipoles or monopoles [15] for electric field mapping and small loops [16, 17] for acquisition of a

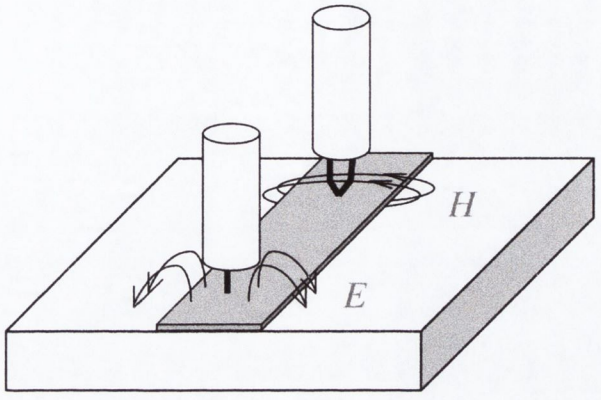

Figure 1.1: Measurement of the field intensities by small antennas

signal proportional to the magnetic field intensities. A modification of the method is a scattering technique when a modulated antenna impedance influences the sample field and the response of the circuit output signal modulation is detected [18, 19].

- electro-optical detection which can be also used for simultaneous mapping of the various spatial electric field components [20]

The methods incorporating a metal tip have a strong dependency of the level of the coupled signal on tip/sample separation. The probe distance must be precisely controlled utilizing a STM (Scanning Tunneling Microscopy) junction feedback [21], capacitive distance control with dual frequency excitation [22] or incorporation of a microwave feedback itself [23]. They are applicable for conductive samples only so their use is limited to the characterization of material properties such as resistance (or propagation losses) [24] and sample profile mapping [25, 26].

In this work we will focus on the third approach (Fig. 1.1) as this is the

only method which can lead to a quantitative field description. Additionally, the detection of electric and magnetic field intensities can be separated, measurement of the various spatial components becomes possible. Thanks to the linearity of the probes, the fields (and eventually their sources) can be characterized more precisely than using other methods. After conditioning the electric signal can be detected by a receiver (a spectrum analyzer or vector network analyzer) or by a diode detector on which the DC signal is measured. The main drawback of the method is the relative complexity of the probes which also incorporate a shielding to limit the active part of the antenna. The size of the probes is determined by the difficulties during their production resulting in limited antenna resolution. We increase the resolution of our probes by their miniaturization and also by special positioning techniques and antenna signal processing.

Chapter 2

Principles of near-field measurements

Because of the complexity of the general description of electromagnetic interaction between the field source and the receiver, in many cases the model of signal coupling is simplified by splitting the problem into two separate parts: description of the field induced by the source and the influence of that field on the receiving antenna. Such an approximation is appropriate as long as the mutual coupling between the source and the receiver is low and the influence of the receiving antenna on the transmitter (and its generation of the primary field) can be neglected. This is mostly the case with our field intensity measurements although we have to admit that this low coupling, which avoids the distortion of the circuit signals and the measured field, comes at the expense of lower levels of the detected signal.

2.1 Field of elementary sources

The excited electromagnetic field depends on the spatial distribution of the sources - electric currents and charges. As the field sources vary in time the system quantities can be transformed by Fourier analysis to the frequency domain and each frequency can be handled separately. This approach also suits our measurement methods as a single data set (for an image of the field distribution above the circuit) is taken for a particular microwave frequency and the measured results can be directly compared with quantities calculated for that frequency. The physical quantities can be written in harmonic form - i.e. $\mathbf{B}(t) = \mathbf{B} \cdot \exp(i\omega t)$ - and the time-dependent factor can be eventually removed from the formulas. Excluding static fields from our consideration we can directly link electric charges and current flow using the continuity theorem

$$\nabla \cdot \mathbf{j} + i\omega\rho = 0 \tag{2.1}$$

and both can be interchangeably taken as a source of the excited field. A convenient method for the field description is the use of scalar and vector potentials ϕ, $\mathbf{A}$ defined upon the Maxwell equations and vector identities $\nabla \cdot (\nabla \times \mathbf{A}) = 0$, $\nabla \times (\nabla\phi) = 0$ in the form

$$\mathbf{E} = -\nabla\phi - \frac{\partial \mathbf{A}}{\partial t} \tag{2.2}$$

$$\mathbf{B} = \nabla \times \mathbf{A} \tag{2.3}$$

For complete definition of vector potential $\mathbf{A}$ its divergence has yet to be specified. Thanks to this ambiguity a well-suited Lorentz condition can be introduced

$$\nabla \cdot \mathbf{A} = -i\omega\mu_0\epsilon_0\phi \tag{2.4}$$

which allows simplification of the wave equations for scalar and vector potentials, in a time-independent form also called the Helmholtz equations

$$\begin{aligned} \nabla^2\phi + \omega^2\mu_0\epsilon_0\phi &= -\frac{\rho}{\epsilon_0} \\ \nabla^2\mathbf{A} + \omega^2\mu_0\epsilon_0\mathbf{A} &= -\mu_0\mathbf{j} \end{aligned} \tag{2.5}$$

Using the Dirac unit impulse for the infinitesimal source normalization [28] the solution of these wave equations can be obtained as a collection of contributions of all elementary sources, the field potentials become the integrals over the source volume

$$\phi = \frac{1}{4\pi\epsilon_0}\int \frac{\exp(-i\beta r)}{r}\rho\, d^3r \tag{2.6}$$

$$\mathbf{A} = \frac{\mu_0}{4\pi}\int \frac{\exp(-i\beta r)}{r}\mathbf{j}\, d^3r \tag{2.7}$$

where $\beta = \frac{\omega}{c} = \omega\sqrt{\mu_0\epsilon_0}$ is the propagation constant and r is the distance away from the source location.

Note that neither the field sources (charges and current densities) nor the potentials themselves are independent physical quantities as they have to fulfill the continuity theorem (2.1) respectively Lorenz condition (2.4). This allows complete field description using a single vector function $\mathbf{A}$ from which both electric and magnetic intensities can be derived:

$$\mathbf{E} = -\nabla\phi - i\omega\mathbf{A} = -ic\left(\frac{1}{\beta}\nabla(\nabla\cdot\mathbf{A}) + \beta\mathbf{A}\right) \tag{2.8}$$

$$\mathbf{H} = \frac{1}{\mu_0}\nabla\times\mathbf{A} \tag{2.9}$$

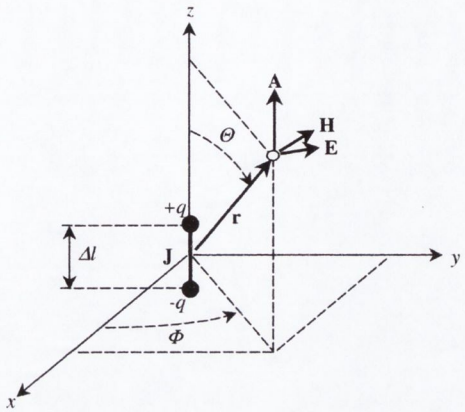

Figure 2.1: Radiation from a current element. The source can be defined by a current path $\mathbf{J}\Delta l$ or by a charge dipole $\mathbf{p} = q\Delta\mathbf{l} = -i\frac{\mathbf{J}}{\omega}\Delta l$

2.1.1 Fields of a short dipole

Using equations (2.8), (2.9) electric and magnetic field intensities of an infinitesimal current element can be explicitly derived. A convenient form to express the field components is the use of a polar coordinate system (see Fig. 2.1) for which many spatial components vanish. Table 2.1 includes not only the general field expression but also the formulas for the far-field approximation ($\beta r \gg 1$), the near-field and quasi-stationary approximations when $r \ll \lambda$. The propagation factor $e^{-i\beta r}$ can be further approximated in quasi-stationary region by taking only first two terms its expansion, $e^{-i\beta r} \simeq 1 - i\beta r$. In the table we have left its original exponential form to express better the phase retardation of propagating field.

Component	General expression	Far Field	Near-Field	Quasi-stationary
$d\mathbf{E}$	$\frac{e^{-i\beta r}}{4\pi\epsilon_0}\frac{1}{\beta c r^3}\left[-i\beta^2 r^2\left(\mathbf{r}_0\times\mathbf{j}\times\mathbf{r}_0\right)+\right.$ $\left.+\left(-i+\beta r\right)\left(3\mathbf{r}_0\left(\mathbf{r}_0\cdot\mathbf{j}\right)-\mathbf{j}\right)\right]$	$-\frac{e^{-i\beta r}}{4\pi\epsilon_0}\cdot$ $\cdot\frac{i}{cr^3}\beta\left(\mathbf{r}\times\mathbf{j}\times\mathbf{r}\right)$	$\frac{e^{-i\beta r}}{4\pi\epsilon_0}\frac{1}{\beta c r^3}\cdot$ $\cdot\left[\left(-i+\beta r\right)\left(3\mathbf{r}_0\left(\mathbf{r}_0\cdot\mathbf{j}\right)-\mathbf{j}\right)\right]$	$\frac{1}{4\pi\epsilon_0}\frac{i}{\beta c r^3}\cdot$ $\cdot\left(3\mathbf{r}_0\left(\mathbf{r}_0\cdot\mathbf{j}\right)-\mathbf{j}\right)$
$d\mathbf{H}$	$\frac{e^{-i\beta r}}{4\pi r^2}\left(i\beta r+1\right)\cdot\left(\mathbf{r}_0\times\mathbf{j}\right)$	$\frac{e^{-i\beta r}}{4\pi r}i\beta\cdot\left(\mathbf{r}_0\times\mathbf{j}\right)\Delta l$	$\frac{e^{-i\beta r}}{4\pi r^2}\left(i\beta r+1\right)\cdot\left(\mathbf{r}_0\times\mathbf{j}\right)$	$\frac{1}{4\pi r^2}\cdot\left(\mathbf{r}_0\times\mathbf{j}\right)$
dE_r	$\frac{\cos\Theta\, e^{-i\beta r}}{2\pi\epsilon_0}\frac{\beta^2}{c}\left(\frac{1}{\beta^2 r^2}-\frac{i}{\beta^3 r^3}\right)j$	0	$\frac{\cos\Theta\, e^{-i\beta r}}{2\pi\epsilon_0}\frac{\beta^2}{c}\left(\frac{1}{\beta^2 r^2}-\frac{i}{\beta^3 r^3}\right)j$	$-i\frac{\cos\Theta}{2\pi\epsilon_0}\frac{1}{\beta c r^3}j$
dE_Θ	$\frac{\sin\Theta\, e^{-i\beta r}}{4\pi\epsilon_0}\frac{\beta^2}{c}\left(\frac{i}{\beta r}+\frac{1}{\beta^2 r^2}-\frac{i}{\beta^3 r^3}\right)j$	$i\frac{\sin\Theta\, e^{-i\beta r}}{4\pi\epsilon_0}\frac{\beta}{cr}J\Delta l$	$\frac{\sin\Theta\, e^{-i\beta r}}{4\pi\epsilon_0}\frac{\beta^2}{c}\left(\frac{1}{\beta^2 r^2}-\frac{i}{\beta^3 r^3}\right)j$	$-i\frac{\sin\Theta}{4\pi\epsilon_0}\frac{1}{\beta c r^3}j$
dH_ϕ	$\frac{\sin\Theta\, e^{-i\beta r}}{4\pi}\beta^2\left(\frac{i}{\beta r}+\frac{1}{\beta^2 r^2}\right)j$	$i\frac{\sin\Theta\, e^{-i\beta r}}{4\pi}\frac{\beta}{r}j$	$\frac{\sin\Theta\, e^{-i\beta r}}{4\pi}\beta^2\left(\frac{i}{\beta r}+\frac{1}{\beta^2 r^2}\right)j$	$\frac{\sin\Theta}{4\pi}\frac{1}{r^2}j$
dE_ϕ, dH_r, dH_Θ	0	0	0	0

Table 2.1: Field components of an infinitesimal dipole. $r=|\mathbf{r}|$ is the lenth of the position vector between the source and the point of interest, $\mathbf{r}_0$ is the unit vector in that direction

In many cases an ideal electric dipole is used as a model of an elementary source. It can be derived from a small ($\Delta l \ll \lambda$,) current path with uniform amplitude along its length and represented by an infinitesimal wire conductor. The current causes charge accumulation at the ends resulting in the moment $\mathbf{p} = q\Delta\mathbf{l}$, the charges can be obtained using the continuity theorem (2.1) for which $q = -i\frac{1}{\omega}\int \nabla\mathbf{j}d^3r = -i\frac{J}{\omega}$. The induced vector potential, parallel to the dipole, can be directly expressed from (2.7) by substituting $\int \mathbf{j}d^3r = J\Delta\mathbf{l} = i\omega p$

$$\mathbf{A} = -i\omega\mu_0 \frac{\exp(-i\beta r)}{4\pi r} p \tag{2.10}$$

The formulas for the field intensities are analogous to the ones in table 2.1 and the quasi-stationary case of electric intensity is identical to the results obtained by the electrostatic Coulomb's law for a dipole of two point charges $+q$, $-q$ separated by a small distance Δl

$$E_r = p\frac{\cos\Theta}{2\pi\epsilon_0 r^3} \tag{2.11}$$

$$E_\Theta = p\frac{\sin\Theta}{4\pi\epsilon_0 r^3} \tag{2.12}$$

The relative phase difference between the electric and magnetic intensities in the stationary region is 90 degrees and they can be handled separately. The relation for a stationary magnetic field is usually written as a function of the current as it resembles the Biot-Savart law,

$$H_\phi = J\Delta l\frac{\sin\Theta}{4\pi r^2} \tag{2.13}$$

The electric and magnetic intensities in the far-field region, corresponding to the quantities proportional to term $1/r$, are coupled and their ratio is given

by the free space impedance

$$Z = \frac{E}{H} = \frac{1}{\epsilon_0 c} \doteq 377\Omega \tag{2.14}$$

The errors of the near-field approximations can be estimated by comparison of the terms proportional to r^{-1}, r^{-2} and r^{-3}. Operating at distances of about $\lambda/10^3$ with the area of contributing sources smaller than $\lambda/10^2$, the errors can be estimated below 0.25% for the near-field approximation and below 5% using the quasi-stationary model of the radiation of the sources. The real uncertainties caused by these approximations can be expected to be even smaller as the contribution of closer sources (with smaller errors) to the total field is larger than the contributions at the sources area boundaries.

2.1.2 Electric intensity of oscillating charges

In near-field region it is more convenient to express the solution for electric field intensity as a function of the charges - not currents. In accordance with the formulas in table 2.1 and limiting our consideration to stationary case each component of the electric intensity can be written in the form

$$E_x = \frac{1}{4\pi\epsilon_0} \int \frac{1}{\beta c} \left[\left(3\frac{x}{r^5}\mathbf{r} - \frac{\mathbf{x}_0}{r^3} \right) \cdot \mathbf{j} \right] d^3r \tag{2.15}$$

where $\mathbf{x}_0$ represents the unit vector of the x-coordinate. If we express

$$\nabla \left(\frac{x}{r^3}\mathbf{j} \right) = \nabla \left(\frac{x}{r^3} \right) \cdot \mathbf{j} + \frac{x}{r^3} (\nabla \cdot \mathbf{j}) = \left(-3x\frac{\mathbf{r}}{\mathbf{r}^5} + \frac{\mathbf{x}_0}{r^3} \right) \cdot \mathbf{j} + \frac{x}{r^3} (\nabla \cdot \mathbf{j}) \tag{2.16}$$

using continuity theorem (2.1) and substituting the term

$$\left(3x\frac{\mathbf{r}}{\mathbf{r}^5} - \frac{\mathbf{x}_0}{r^3} \right) \cdot \mathbf{j} = \frac{x}{r^3} (\nabla \cdot \mathbf{j}) - \nabla \left(\frac{x}{r^3}\mathbf{j} \right) \tag{2.17}$$

into (2.15) we get the electric intensity for x coordinate

$$E_x = \frac{1}{4\pi\epsilon_0}\int \frac{x}{r^3}\rho(\mathbf{r})d^3r - \frac{1}{4\pi\epsilon_0}\frac{1}{\beta c}\int \nabla\left(\frac{x}{r^3}\mathbf{j}\right)d^3r \tag{2.18}$$

The second integral in equation (2.18) can be transformed using Gauss-Osrtogradski theorem to the surface integral encapsulating the source volume

$$\int \nabla\left(\frac{x}{r^3}\mathbf{j}\right)d^3r = \oint \frac{x}{r^3}\mathbf{j}\,d\mathbf{S} = 0 \tag{2.19}$$

and it can be set to zero if we assume that all currents are limited to the source volume. Using similar formulas for other components we get eventually

$$\mathbf{E} = \frac{1}{4\pi\epsilon_0}\int \frac{\mathbf{r}}{r^3}\rho(\mathbf{r})d^3r \tag{2.20}$$

which resembles well known Coulomb's law of electrostatic field.

Note that we are allowed to use the stationary model under two important conditions: the sources are close enough so $\beta r \ll 1$ and there should be no external currents to fulfill (2.19). Obviously our microwave circuits are supplied by the external sources. Fortunately all those signals are coupled to the inspected region by balanced[1] transmission lines where each pair of conductors (or the main conductor and the grounding) carries opposite currents so that this condition is well satisfied.

This approximate formula provides important information about the character of the electric field close to the sources: the electric intensity depends on the particular result of circuit currents - the charge distribution, to a much lower degree it depends on the paths of the currents which influence

[1]The term "balanced line" is used here to express the current symmetry - not the symmetry of the potentials relative to a grounding as often used in radio and microwave engineering

only the far-field components. Because different configurations of the current lines may lead to a similar spatial distribution of charges, measurements of the electric intensities in near-field region provides information about those charges but poorly describes the currents themselves. To some extent the information about them may be retrieved by comparison of the measured data with full-wave electromagnetic field solutions for a particular configuration of circuit signal lines. In this way, by measuring the distribution of the electric field along uniform transmission line with known propagation laws, the signal currents may be also recalculated.

In some situations the static formulas match precisely the full-wave results. This is the case of straight conductors in homogeneous media guiding harmonic TEM waves such as straight wires, two-wire lines, coaxial transmission lines. In the following section we will use the stationary model to characterize the field of those transmission lines.

2.2 Models of circuit field sources

2.2.1 Two-wire transmission line of infinitesimal cross-section

Due to the high capacitances of the microwave circuit elements and radiation losses at high frequencies, all the signal transmission is carried by a pair of coupled lines: either balanced (such as coplanar strips and slot lines) where symmetric conductors carry electrical currents and potentials, or unbalanced ones (microstrips, coplanar waveguides) where the main conductor carrying the signal induces a secondary image of the currents and charges in the nearby grounding.

In many cases the field of non-symmetric lines can be solved using the

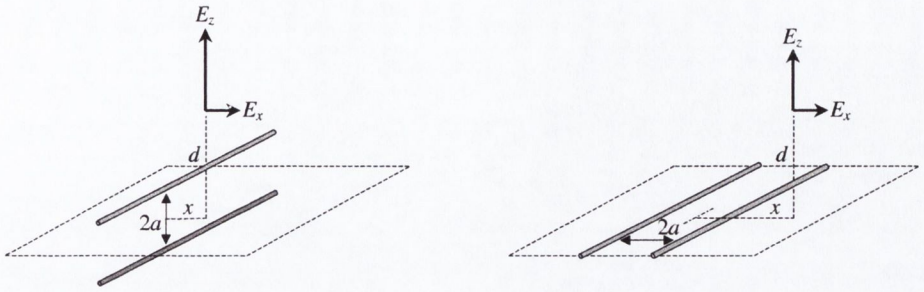

(a) (b)

Figure 2.2: Vertical (a) and horizontal (b) configurations of coupled transmission lines

method of images and represented by a symmetric configuration. This is the case for a uniform conductor placed at a distance a above a zero-potential ground. For the theoretical analysis of the surrounding field we will use a model of an ideal transmission line consisting of two wires separated by a distance a with infinite length and infinitesimal cross-section as presented in Fig. 2.2. We can use the quasi-static model with constant distribution of currents and charge density along the wire as it matches the full-wave solution with TEM harmonic waves propagating along the line. Two configurations - horizontal and vertical - are taken into account to cover the standard lines arrangement of planar circuits. The formulas for normal (z) and tangential (x) field components in quasi-stationary approximation are expressed in table 2.2.

	Finite distance $2a$	Infinitesimal separation $2a$
E_z	$q\frac{1}{2\pi\epsilon_0}\left(\frac{z-a}{x^2+(z-a)^2}-\frac{z+a}{x^2+(z+a)^2}\right)$	$2aq\frac{1}{2\pi\epsilon_0}\frac{x^2-z^2}{(x^2+z^2)^2}$
E_x	$q\frac{1}{2\pi\epsilon_0}\left(\frac{x}{x^2+(z-a)^2}-\frac{x}{x^2+(z+a)^2}\right)$	$2aq\frac{1}{2\pi\epsilon_0}\frac{2xz}{(x^2+z^2)^2}$
H_z	$I\frac{1}{2\pi}\left(\frac{x}{x^2+(z-a)^2}-\frac{x}{x^2+(z+a)^2}\right)$	$2aI\cdot\frac{1}{2\pi}\frac{-2xz}{(x^2+z^2)^2}$
H_x	$I\frac{1}{2\pi}\left(\frac{z-a}{x^2+(z-d)^2}-\frac{z+d}{x^2+(z+d)^2}\right)$	$2aI\cdot\frac{1}{2\pi}\frac{z^2-x^2}{(x^2+z^2)^2}$

Table 2.2: Field surrounding transmission line and its infinitesimal dipole approximation $d \ll l$ for vertical configuration as shown in Fig. 2.2 (a). The field distriburion for conductors placed horizontaly (Fig.2.2 b) can be obtained by permutation of the coordinates : $x' = -z$, $z' = x$.

Resolution limit

One of the primary goals of the circuit field mapping is localization and quantitative description of the signals. With increasing separation between the sample, the probe field intensity decay and spatial contrast decrease due to field dispersion. Figure 2.3 represents the field distribution of the electric and magnetic components above a transmission line in the vertical configuration, calculated according to the formulas in table 2.2. The dimensions of the field image scale directly to the probe distance and the width of the field maximum compares directly to the probe separation. This gives us an expected general rule for the measurement strategy: to achieve images of a certain resolution, the scan has to be performed at a probe distance comparable to or smaller than the desired resolution, $z \approx R$. On the other hand the field at higher distances is more homogeneous with a better defined probe response. Additionally, if the probe is too close to the sample its presence may cause redistribution of the circuit sources at immediate distances and distortion of the measured signals due to its influence on the circuit.

Figure 2.4 shows a two-wire line in the horizontal configuration and can be used as a model for various coplanar structures such as slot lines and coplanar waveguides. For a line separation exceeding the distance of the field probe ($a \gg d$, $a = 8d$ in the figure) the sources should be considered rather as separate lines and the infinitesimal dipole approximation is no longer valid.

2.2.2 Electric fields of surface charges

Microwave planar circuits consist of a single or several layers with conductive signal lines separated by dielectric films. We will describe one of the most common configurations, a single layered circuit with or without grounding.

The total field at a certain point $[x, y, z]$ above the circuit can be formally

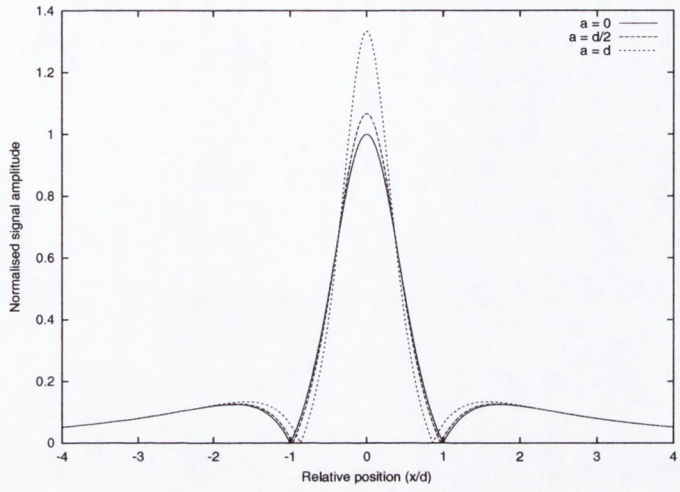

(a) E_z, H_x

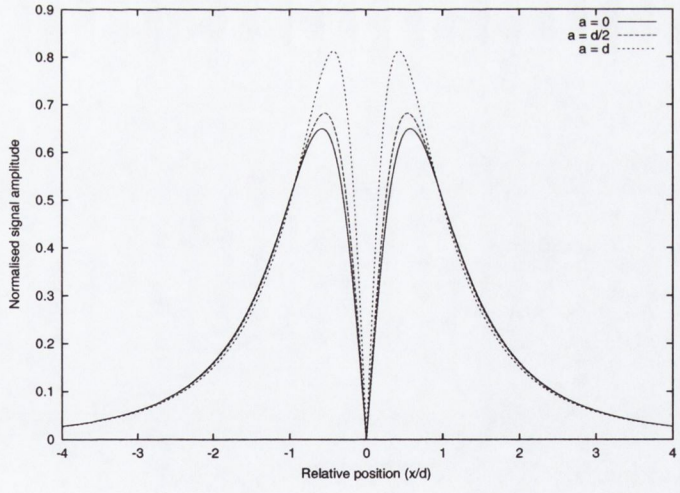

(b) E_x, H_z

Figure 2.3: Distribution of amplitudes of the normal and the tangential components of the electric and magnetic field intensensities for finite distances between the line wires and for infinitesimal wires sepparation for the vertical configuration. We see that the approximation causes an error lower than 0.3 dB for a wire separation of $a \leq d/2$ and less than 2 dB for $a \leq d$. The values of the tangential E_x and normal H_z components in (b) are normalised to their orthogonal counterparts in (a).

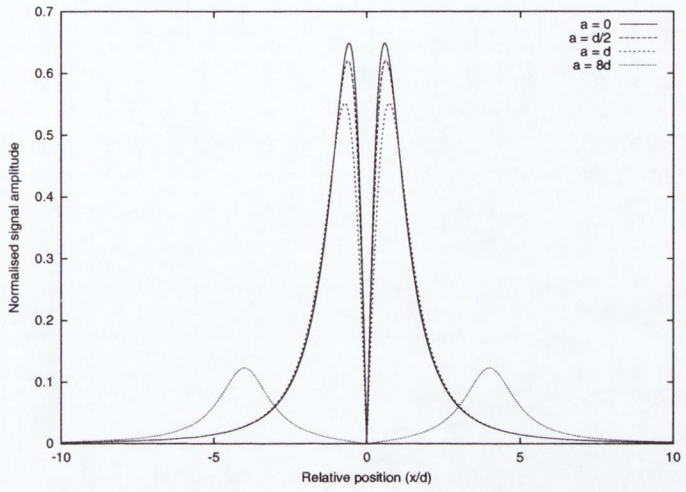

(a) E_z, H_x

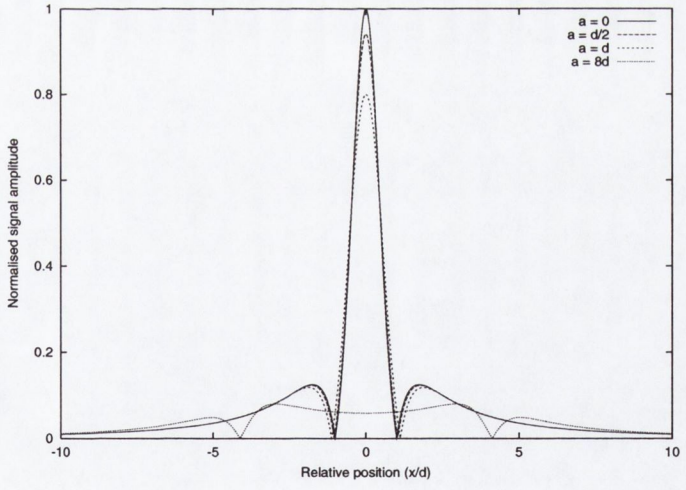

(b) E_x, H_z

Figure 2.4: Distribution of amplitudes of normal and tangential components of electric and magnetic fields for the horizontal configuration. The curves are complementary to these in Fig. 2.3 , the errors for the infinitesimal dipole approximation can be expected to be lower than 0.5 dB for a wire separation of $a \leq d/2$ and less than 1.5 dB for $a \leq d$.

written as an integral over the source area

$$F(x,y,z) = \int\int \mathcal{G}(x-x', y-y', z)\rho(x', y')\, dx\, dy \tag{2.21}$$

where $F(x,y,z)$ may represent any particular scalar or vector field quantity - potential ϕ or components of electric intensity $\mathbf{E}$. The function $\mathcal{G}$ - which has yet to be specified - is a corresponding weighting function and represents the contribution of an infinitesimal source to the total field for defined distance between the source and point of interest. If the charges would be located in free space the relation could be directly expressed using equation (2.20). In our case the charges induce the secondary field sources by polarization of the dielectric film and by the induction of the surface charges on the conductive grounding. The influence of these additional sources on the field can be described by their substitution with virtual charge images screened on the media boundaries. The position of the images can be obtained by multiple reflection of the original source at the interfaces as demonstrated in figure 2.5 for a single layered structure with grounding. Knowing the positions and quantities of the charge images the response functions can be expressed as a sum of the fields induced by those charges, table 2.3 summarizes the field calculation for three basic planar structures.

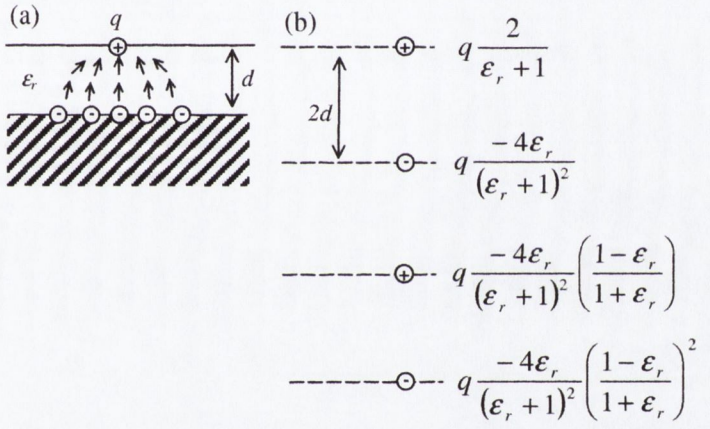

Figure 2.5: Field of surface charges. To describe the field above the substrate the real field sources (a) can be substituted by a serie of the charge images(b)

Configuration	Charge response function $\mathcal{G}$
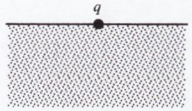 Dielectric surface	$\frac{2}{1+\epsilon}\mathcal{F}(x-x',y-y',z)$
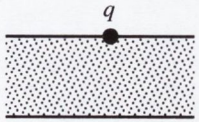 Dielectric slab	$\frac{2}{\epsilon_r+1}\left[\mathcal{F}(x-x',y-y',z)+\frac{2\epsilon_r}{1+\epsilon_r}\sum_{n=1}^{\infty}\left(\frac{1-\epsilon_r}{1+\epsilon_r}\right)^{2n-1}\cdot\mathcal{F}(x-x',y-y',z+a[n+1])\right]$
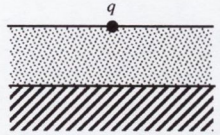 Dielectric slab with grounding	$\frac{2}{\epsilon_r+1}\left[\mathcal{F}(x-x',y-y',z)-\frac{2\epsilon_r}{1+\epsilon_r}\sum_{n=0}^{\infty}\left(\frac{1-\epsilon_r}{1+\epsilon_r}\right)^{n}\cdot\mathcal{F}(x-x',y-y',z+2a[n+1])\right]$
Field quantity	**Field function $\mathcal{F}$**
Intensity E_x, E_y, E_z	$\mathcal{F}^{Ez}(x,y,z)=\frac{y\cdot\left(x^2+y^2+z^2\right)^{-\frac{3}{2}}}{4\pi\epsilon_0}$, $\mathcal{F}^{Ey}=\frac{y\cdot\left(x^2+y^2+z^2\right)^{-\frac{3}{2}}}{4\pi\epsilon_0}$, $\mathcal{F}^{Ez}=\frac{z\cdot\left(x^2+y^2+z^2\right)^{-\frac{3}{2}}}{4\pi\epsilon_0}$
Potential ϕ	$\mathcal{F}^{\phi}(x,y,x)=\frac{1}{4\pi\epsilon_0}\left(x^2+y^2+z^2\right)^{-\frac{1}{2}}$

Table 2.3: Response function of surface charge for various structures. The field function $\mathcal{F}$ should be substituted with the expression presented at the bottom of the table.

In general it is impossible to express explicitly the field summation of an unbounded series in the presented formulas. In most cases the calculation can be limited to the first several charge images, the number of iterations depends on the dielectric permitivity. For high dielectric constant with strong charge reflections on the boundaries the number must be higher and the field sources are distributed in a wider area.

2.2.3 Microstrip transmission line

One of the most common types of transmission lines used for signal transmission in planar circuits is a microstrip - a uniform conductor separated from zero-potential grounding by a dielectric material (see Fig. 2.6). Microstrips are often used in all kinds of planar circuits due to their low production costs, relatively low transmission losses and low radiation. Possibility of integration with additional microwave elements - both shunt and distributed - and a relatively wide range of characteristic impedances makes them a good choice for application in hybrid and monolithic integrated circuits. A comparison of various guiding media can be found in [30].

Basic parameters characterizing the transmission line - its capacity C and inductance L per unit length (and its characteristic impedance $Z = \sqrt{L \cdot C^{-1}}$) can be used to express the signal transmission between the line ports - input and output. To describe the field distribution, a complete characterization of the microstrip is required with the width and thickness of the strip conductor, the permitivity and thickness of the dielectric, the line termination. Each line has to be solved individually, numerical methods have to be used (mostly FDTD - Finite Difference Time Domain) to find a full wave solution for the particular line configuration. Nevertheless for most strips with low characteristic impedance, including standard 50Ω lines

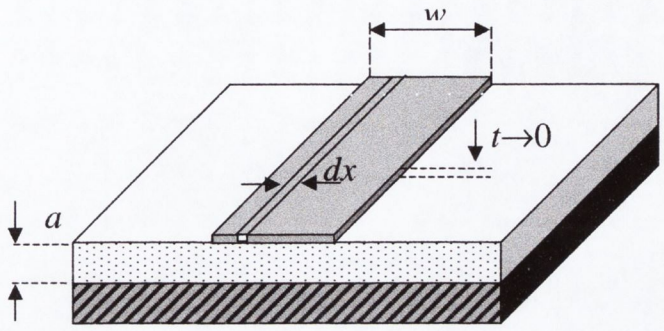

Figure 2.6: Microstrip transmission line configuration

and lines with losses [31], a quasi-TEM[2] (Transverse Electric and Magnetic) approximation can be used for two harmonic waves propagating in opposite directions along the line.

We will limit our consideration to lines with infinitesimal thickness $w \gg t$. To calculate the surrounding electric field we need to find the distribution of charges $\rho(x')$ across the line and then to calculate the field induced by those charges. We can use the method of images as presented in table 2.3 to express the induced field, the only difference is that for uniform distribution of the charges along the line we will define the source element as a small strip of infinite length and small width dx (see Fig. 2.6) for which the field functions will be

$$\begin{aligned} \mathcal{F}^{\phi} &= \frac{1}{2\pi\epsilon_0} \ln \left| \frac{\sqrt{x^2+z^2}}{r_0} \right| \\ \mathcal{F}^{Ez} &= \frac{1}{2\pi\epsilon_0} \frac{z}{\sqrt{x^2+z^2}} \end{aligned} \tag{2.22}$$

[2]The field can not be assumed as true TEM as the propagation factors in air and in the substrate dielectric differ which leads to the dispersion of the guided waves.

where the zero-potential level r_0 can be set equal to unity. To find the distribution of the charges across the strip it is necessary to find the solution of the electrostatic Poisson equation which in our case can be written

$$\int_{-\frac{w}{2}}^{\frac{w}{2}} \mathcal{G}^{\phi}(x - x', z = 0)\rho(x')dx' = \phi(x) = 1 \tag{2.23}$$

for any x in the interval $(-\frac{w}{2}, \frac{w}{2})$. The equation represents the boundary condition for the solution, the potential at the strip conductor has to be constant and can be set to unity. We have used the method of moments to numerically solve the equation (2.23). An example for the charge distribution of a typical 50Ω transmission line is shown in figure 2.7(a). Once the distribution is known the electric field can be calculated using equation (2.21). The figure 2.7(b) shows not only the induced normal component of electric intensity E_z but also the field of the strip approximated by an infinitesimal dipole line introduced in section 2.2.1. The total dipole moment of the strip can be calculated by a summation through the dipoles of all images,

$$p = \sum_n z_n q_n = \frac{2CU}{\epsilon_r + 1}\left[\frac{2\epsilon_r}{(1+\epsilon_r)^2}\sum_{n=0}^{\infty}\left(\frac{1-\epsilon_r}{1+\epsilon_r}\right)^n \cdot 2a\,(n+1)\right]$$

where total charge CU per unit length may be evaluated using known capacitance of the line and with approximate formulas found in many microwave handbooks [32, 33]. The approximation can be used only for distances significantly larger than the strip dimensions when the spatial distribution of the line can be neglected - i.e. for distance 700 μm in the figure b).

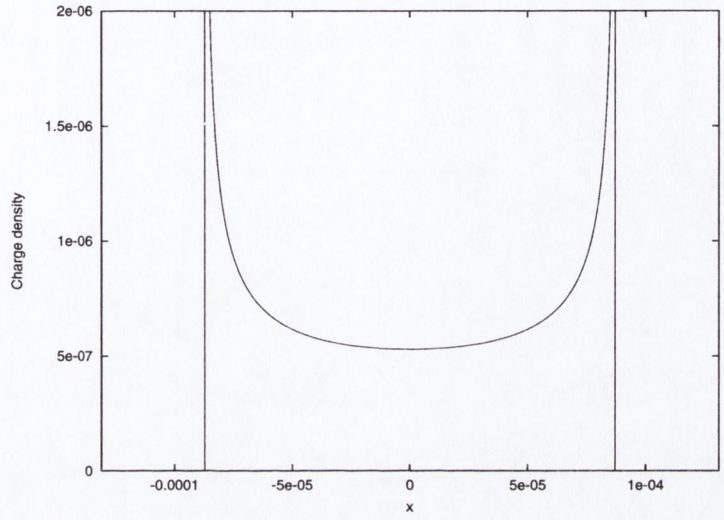

(a)

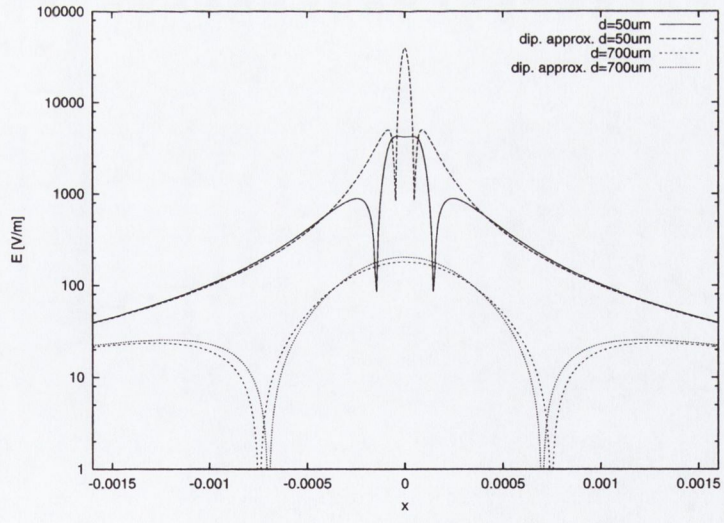

(b)

Figure 2.7: The charge distribution (a) and calculated normal electric field (b) of a 50Ω microstrip transmission line. Line width $w = 175\mu m$, dielectric thickness $a = 127\mu m$, relative permittivity $\epsilon_r = 6.15$.

2.3 Recovery of the circuit signals

Although the primary goal of the presented work is the development of methods for the measurement of induced fields, we would like to introduce one important aspect of the data post-processing: localization and quantitative description of field sources from a known field distribution as acquired during the scanning process. In many cases the position of the device signal lines and their basic parameters are known and comparison of the measured data with the calculated field - such as for models of transmission lines as introduced in the previous section - can be an appropriate method for the description of the circuit signals. For complicated structures with small separation between signal paths, when the sources contributing to the field can not be distinguished, a more general approach would be useful which would not rely on a particular model of the circuit structure.

2.3.1 Single-layered planar circuits

For many microwave circuits the signal lines are formed in the plane of the device and we can limit the source area to the device surface and the grounding. In the following we will describe one approach for the deconvolution of the field sources, a transformation of the image of the normal electric field component $E_z(x, y)$ (acquired during scanning at a distance z above the circuit) to the circuit surface charges.

The electric field intensity at any point $[x, y]$ and distance z above the surface can be expressed in accordance with (2.21)

$$E_z(x, y, z) = \int_{-\infty}^{+\infty} \int_{-\infty}^{+\infty} \mathcal{G}^{Ez}(x - x', y - y', z)\rho(x', y')dx'dy' \qquad (2.24)$$

where the weighting factor can be taken from table 2.3 for the particular

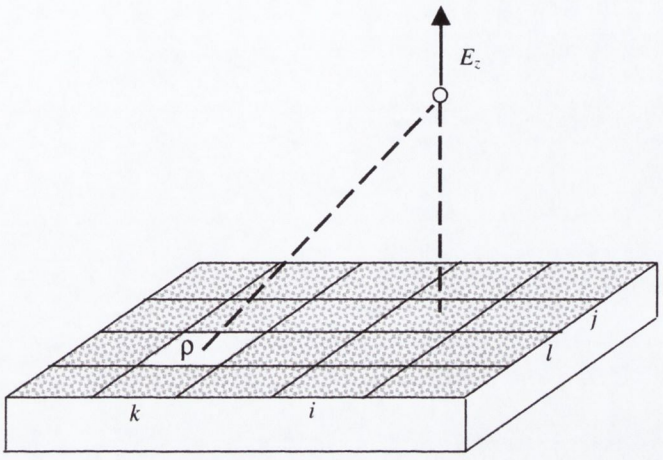

Figure 2.8: Contribution of the surface charge to the normal electric field intensity

substrate configuration.

As the field data $E_z(x, y, z)$ is acquired during the scanning process, to find the sources means to solve (2.24) for the surface charge density $\rho(x', y')$ in the form of an inverse transformation $\mathcal{G}^*$

$$\rho(x, y) = \int_{-\infty}^{+\infty} \int_{-\infty}^{+\infty} \mathcal{G}^*(x - x', y - y', z) E_z(x', y') dx' dy' \tag{2.25}$$

Unfortunately it is impossible to express explicitly $\mathcal{G}^*$and the equation (2.24) has to be solved numerically. A possible approach is to use the Moment Method (MM) to convert the integral equation (2.24) to a system of linear equations. If we denote $E_{i,j} = E_z(i \cdot \Delta x, j \cdot \Delta y, z)$ the discrete grid data obtained during the scanning process (Δx, Δy are the separations between scanned points and lines) and discretise the source area in the surface, we

can write equation (2.24) in the form

$$E_{i,j} = \sum_{k,l} \mathcal{G}^{Ez}_{i,j,k,l} \rho_{k,l} \tag{2.26}$$

where we assume homogeneous charge distribution $\rho_{k,l}$ for each segment area. The coefficients $\mathcal{G}_{i,j,k,l}$ have to be numerically integrated for segments close to the measured point when the distance r significantly varies between the segment boundaries,

$$\mathcal{G}^{Ez}_{i,j,k,l} = \int_{(l-j)\Delta y}^{(l-j+1)\Delta y} \int_{(k-i)\Delta x}^{(k-i+1)\Delta x} \mathcal{G}^{Ez}(x, y, z)\, dx\, dy \tag{2.27}$$

For $r \gg \Delta x$, $r \gg \Delta y$ these can be approximated

$$G^{Ez}_{i,j,k,l} \simeq \mathcal{G}^{Ez}([k-i]\,\Delta x, [l-j]\,\Delta y, z)\Delta x \Delta y \tag{2.28}$$

If we construct the field vector $\mathbf{E} = [E_{1,1},\ E_{1,2},\ \ldots E_{2,1},\ \ldots E_{n,m}]$ respectively the charge density vector $\mathbf{R} = [\rho_{1,1},\ \rho_{1,2},\ \ldots \rho_{m,n}]$ the tensor equation (2.26) can be written in matrix form

$$\begin{bmatrix} E_{1,1} \\ E_{1,2} \\ \cdots \\ E_{m,n} \end{bmatrix} = \begin{bmatrix} \mathcal{G}_{1,1,1,1} & \mathcal{G}_{1,1,1,2} & \cdots & \mathcal{G}_{1,1,m,n} \\ \mathcal{G}_{1,2,1,1} & \mathcal{G}_{1,2,1,2} & \cdots & \mathcal{G}_{1,2,m,n} \\ \cdots & \cdots & & \cdots \\ \mathcal{G}_{m,n,1,1} & \mathcal{G}_{m,n,1,2} & \cdots & \mathcal{G}_{m,n,m,n} \end{bmatrix} \cdot \begin{bmatrix} \rho_{1,1} \\ \rho_{1,2} \\ \cdots \\ \rho_{m,n} \end{bmatrix} \tag{2.29}$$

or simply

$$\mathbf{E} = \mathbf{G} \cdot \mathbf{R} \tag{2.30}$$

and its solution can be formally expressed as

$$\mathbf{R} = \mathbf{G}^{-1} \cdot \mathbf{E} \tag{2.31}$$

Knowing the distribution of the sources, the potential at the surface - and the circuit voltages - can eventually be calculated using the potential response function $\mathcal{G}^{\phi}$,

$$\begin{aligned} \phi(x, y, z = 0) &= \int\int \mathcal{G}^{\phi} \rho(x, y)\, dx'\, dy' \\ \phi_{i,j} &= \sum_{k,l} \mathcal{G}^{\phi}_{i,j,k,l} \rho_{k,l} \end{aligned} \tag{2.32}$$

Although the solution of the linear equation system (2.29) always exists, the precision and relevance of the calculated source distribution depends on the precision of the field measurements - including noise errors, uncertainties introduced by the source discretisation and approximation of Green's coefficients. Sometimes these errors can cause the presence of high spatial frequencies (comparable to the discretisation distances) in the calculated result. In some cases more advanced discretisation techniques for MM calculations can lead to stable solutions, i.e. use of overlapping source segments each with piece-wise triangular or sinusoidal distribution[28, p.450] to assure the continuity of the solution. Additional computational difficulties can be based on the size of the matrix and requirements put on computational resources. The amount of required computer memory and computational time (using the Gauss-Jordan method) is proportional to the number of matrix elements $\sim m^2 \cdot n^2$ and may be enormous even for relatively small scanning areas . To reduce these requirements the area contributing to the field of a particular point can be limited to distances comparable with the separation between the probe and the circuit, assuming that we can neglect the contribution of distant sources and all elements $G_{i,j,k,l}$ can be put equal to zero for $|i - k| \gg \frac{z}{dx}$ or $|j - l| \gg \frac{z}{dy}$. In such a case more effective algorithms, including iterative methods, can be used to solve the system of linear equation and take an

advantage from the reduced form of the matrix and its symmetry to avoid construction of the full matrix of all coefficients [34].

2.3.2 Multi-layered circuits

Many modern MMIC and hybrid circuits are formed by multi-layered conductors for which a slightly different approach has to be chosen to find the distribution of the device signals. In general it is impossible to localize the field sources in three dimensional space as equations (2.6), (2.7) do not have an unambiguous solution and some further assumptions should be taken for the form of the expected result. The possible approach is to limit the distribution of the signal sources, charges or currents, to the actual signal lines as the circuit geometry is known. If we discretise the charges along these lines and describe the variable source quantities as parameters $\mathbf{R} = [\rho_1, \rho_2, \ldots \rho_k]$, we can construct system of linear equations similar to the one of (2.29) and write

$$\begin{bmatrix} E_{1,1} \\ E_{1,2} \\ \cdots \\ E_{m,n} \end{bmatrix} = \begin{bmatrix} \mathcal{G}_{1,1,1} & \mathcal{G}_{1,1,2} & \cdots & \mathcal{G}_{1,1,k} \\ \mathcal{G}_{1,2,1} & \mathcal{G}_{1,2,2} & \cdots & \mathcal{G}_{1,2,k} \\ \cdots & \cdots & & \cdots \\ \mathcal{G}_{m,n,1} & \mathcal{G}_{m,n,2} & \cdots & \mathcal{G}_{m,n,k} \end{bmatrix} \cdot \begin{bmatrix} \rho_1 \\ \rho_2 \\ \cdots \\ \rho_k \end{bmatrix} \tag{2.33}$$

where response the coefficients $\mathcal{G}_{m,n,i}$ depend on the position of the measuring point relative to the source. The coefficients should include the influence of the polarisation of the materials and - if present - the influence of the conductive grounding. For planar multilayered structures the response coefficients may be again calculated using method of charge images and their multiple screening - similar to that presented in section 2.2.2. The existence and precision of the solution of the linear equations (2.33) depends not only on the precision of the measured intensities E, but also on the rank of the

matrix of the system. To find the solution, this rank should be theoretically equal to k and the number of measured points must exceed or be equal to the number of the discrete sources, $m \cdot n \geq k$. In practice, the discretisation errors and approximations of the response coefficients causes the rank to be virtually equal to $k + 1$ (if $m \cdot n > k$) and the result is normally calculated using optimisation methods, such as looking for a solution for ρ_i to minimise the term

$$\sum_{i,j} \left| E_{i,j} - \sum_{k} \mathcal{G}_{i,j,k} \rho_k \right|^2 \tag{2.34}$$

The relevance of obtained solution depends not only on the precision of the measured field but also on the distribution of measured points relative to the sources and the orthogonality of the system of equations. In general, the measurement of the field very close to the sources and covering the whole source area helps to assure the independency of the equations in the system. In some cases, measurement of the field components paralel to the surface (see sections 4.4, 7.2) can help to find more precise solution if the field induced above the circuit have strong tangential conponents.

Chapter 3

Topography probe

To accomplish high resolution of field imaging the antenna must be driven with high precision close to the circuit surface. The standard approach of microwave near-field measurements - horizontal plane scanning at a defined constant level [1, 15, 14] - can not be implemented with sufficient precision for highly miniaturized circuits. The small tip sample separation d=1-100 μm can not be kept constant for such scanning when the sample tilt and the size of circuit features is comparable or exceeds the working distance. This is the case of step-like profile of the transmission lines, various shunt elements and other surface features like air bondings, signal contacts etc.

The methods utilizing microwave signal acquisition with simultaneous tip-sample distance control, such as Scanning Tunneling Microscopy (STM) junction [21], capacitive distance control using dual frequency excitation [22] or incorporation of a microwave feedback for distance control [23, 24] are applicable for conductive samples only and their use is limited to the material property and sample profile mapping [25, 26].

The topography acquisition methods incorporated in scanning force microscopy (SFM) and related techniques are based on measurement of the de-

flection of a cantilever in contact with the sample or on the detection of the interaction between an oscillating probe and the sample surface [38, chap. 2]. The probe can oscillate parallel (as used in SNOM) or perpendicular (AFM) to the sample. Close to the sample surface the forces acting on the tip influence both the amplitude and the phase of the mechanical vibrations. The monitored signal can be used in the positioning feedback for the probe to keep the level of the signal and acting forces constant. The attraction of these methods is their good resolution and the fact that they are relatively independent of the particular optical or electrical properties of the surface studied and they can also work with all the common materials used in microwave circuits - conductors, semiconductors and dielectric materials. Some of these methods take advantage of the simultaneous acquisition of the topography together with an additional measured quantity: optical intensity in SNOM or electric field signals in scanning capacitance microscopy (SCM) and scanning resistance microscopy (SRM), which are particularly useful for characterization of semiconductor materials and devices [36, 37]. Unfortunately, the range of the probe/sample interaction is limited and in most cases does not exceed a few tens of nm and may significantly vary during the scanning process, occasionally leading to direct contact between the probe and the sample. This does not allow simultaneous measurement of the microwave field. For such a probe separation strong capacitive coupling between the antenna and the circuit conductors would cause significant distortion of the signal resulting from the measured electric intensity. This makes it necessary to split the measurement process into two separate steps (see Fig. 3.1):

- sample profile acquisition
- field probe scanning when the antenna is driven according to the previously acquired topographic data at defined distance above the surface.

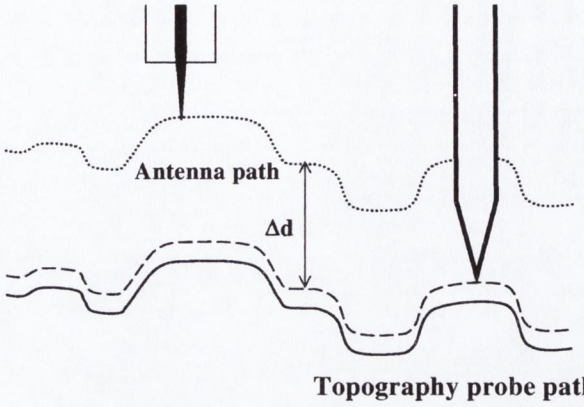

Figure 3.1: Separate scanning of the sample topography and the field.

There are two ways to perform such a measurement:

- both scans are acquired with the same probe where an additional position offset between the scans is applied
- different detectors for topography acquisition and field measurements are used. After topography acquisition, the probe is exchanged for the field antenna and precisely aligned to the position of the previous probe.

We have studied both possible approaches, only the second one was eventually realized. Although the use of different probes is more demanding on the set-up instrumentation and the precision of measurement process, separate probes for SFM topography and field acquisition permits the optimization of each probe design with respect to their different functions.

3.1 Shear-Force (SF) detector

Shear-force detection [41, 42] is commonly used as the key method for sensing the probe-sample proximity in near-field optical microscopy. It is based on exciting probe oscillations by a dithering piezo parallel to the surface and monitoring their dependence on the probe-sample separation. A dissipative interaction between the sample and the probe damps the oscillations. The detection of the oscillations can be performed optically when a laser beam strikes the probe and the shadowed or reflected light intensity is measured by a photo-diode [41, 43]. Alternative interferometric methods may be used to increase the detection sensitivity and to avoid the collision of the feedback reference beam with the sample [44, 45].

As all these optical methods require precise adjustment of relatively complex instrumentation, various non-optical methods were introduced to detect the probe motion, to simplify the system design and to circumvent the above mentioned issues. These methods include for example the piezoelectric tuning fork oscillator [46, 47], the detection of a voltage induced in a secondary piezo element glued to the holder [48] or directly to the fiber. Other instruments measure the influence of the probe vibrations on a capacitance detector [49] or directly measure the capacitance change of the dithering piezo with a Wheatstone bridge [50, 51].

The importance of the light-weight design of the topography probes in our system arises from the fact that all the scanning movement must be performed by the probe - not the device under testing. The microwave circuits with their plug-in cables, their housing, cooling systems etc., are relatively heavy and can not be actuated by piezos with adequate efficiency during the scanning process.

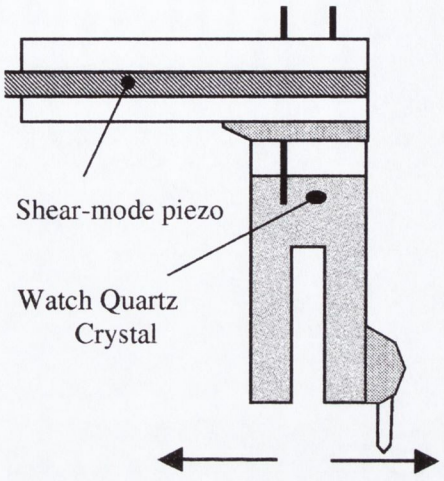

Figure 3.2: Standard configuration of SF tuning fork system.

3.1.1 Tuning fork SF oscillator

The preliminary testing of various non-optical configurations indicated the superiority of the method utilizing a Quartz tuning fork crystal, commonly used in digital watches. The method was introduced by Karrai and Grober [46]. Its good sensitivity and relative simplicity of design made it a good candidate for incorporation in our scanning system. We have focused our attention on the further improvement of this method - especially on reducing relatively long time constant of the relaxation processes which limits the speed of shear-force feedback system.

In the original design the fork base is glued to a piezo, which is excited at the main resonance frequency of the fork (see fig. 3.2). The probe - an optical fiber - is glued to one of the arms and it protrudes from the end of the fork by only 1-2 mm. Its own resonance frequency is higher than the one of the fork, so the employed resonance is that of the tuning fork. The system

can be described by a model of coupled linear oscillators

$$m\frac{d^2y_1}{dt^2} + b\frac{dy_1}{dt} + k\left(y_1 - y_2\right) = -F\exp\left(i\omega t\right) \tag{3.1}$$

$$\left(m + m_t\right)\frac{d^2y_2}{dt^2} + \left(b + b_t\right)\frac{dy_2}{dt} - k\left(y_1 - y_2\right) = F\exp\left(i\omega t\right) \tag{3.2}$$

where m is effective mass of the free arm, b is its damping coefficient, k is the effective spring constant of the arms for the mode of interest, F describes influence of excitation forces on the system. The actual values of m, k can be calculated by modeling the transverse vibrations of a fixed beam [52, p. 495]. Using Young's modulus of quartz ($E = 7.87 \cdot 10^{11}\,\mathrm{N/m^2}$) and the dimensions of the prongs of our forks we get $m = 2.5 \cdot 10^{-7}$ kg, $k = 5370\,\mathrm{N/m}$. The influence of a probe glued to one arm is represented by an additional mass m_t and probe/sample interaction by a damping coefficient b_t. The force F here is not the complete exciting force acting on the fork but rather a difference between the two forces acting on the arms. Such a difference is essential to excite the main resonance mode where the arms oscillate with opposite phase, the forces between the two arms are much larger than the ones between the fork and the holder[1]. Substituting $m\frac{dy_1}{dt} = \left(m + m_1\right)\frac{dy_2}{dt}$, $m\frac{d^2y_1}{dt^2} = \left(m + m_1\right)\frac{d^2y_2}{dt^2}$ and $my_1 = \left(m + m_1\right)y_2$ in the difference of equations (3.1), (3.2) we get

$$2\left(m + m_t\right)\frac{d^2y_2}{dt^2} + \left[2b\left(1 + \frac{m_t}{2m}\right) + b_t\right]\frac{dy_2}{dt} + 4k\left(1 + \frac{m_t}{2m}\right)y_2 = F\exp\left(i\omega t\right) \tag{3.3}$$

[1]This is actually the principle of all tuning fork oscillators: for opposite phase of the oscillation of the arms the forces between the whole system and the holder are $\frac{dp}{dt} = 0$ so there are no elastic deformations of the system attachment and with low damping the quality factor remains high.

Its solution gives us the resonance frequency

$$\omega_0 = \sqrt{\frac{k'}{2\left(m + m_t\right)}} \tag{3.4}$$

where we have used the symbols $k' = 4k\left(1 + \frac{m_t}{2m}\right)$ for modified spring constant.

The influence of the same tip/sample interaction forces is reduced in (3.3) due to the fact that the damping forces also attenuate the vibration of the second arm without the tip. For the main resonance frequency this free arm oscillates with a larger amplitude than the arm with the tip

$$y_1 = \frac{m + m_t}{m} y_2 \tag{3.5}$$

and also accumulates more energy than the one with the tip. We have optically measured the oscillations by detecting a laser beam intensity partially shadowed by the vibrating arms (see Fig 3.3). The ratio of the amplitudes was 1:4.

The relevance of the mathematical model is based on the assumption of anti-phase oscillations of the arms to fulfill the condition of zero total momentum. We have measured the phase difference (the dashed line in figure 3.3) between the arms and for the main resonance mode of 31130 Hz frequency, the results correspond very well to our assumption. One can also excite modes below 28 kHz for which the two arms oscillate in phase, however these modes are highly sensitive to the way the fork is glued, the kind of glue used etc. Additionally such modes are not well detectable as the piezoelectric signal corresponds to the difference between the arms.

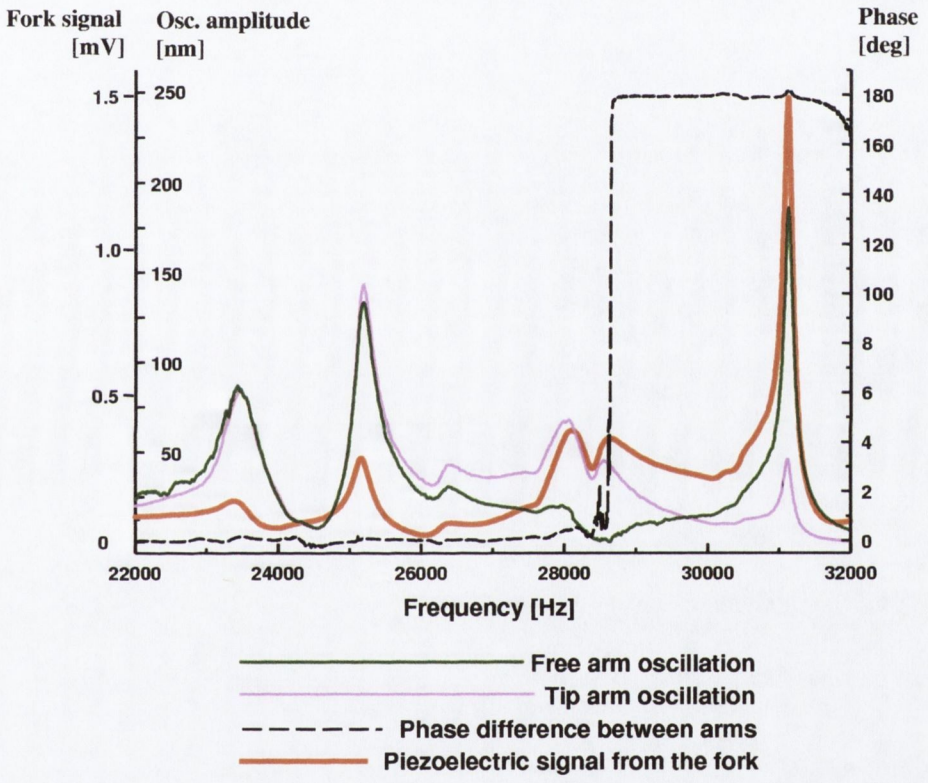

Figure 3.3: Resonation of the tuning fork arms in standard configuration $\omega_0 = 31\,130$ Hz, $Q = 510$.

3.1.2 Single oscillating arm design

The approach we have adopted to reduce the response time is to reduce the mass of the oscillating system and to excite the oscillations in just one arm of the fork, keeping the other arm glued to a stiff heavy base (Fig.3.4). The mathematical model of this oscillator is simpler than in the previous case,

$$(m + m_t)\frac{d^2y}{dt^2} + (b + b_t)\frac{dy}{dt} + ky = F\exp(i\omega t) \tag{3.6}$$

where the constants m, m_t, b, b_t, k correspond to the ones introduced previously. The resonance frequency is simply $\omega_0 = \sqrt{\frac{k}{(m+m_t)}}$, the quality factor for free oscillations - without interaction of the tip with the sample - is $Q_{max} = \frac{\sqrt{k(m+m_t)}}{b}$ and both these parameters can be obtained by measuring the resonance curve. For our probe the resonance frequency was $\omega_0 = 26\,200$ Hz which drops more due to additional mass m_t than in previous configuration, where it was more influenced by the free arm oscillation and much closer to the original resonance of watch quartz crystal 32768 Hz.

The tip approach curves for both configurations are compared in figure 3.6. Although we can not completely eliminate the possibility of the influence of the shape of the tip apex, we have tried to reduce this factor by using similar tips with apex radii about 0.5 μm. The width of the interaction zone is similar in both cases, although the shapes of the curves slightly differ. The improved design is more responsive as the dissipative interaction forces have to damp the vibrations in one arm only. For each point of the curve the quality factor can be calculated as $Q \simeq \frac{y}{y_{max}}Q_{max}$ and the corresponding relaxation time is $\tau = \frac{Q}{\omega_0}$. In our case the reduction was about 3 times, to about $\tau = 0.8$ ms for free oscillations without the tip/sample interaction. An additional advantage of the improved design is the fact that the detected

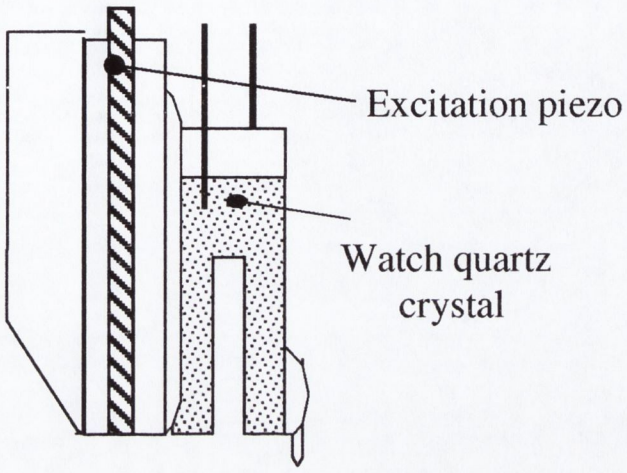

Figure 3.4: Single oscillating arm configuration

signal directly corresponds to the tip vibration - not the oscillations of the whole system. This is especially important when the tip rapidly approaches the sample, where, in the double-arm design, slowly damped signal coming from the oscillations of the arm without the tip does not allow the position feedback to react, even if the arm with the tip is already in contact with the sample. The resulting collision may cause significant damage to the tip.

We have also tried to further reduce the effective mass of the oscillator by exciting the vibrations in a longer free fiber tip [54] and use the fork piezoelectric response rather as a vibration detector only (see figure 3.7). We have removed the plastic jacket from the optical fiber to reduce the damping, the quality factor and estimated ratio between the amplitudes was Q =350. Although this technique is useful for detection of small drag forces in the tip/sample interaction (up to 10^{-11}N), it requires long time constants (more than 10ms) for phase-locked signal detection due to the lower level of piezo-

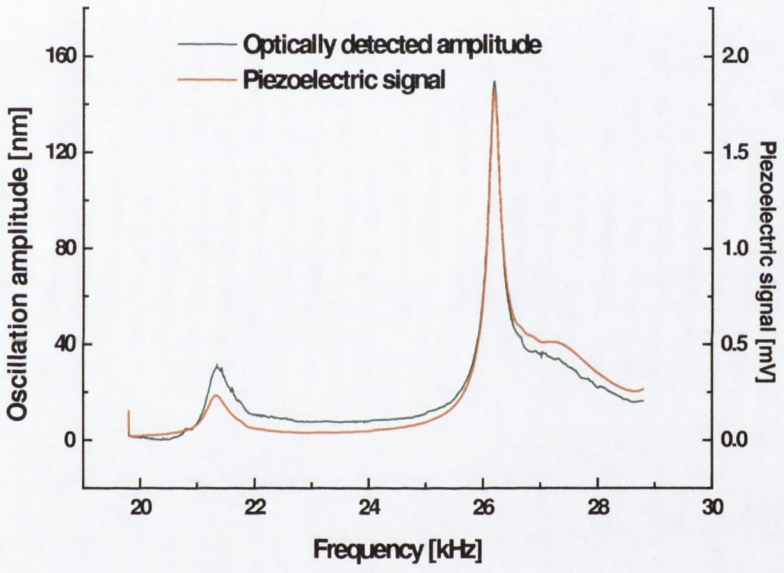

Figure 3.5: Resonance curve of the single oscillating arm configuration, $\omega_0 = 26\,200$, $Q_{max} = 130$

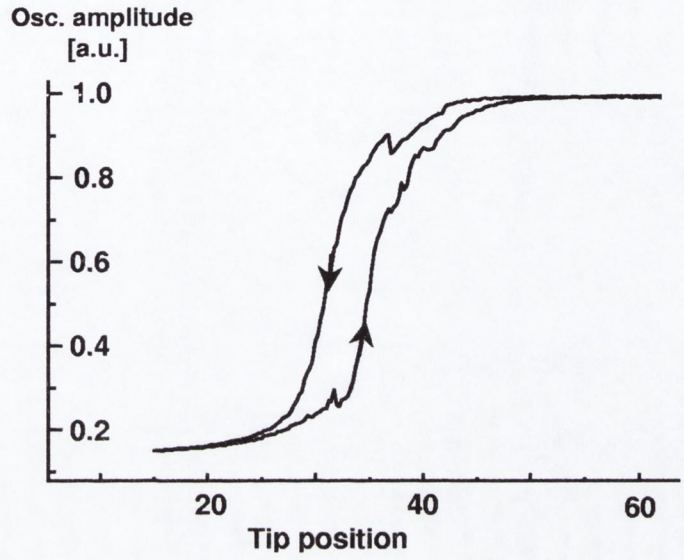

(a)

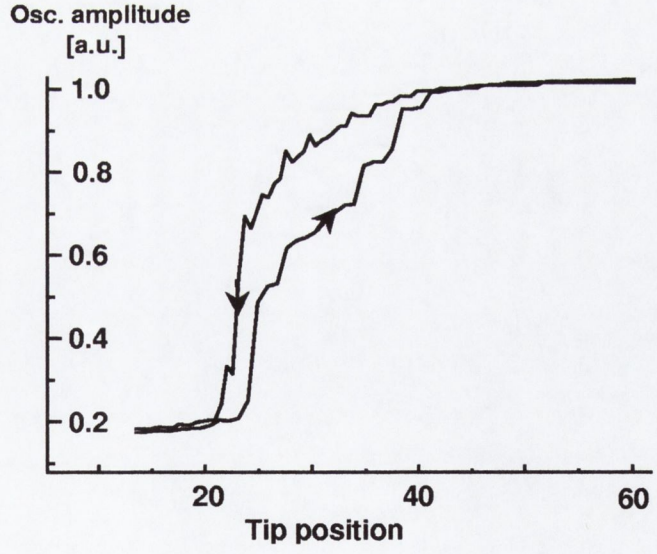

(b)

Figure 3.6: Comparison of the tip appoach curves for standard (a) and single oscillating arm (b) configurations. The sample was Si single crystal structure, tip radius was about 0.5 μ m. The primary amplitude in both cases is 25nm.

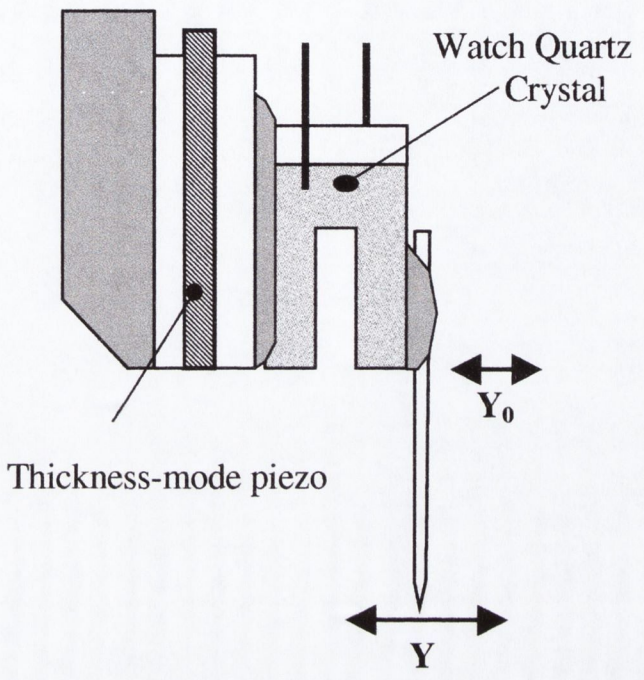

Figure 3.7: Long-probe SF configuration. The system is excited at the tip own resonance frequency ($\omega_0 = 7555$Hz) and its vibration is detecterd by the residual movement of the fork arm. The ratio between the tip apex amplitude Y and the arm oscillation can be calculated from the solution of the harmonic oscillator, $\frac{Y}{Y_0} \doteq Q$.

electric response as the fork arm oscillates with a much lower amplitude than the tip apex.

The character of the forces strongly depends on the shape of the tip apex and the material of both the tip and the sample. Figure 3.8 shows the approach curves for a blunt tip (the apex radius approximately $3\mu m$) and a silicon substrate, with and without a gold layer. We can observe large difference between the approach and withdrawal curves.

The exact nature of so-called shear-forces is still unclear but they seem to

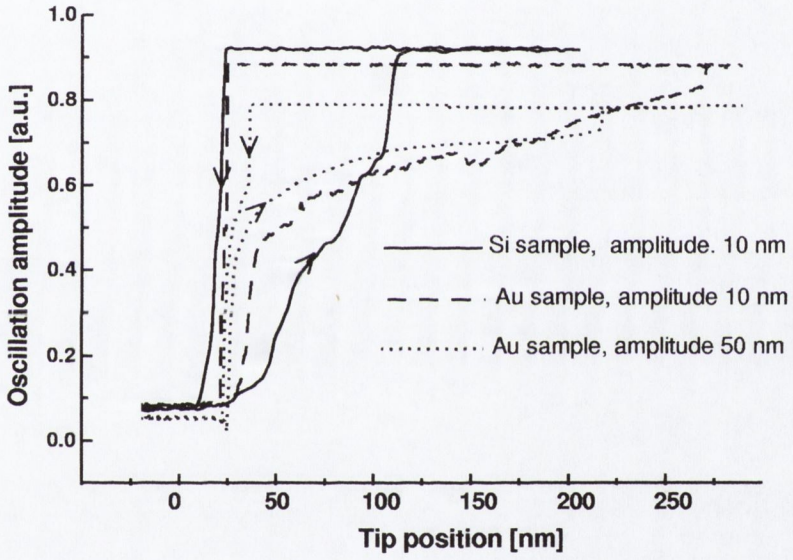

Figure 3.8: Shear-force interaction for a blunt tip

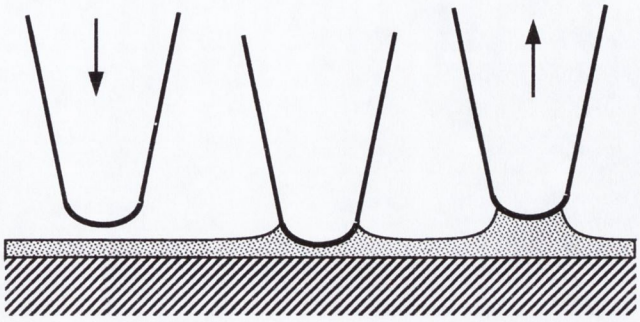

Figure 3.9: Influence of a surface water layer on the tip oscillation

be rather a combination of various forces - including viscosity forces, van der Waals forces or just the friction between the surface and the probe for varying perpendicular pressure applied on the tip apex. Although their contribution may vary depending on the particular experimental conditions, a number of experiments [55, 56, 57, 58] have shown the importance of surface properties on the damping behavior. In ambient conditions, most materials are water-adsorptive enough to attract air humidity and to form a few nm thick layer on the sample surface, influencing the oscillation of the tip in close proximity to it [59]. We believe that during the backward motion of a blunt tip capillary forces pull the surface water contamination, forming a meniscus surrounding the tip apex (figure 3.9) and perturbing the tip oscillations to relatively high distances as indicated by the experiment.

3.1.3 Touching geometry of oscillation coupling between the fork and the probe

One of the most critical factors of tuning fork SF detection is attaching the probe to the fork arm. This does not represent a problem for a stand-alone

topography detector as the short tip can be directly glued to the fork by a stiff adhesive as used in the above presented experiments, but it becomes crucial if the probe should function also as another detector, either optical or - as in our case - a microwave antenna. In a configuration proposed by Salvi et al.[60] the optical fiber probe is merely introduced between the prongs and held against its junction. Unfortunately, vibrations are coupled between the probe and the fork by a causal non-symmetry in the geometry. Furthermore, due to low damping of the arms oscillation by the probe, the system is characterized by a high quality factor and low response speed.

We would like to propose here a simple coupling method by static lateral forces of a slightly bent probe (figure 3.10). The probe must be rigidly clamped by a fiber holder to sustain small static forces. Although it might seem that high oscillation frequencies would cause rebounding of the probe from the arm, simple estimation calculus shows the opposite. If we put the condition of permanent tip/fork contact that the acceleration caused by the reaction forces of probe bending should be at all times higher than the maximum acceleration of the real oscillations, we get minimal probe bending

$$\Delta x > A\frac{\omega^2}{\omega_p^2} \tag{3.7}$$

where A and ω, are the oscillation amplitude and frequency respectively, ω_p is the resonant frequency of the probe rigidly clamped in a holder. We have used here the probe resonance frequency ω_p rather than direct static forces as it can be calculated from the particular probe geometry. Optical fiber probes of 5 mm length or shorter have resonance frequencies exceeding 5 kHz [61, chapter 2.3], for standard operating amplitudes of about 20 nm at frequencies above 20 kHz we get $\Delta x > 320$ nm to fulfill condition (3.7). Although the resonance frequency for metal microwave antennas can drop

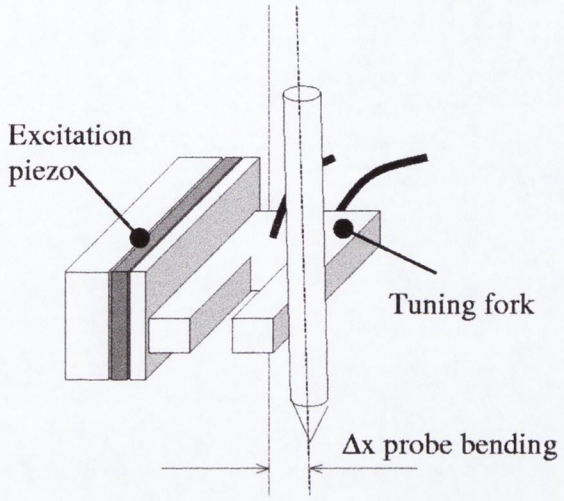

Figure 3.10: Touching mode of the coupling of oscillations between the probe and the fork

to several hundreds of Hz, a probe bending of about 0.1 mm is sufficient to sustain the acceleration of the working oscillations.

We have tested the configuration using a 4 mm length probe, the resonance frequency of the system was about $\omega_0 = 21\,\mathrm{kHz}$. The measured interaction curves (figure 3.11) were slightly different than for similar measurements with a glued tip. The difference is probably caused rather by the different shape of the tip apex than the different geometry of the oscillator.

Although the described configuration was not eventually employed in the set-up prototype (see section 3.6) we think that it may be found to be an attractive method in SNOM where the incorporation of a quartz fork became a popular method for the probe distance control (also in recent commercial SNOM set-ups [62]) but still uses a glued probe.

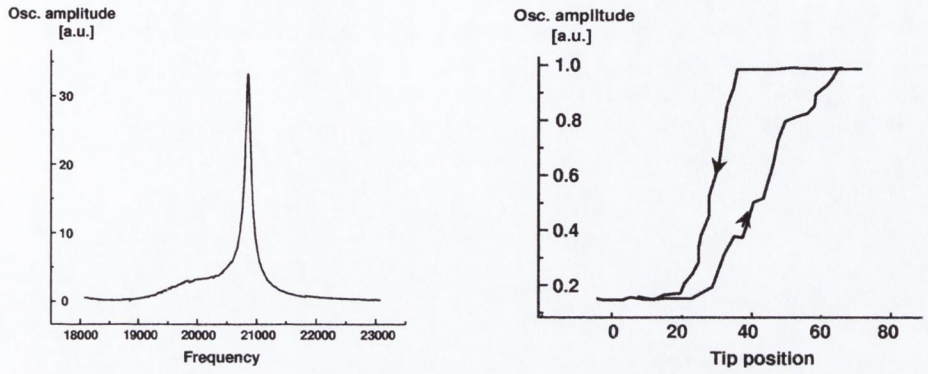

Figure 3.11: Resonance and approach curves for touching more of oscillation coupling. The sample was single crystal Si wafer, oscillation amplitude was about 30 nm.

3.2 Tapping mode scanning force distance control

The tapping mode provides a more sensitive and reliable method of probe/sample interaction sensing rather than shear-force detection as all surface repulsive and attractive forces are perpendicular to the interface. Although the conservative forces do not directly cause the vibration energy dissipation, they influence the oscillation conditions and the resonance frequency by the force gradient [63, 64]. An additional advantage of the configuration, with a cantilever vibrating perpendicular to the surface, is the robustness of the system: a causal direct contact of the probe in most cases does not cause probe damage - only bending of the fork prong (to which the tip is attached) as its lateral stiffness is much lower than the rigidity along its length.

Successful use of the tapping mode of tuning fork topography sensing was reported by Tsai et al. [53] and Giessibl [65]. We have employed our tested tuning fork configuration in the tapping regime just by its rotation through

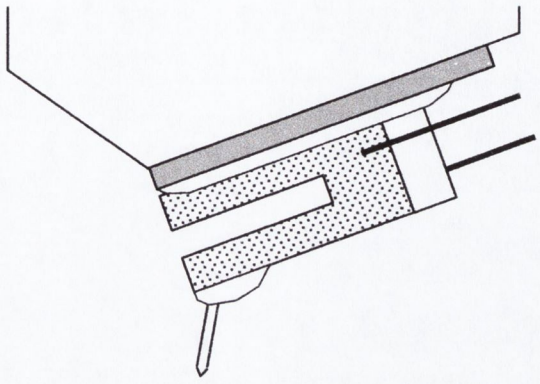

Figure 3.12: Tapping mode of tuning-fork topography detection

an angle of 60-80 degrees (figure 3.12). Different modes of probe/sample interaction were observed depending on the oscillation amplitude and tip apex shape - see fig. 3.13:

1. low primary oscillation amplitude and sharp tips: The curves were similar to the ones for the shear-force interaction. The damping mechanism is probably similar to the SF one and it is likely caused by a water contamination of the surface, but may be influenced by other forces also (especially van der Waals forces).

2. high primary oscillation amplitude and sharp tips: The interaction region was very linear and proportional to the excitation amplitude. The interaction can be described as a "knocking" of the tip apex against the sample surface.

3. low dithering amplitude and blunt tips: the wide withdrawal curve is most likely caused again by a water layer pulled by liquid capillary forces. The approach interaction interval is wider than for sharp tips

and is probably caused by the damping of the air layer between the tip apex and the sample. It is not clear if that damping is caused by the dissipative turbulent motion of the air or by the pressure change of the air between the blunt tip apex and the sample for relatively high frequency vibrations. Such changes would effectively act as gradient forces, changing the resonance frequency of the system and the amplitude of oscillation - similar to van der Waals forces for AFM probes [66].

4. high dithering amplitude and blunt tips (not included in the figure): The tip is again knocking on the sample but the forces are distributed over a larger area so the interaction can be considered as more "gentle" than for the second case.

Various tapping modes give us the possibility of choice of an appropriate scanning method for topography acquisition with respect to the inspected area and the scanning velocity. For large areas and fast scanning speeds, tips with a large apex radius can be used. Whenever higher resolution is required, the sharper tips and lower scanning velocities have to be used.

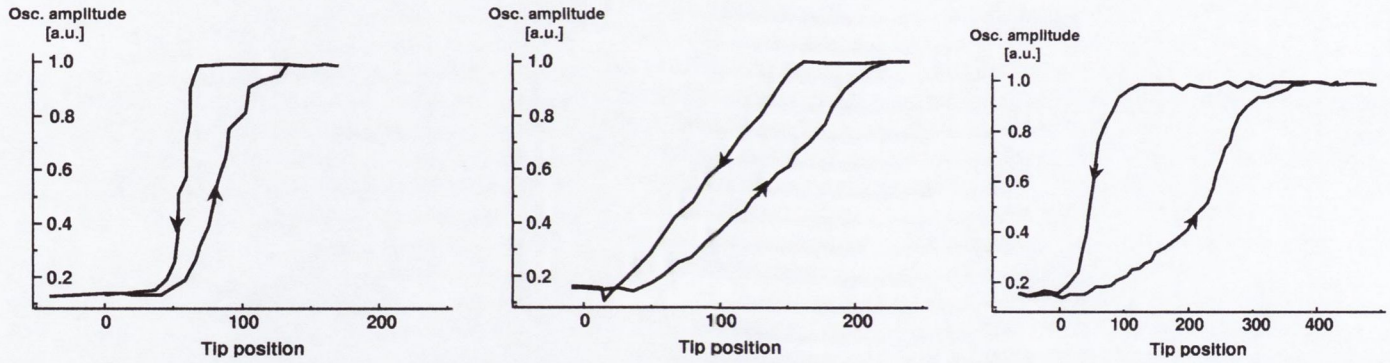

(a) $r = 0.5\mu$m, $A = 15$nm (b) $r = 0.5\mu$, $A = 60$nm (c) $r = 20\mu$m, $A = 20$nm

Figure 3.13: Various interaction modes of taping SFM configuration. The approach curves differ with respect to the arex radius r and primary excitation amplitude A

3.3 Measurement of oscillation amplitude

In many papers the fork signal is compared to the values of oscillations measured by alternative methods, in most cases optical. Thanks to the linearity of piezo-electric response, the fork sensitivity is usually refereed as a ratio between the fork voltage and the oscillation amplitude,

$$k = \frac{U}{A} \tag{3.8}$$

We have measured the real oscillation using a method where a laser beam is diffracted at the probe or the fork arm edge - a method somewhat similar to the one described by Wei et al. [67]. For the standard configuration (paragraph 3.1.1) the definition (3.8) is appropriate as the ratio between the arms vibration may vary due to different mass and geometry of the attached probes and the calibration should be performed with every probe. For the single-arm configuration, the induced voltage can be directly compared to the deformation which takes place in only one arm, so the sensitivity should not be dependent on the particular probe mass. Nevertheless, the detected voltage is strongly dependent on the load of the signal conditioning system -particularly on its input capacitance. The reason for this influence is that the fork should be considered as a current source. This fact corresponds to the physical principle of signal generation: due to the piezo-electric effect the deformation of the arm induces a certain charge at the fork electrodes and the amplitude of the induced current is

$$J = \frac{dQ}{dt} = k'\omega A \tag{3.9}$$

where k' is a factor depending only on the particular fork type and can be considered constant for the particular manufacturer and fork model. The detected voltage is then

$$U = \frac{J}{\omega C} = k' \frac{1}{C_f + C_i} A \tag{3.10}$$

where C_f is the fork capacitance (which for most watch crystals is in the range of 1.5-10 pF [68]), C_i is an input capacitance of the detection system. The resistanceof the input is for voltage measuring instruments above $10^9\Omega$ and can be neglected relative to the capacitive reactance for the frequencies of interest. Our observation showed very good agreement with the above formulas[2], the measured sensitivity constant for our forks was $k = 3.5 \cdot 10^{-6}\mathrm{Asm}^{-1}$. As the fork represents a weak current source, a low noise amplifier close to the fork may improve the signal-to-noise ratio for long connections between the fork and the instrument.

3.4 Self-excitation regime of the tuning fork

The tuning fork systems are usually dithered by an external piezo-tube, bimorph or - as on our case - a thickness mode piezo plate. The reason for this is that it is difficult to separate the mechanical oscillation response from the excitation signal for the relatively low quality factor of the quartz crystals. To assure the frequency stability, the watch crystals normally operate encapsulated in a can, having a quality factor in vacuum in the order of 10^5. For forks implemented in SFM probes with Q below 1000, the ratio between the

[2]Our first probes were not equipped with a preamplifier and detected voltages were inverse proportional to the length of used coaxial cables, $U \sim 1/(L + c)$. In fact the use of coaxial cables with known capacitance per unit length is more precise method to determine k' then use of shunt elements.

oscillation response and the dithering signal - and which can be measured on the fork pins as a change of its impedance - is low, we have measured its values in the range $10^{-1} - 10^{-2}$. An additional problem is represented by the load of the measurement unit connected to the high impedance of the fork. Although both issues can be probably addressed by the use of a Wheatstone bridge circuit in a way Hsu et al. applied on a dithering piezo [50], incorporation of an additional circuit element and further requirements for the bridge adjustment would not allow the probe miniaturization and would rather increase the probe complexity than simplify it. A possible implementation of the self-excitation regime of the fork is presented by Chuang et al. [69] which uses a time-gating method where the excitation/oscillation-sensing signals are multiplexed by an electronic switch in sub-millisecond intervals. Although the method seems to be very useful, it requires some additional instrumentation and extends the response time of the system.

We have developed a simple yet efficient method for signal separation based on the fact that for resonance frequency the mechanical oscillations and electrical response are shifted relative to the excitation signal and forces by 90 degrees. This signal orthogonality allows phase-sensitive detection of the component corresponding to the mechanical vibrations only and suppressing the excitation signal to about two orders below that of the functional component.

The figure 3.14 describes the plug-in schematics for the oscillator. The tuning fork is plugged directly between the generator and the inverting input of an operational amplifier. For the excitation signal the circuit represents an electronic differentiator with the fork as a capacitor, its output signal $U_e = \omega RC_f$ is shifted by the differentiator by 90° and is suppressed by lock-in synchronous detection. For the mechanical oscillations the circuit functions

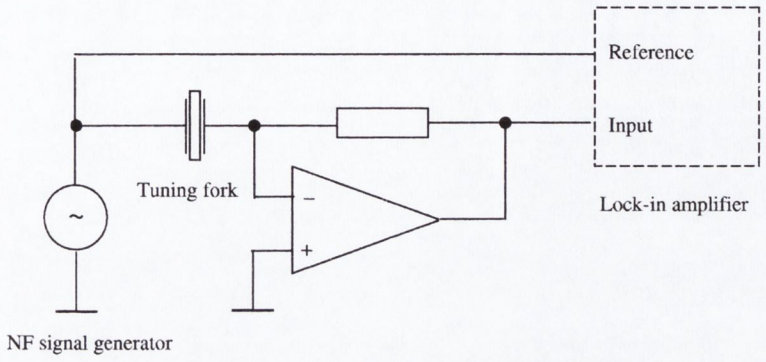

Figure 3.14: Schematics of the fork plug-in

as an I/V converter with output voltage

$$U = -JR = -k'R\omega \cdot A \tag{3.11}$$

As the input of the I/V converter represents a virtual ground, it does not influence the fork by its capacitance and the oscillation amplitude can be directly calculated using 3.11. The circuit functions simultaneously as a signal conditioner whose low impedance output can be matched to any standard transmission line.

In terms of the system sensitivity and response time the performance of such a circuit is similar to those with an external excitation piezo. On the other hand it increases the system reliability with a simpler system adjustment as there are no requirements of lock-in phase adjustment due to the phase shift caused by the particular mechanical contact of dithering piezo. This permits the possibility of probe miniaturization and easy exchange of the tips. The combination of such an excitation circuit together with the tapping mode configuration of the fork makes an optimal choice for incorporation in

our system.

3.5 Velocities of the probe motion

3.5.1 Stability of the feedback system

The signal from the tip oscillations is detected by a lock-in amplifier and used in a negative feedback for probe positioning to keep the signal in the middle of the interaction range. The limited time response - and the phase shift caused by particular components in the feedback system - may cause a system oscillation for a high overall gain of the feedback. The main response delays are caused by the mechanical properties of positioning system, with resonance frequency about 200 Hz, and the response time of the SFM mechanism. For a single oscillation arm geometry, its value is about 1ms and the corresponding frequency limit of about 150Hz still remains the main factor limiting the response speed. The exact calculations and establishment of a theoretical stability criterion is very difficult as the tip/sample interaction curves are non-symmetrical and strongly non-linear. We can nevertheless perform some estimative calculations for the loop-back gain to keep the system stable. We have observed that the main instability factor comes from the limited interaction range of the SFM mechanism rather than the particular slope of the approach curve.

If we want to keep the spurious system oscillation amplitudes A_{max} with velocities

$$v_{max} = 2\pi f_{max} A_{max} \tag{3.12}$$

in the interaction range I so $2A_{max} < I$ we get for the maximum probe speed

the condition

$$v_{max} < \pi f_{max} I \tag{3.13}$$

where f_{max} is the frequency limitation of the feedback. We have expressed this condition in terms of the maximum probe velocity rather than the total feedback gain because of integrational character of our loop-back system for which the signal from the probe controls the velocity of the tip motion - not directly its position. For an interaction interval of 10-500 nm, which depends on the working regime of SFM probe, we get limited values for the perpendicular probe motion in the range of 5-250 μm/s.

Our observation of the feedback stability corresponds well to the above estimations. The values compare better to the width the withdrawal curves - probably because once the tip is in contact with the surface, the water layer between the probe and the sample is always present and it allows a higher speed of probe motion. Note that one can also operate at velocities exceeding the mentioned limit: in such a case the system oscillates with an amplitude corresponding to equation (3.12) in a sort of "jumping mode" for which the approach curve represents more-less the step response function. For such a working regime it is better to filter out the mechanical resonances, which may have a relatively high quality factor, and work on lower frequencies predefined by the lock-in internal time constant - in our case $\tau = 3$ms ($f \doteq 50$Hz). This regime is suitable for blunter tips and tapping mode probes (section 3.2) where the perpendicular forces just bend the fork arm. We have often used probes with radii of about 5 μm at velocities of 300 μm/s for which the maximum arm bending of 1 μm represents forces about of $5 \cdot 10^{-3}$N and can be easily sustained by the tip without its, or the samples, damage.

3.5.2 Scanning velocity

The horizontal scanning speed is limited by the fact that the stylus must be able to follow the sample relief. It depends not only on the feedback speed but also on the particular circuit profile and the probe geometry. For probes positioned perpendicular to the sample plane the scanning velocity is limited by the apex radius and the angle of conical probe shape (see figure 3.15). For most probes the taper angle is relatively low ($10^o - 15^o$) and it is difficult to avoid direct probe contact and probe bending at step-like features of the circuit. These steps are very common for planar circuits prepared by lithography techniques and for such structures it is better to attach the stylus to the arm with an inclination angle α. This inclination allows one to increase the scanning velocity to values

$$v_{scan} = v_{max} \cdot \tan \alpha \tag{3.14}$$

where v_{max} is the vertical velocity limitation of the feedback described in the previous paragraph. For real scanning the determined velocity should be reduced by a factor of about $1/2$ to facilitate the feedback to act with a certain reserve. Such a probe placement causes convolution of the resulting topography data - i.e. the step structures appear trapezoidal in the resulting image. As for the field measurements where only acquisition of the overall surface structure is required to keep fixed separation between the antenna and the circuit (not precision following of every strip edge) we have often used large angles (up to 70^o) and high velocities ($v_{scan} = 0.5$ mm/s) for scanning large PCB areas.

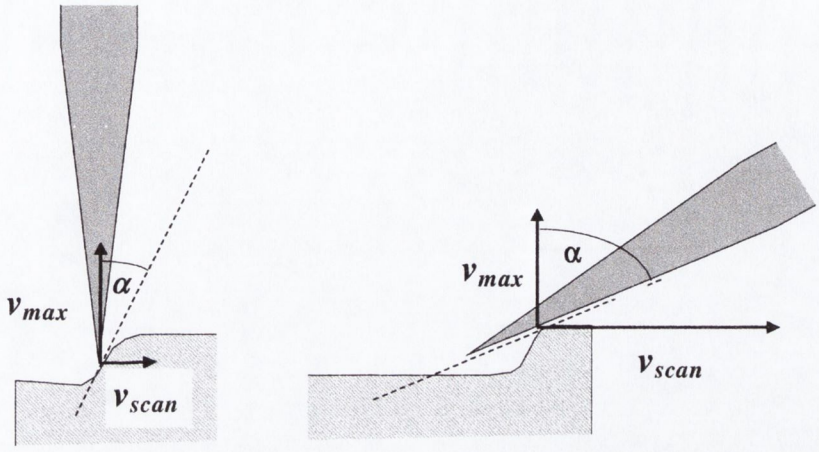

Figure 3.15: Influence of the probe geometry and placement on the scanning speed. For perpendicular probe placement the maximum speed depends on on the probe taper angle or the andle of the edge (whatever is bigger).

3.6 Topography tips

We have manufactured our tips from an optical glass fiber using a custom-built pulling machine. The machine is used by our SNOM group to produce optical near-field probes and it allows one to use various pulling regimes with different pulling velocities/acceleration and different timing of a 50 W CO_2 laser heating. Such differences are essential to form probes with various geometries; with different apex radii and different taper angles (see figure 3.16) The use of different tip shapes facilitates the use of different working regimes for scanning various samples with different velocities and resolutions.

We have also tested our micro-wires incorporated in our electric antennas (Figure 3.16 c) - as the topography probe in shearing mode by gluing the wire to the fork arm. The purpose was to test the possibility of combining both topography and electric probes in a single unit. The wire - a copper conductor

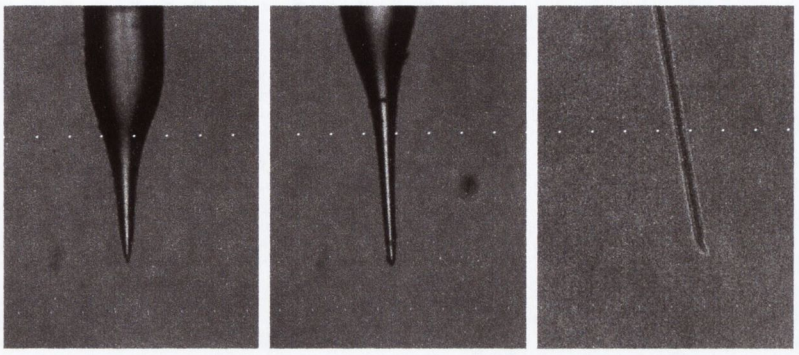

(a) apex radius $r = 1\mu$m

(b) apex radius $r = 3\mu$m

(c) antenna wire: copper core radius $d = 8\mu$m, glass clad 3μm

Figure 3.16: Topography tips and the antenna wire.

of 8 μm diameter encapsulated within a 3 μm glass cladding - was protruding from the fork arm by about 0.5 mm. Unfortunately, the measurement of the approach curves did not show any detectable oscillation damping during the interaction of such tips with the sample surface. The reason for this lack of sensitivity is relatively low lateral stiffness of the long but low diameter wire, which does not allow transfer of the shearing forces to the oscillating arm. Furthermore, the wires own resonance frequency is much below that of the arm - it can be expected to be in the range of a few hundred Hz - so it does not follow the arm movement. If we would apply the touching excitation mode to the real E-field antenna, the effective mass of the oscillation system would be even higher and this fact - together with complexity of the unified system - effectively disqualifies the combined E-field/topography probe for use in our system.

Chapter 4

Electric field probes

4.1 Short monopole antennas

As mentioned in the introduction we have focused our attention on electric intensity measurement using miniaturized coaxial antennas where a central conductor protrudes for a defined length from the shielding. For acquisition of the signal in the far-field region, the antenna wire usually has length comparable to $\lambda/4$ and operates at its own resonance to achieve good sensitivity and impedance matching to the following transmission line. For acquisition in the near-field region, the wire length must be shorter and must compare to the desired resolution. Our first antennas - so-called short mono-poles - were similar to miniaturized versions of those used by Dahele and Gao [1, 15].

The antenna response is normally defined as a signal of the antenna placed in a homogeneous field and it depends on its geometrical parameters: the diameter d and length l of the protruding wire and shielding diameter D (figure 4.1). In some cases the analysis of the antenna can be simplified: for wire length shorter than the diameter of coaxial shield the calculation of the influence of current flow in the shielding can be limited to its conducting

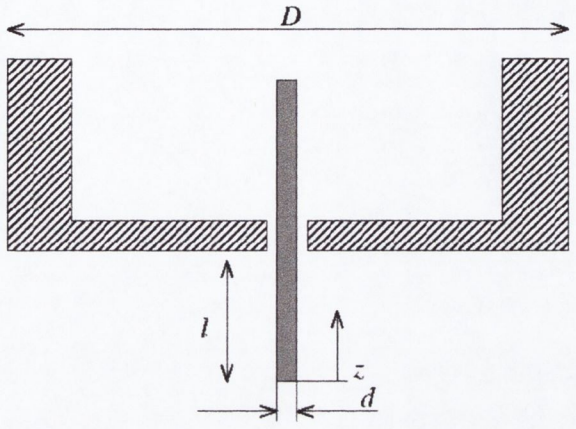

Figure 4.1: Short monopole antenna.

front screen and calculated according to [39, sec. 3.6]. If the wire is much shorter than the diameter ($D \gg l$), the front plane currents can be simulated by the image method and substituted by the missing second half of a dipole antenna. The response of the monopole is then analogous to that of a dipole antenna, originally presented by Hallén and the solution can be found in [39, sec. 3.4]. For wire dimension much smaller than the wavelength ($l \ll \lambda$), but still longer than its diameter($d \ll l$), the distribution of the current along the center rod is linear,

$$J = J_0 \frac{z}{l} \tag{4.1}$$

The probe input current J_0 can be calculated using its basic electrical parameters in accordance with substitution schematics presented in figure 4.2

$$J_0 = \frac{U_{eff}}{Z_L + R_r - \frac{i}{\omega C_l}} \tag{4.2}$$

where the antenna capacitance C_l, radiative resistance R_r, the load impedance

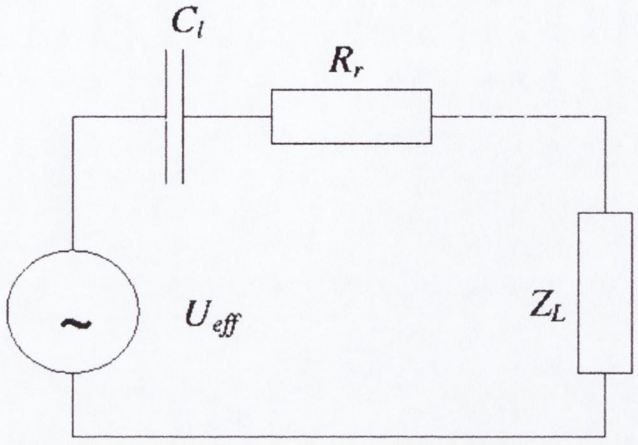

Figure 4.2: Electrical equivalent schematics of a short monopole

Z_L and the effective field source voltage U_{eff} can be calculated using the approximation of Hallén's integrals [70, chap. 9] for $l \ll \lambda$

$$\begin{aligned} C_l &= 55\frac{l}{\ln\frac{l}{d}}\text{pF} \\ R_r &= 40\pi^2\frac{l}{\lambda}\cdot\Omega \\ U_{eff} &= E_z\frac{l}{2} \end{aligned} \tag{4.3}$$

The antenna spatial resolution is comparable to the region which influences the wire (and its virtual image) currents to fulfill the field boundary condition on the conductors and can be assumed $\approx 2l$. To a certain degree, when the field is highly concentrated around the protruding wire apex only, images with spatial contrast better than the antenna length can be obtained, unfortunately they lack quantitative characterization.

The calculations for our antennas ($l = 50 - 150\,\mu m$, $d = 8\,\mu m$, $f = 2 - 8$ GHz) give us the value of the capacitance C_l in the range of a few fF. The radiative resistance R_r in the range of $10^{-1}\,\Omega$ can be neglected when comparing to the capacitive reactance of order $10^5\,\Omega$ and the antenna represents a nearly ideal current source with very high impedance of capacitive character.

The model presented above applies only to protruding wire smaller than the shielding diameter. In the opposite case the surface currents within the shield jacket also contribute to the secondary field and influence the protruding wire. The antenna has to be analyzed for particular probe geometry using numerical simulations [71]. As the result depends on the particular field distribution, a homogeneous case of the external field surrounding the whole antenna is normally assumed to obtain a single sensitivity coefficient - a ratio between the signal level and the field intensity.

4.1.1 Realization of the antennas

Our antennas consist of a body forming a coaxial transmission line - see figure 4.3. The central copper wire is separated from the shielding by its glass cladding and an additional fused silica tube to keep the characteristic impedance of the line relatively high. The particular dimensions of the antennas components can be found in table 4.1. The antennas were assembled using precise micro-manipulators. The front shielding was formed by a conductive adhesive and the wire protrudes from it by 50-150 μm (figure 4.4 a).

The basic electric parameters of the antenna body are

Component	material	I.D.	O.D.
Shielding	stainless steel	125 μm	230 μm
Dielectric separation	fused silica	30 μm	105 μm
Core conductor	copper & glass	8 μm copper core	14 μm glass cladding

Table 4.1: Antenna components

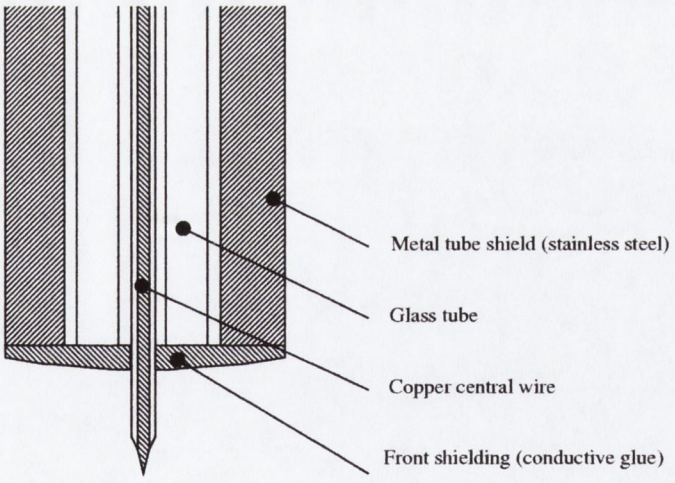

Figure 4.3: Electric antenna cross-section

$$
\begin{aligned}
C_0 &= \frac{2\pi\varepsilon_0}{\sum \frac{1}{\varepsilon_i} \ln\left(\frac{r_i}{r_{i-1}}\right)} = 34\text{pF/m} \\
L_0 &= \frac{\mu_0}{2\pi} \ln\left(\frac{r}{r_0}\right) = 0.55\mu\text{H/m} \\
Z_0 &= \sqrt{\frac{L_0}{C_0}} = 127\Omega
\end{aligned} \tag{4.4}
$$

Note that the above formula apply only for symmetrical axial structure, the real values of the capacitance and the impedance can be estimated to be somewhat lower due to eccentricity caused by air gaps in the structure. These gaps also causes the dispersion of the guided waves due to different propagation factors in different materials. Unfortunately the general solution for such non-axial structures is not known and the non-symmetricity has to be neglected.

One of the problems which may occur during the scanning measurements is the presence of the shielding close to the circuit as it may cause redistribution of the charges on the circuit conductive lines and distortion of the primary field E_p. Unfortunately, this is the case of most our measurements with resolution below 50μm. As the antenna must be driven at comparable distance, a 230μm diameter of our probe shielding causes significant distortion of the primary field and measured results. It was attempted to address the issue by reduction of front shielding by evaporating a few μm thick silver layer directly on the conductor glass cladding or forming the shielding by a silver paint (see figure 4.4 b). Because such a shielding forms low impedance coaxial line of about 15Ω, it must be relatively short so as not to burden the input by additional capacitive load and decrease the antenna overall sensitivity.

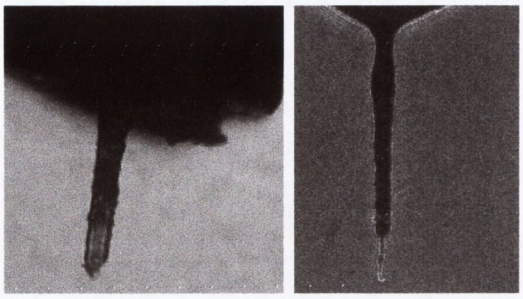

(a) (b)

Figure 4.4: Electric field antennas in standard configuration (a) and with reduced front shielding (b).

4.2 Sensitivity of the probes

The signal level coupled to the acquisition system depends not only on the antenna properties but also on the matching efficiency to the following transmission line and its properties. It is practically impossible to efficiently match such probes to the microwave network as the probes represent nearly ideal current sources with very high impedances. In comparison to standard transmission lines with impedance $50\,\Omega$ the mismatch is in the range $10^3 - 10^4$ and normally microwave resonators such as microwave cavities, coaxial resonators[10, 67], with corresponding quality factor have to be applied to optimize the signal transmission. Unfortunately, their very narrow bandwidth would limit the experiments to single frequency measurements. Furthermore their dimensions, comparable to the wavelength at which they operate, and their mass do not allow their incorporation into our measurement set-up. To a certain degree sophisticated matching networks can increase the efficiency for certain frequency range for which they are optimised, unfortunately, they require a rather large space area to accommodate distributed and shunt ele-

ments.

For our miniature probes we have chosen more simple matching scheme, which uses a quarter-wavelength transformer formed by the antenna coaxial input line of relatively high input impedance of about $Z_0 \simeq 120\Omega$. By choosing the length of this line to be equal to $\lambda/4$ for the frequency of interest, the impedance at the input can be increased to the value

$$Z_i = \frac{Z_0^2}{Z_{50}}$$

where Z_{50} is the input impedance of the following network - in particular an MMIC amplifier. For our values of the impedances the sensitivity increase is expected to be about 15 dB.

In our case, this quarter-wave line consists of two parts: a constant length front antenna body, visible in the picture A.1, and an internal line inside the housing terminated by a preamplifier. By choosing the position where this amplifier is connected and which represents a low impedance termination, one can tune the frequency of maximum sensitivity without changes to the overall geometry of the electric field probe.

We have calculated the properties of our system using the real scattering coefficients of our low noise MMIC amplifier as published by the producer [72]. The signal transmission between the antenna protruding apex and the amplifier input was modeled by a series of transmission lines of various lengths and characteristic impedances to approximate the line parts and tapered junctions between them (figures 4.5). The DC bias is coupled to the probe through its output, a 5V power supply unit is plugged between the VNA and the probe (fig. A.2). Figure 4.6 represents the calculated and measured frequency response of the antenna adjusted for maximum sensitivity of 4 GHz. The antenna model was calculated according to the substitution schematics

4.2 where input voltage can be put equal to 1V for calculation of the total transmission coefficient S_{21}.

The measured data were obtained for the antenna placed in a coaxial calibration unit (paragraph 4.2.1) at a position with electric field intensity 230 V/m. As such intensity results in an effective source voltage of 14 mV, the voltage at the curve maximum should be about 1.6 mV. The real measured value was about 3 times (-10 dB) lower than the predictions (see fig. 4.6 b). The difference is caused by both approximations of our model and the influence of the real properties of the antenna and the calibration unit. The properties of the rest of the microwave network - including the DC bias coupler - were compensated by the network analyzer calibration. Although we see the agreement between overall character of the curves, each antenna must be individually measured in a field standard. We have calibrated the microwave network as a whole to eliminate the influence of cables, connections etc.

4.2.1 Calibration of the antennas

The antennas has to be calibrated in a well defined field standard where the field intensity can be predicted by calculations. Possible configuration of a device - a TEM cell - generating relatively homogeneous field in area comparable with the wavelength was proposed by Crawford [73]. As the active region of our antennas are much smaller than the wavelength, we have build relatively simple calibration units based on standard signal transmission structures:

- 50 Ω coaxial line structure (fig. 4.7 a) into which the antenna is inserted through a small hole in the shield. The field intensity is inversely proportional to the distance from the line center.

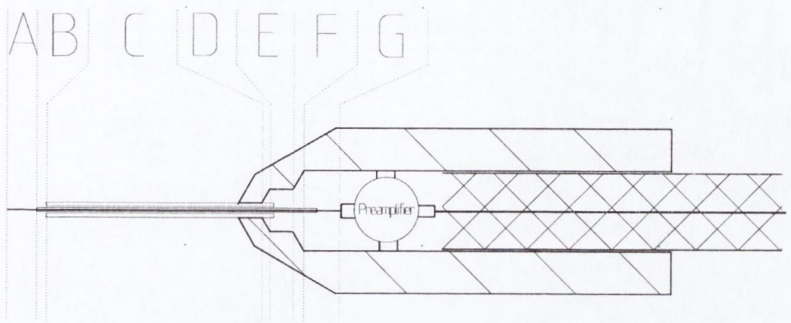

(a) Antenna outline

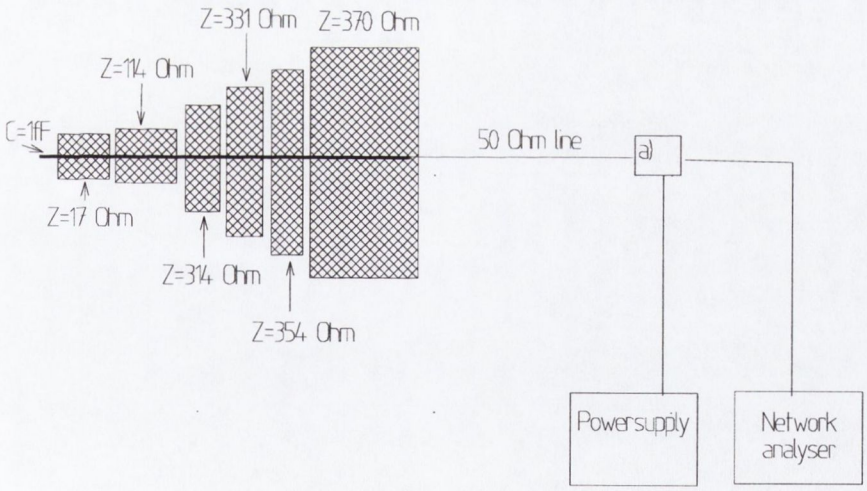

(b) Antenna schematics

Figure 4.5: The design of the antenna

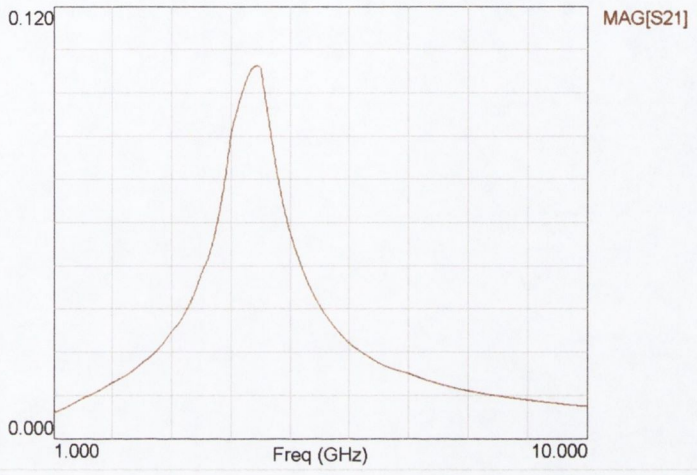

(a) Calculated transmission coefficient of the antenna

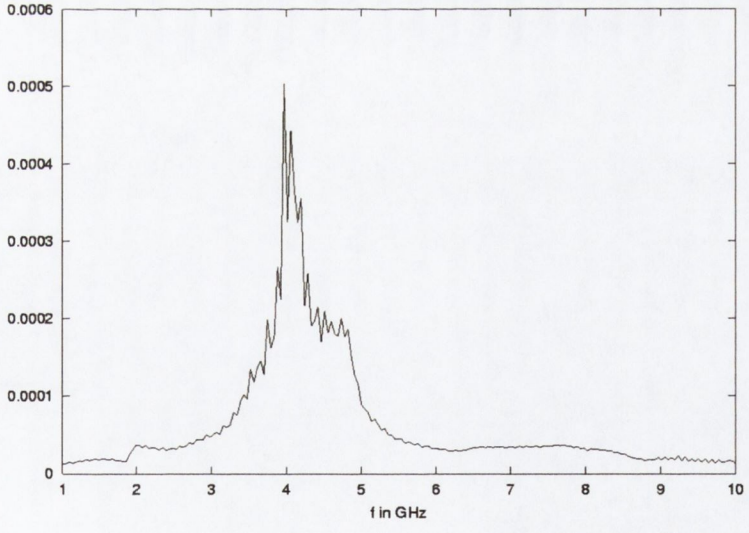

(b) The measured output voltage of the antenna placed in the field of the intensity $E = 230\text{V/m}$.

Figure 4.6: Antenna response. To compare the figures, the values of curve (a) must be multiplied by effective source voltage $U_{eff} = E\frac{l}{2} \doteq 0.014\text{V}$.

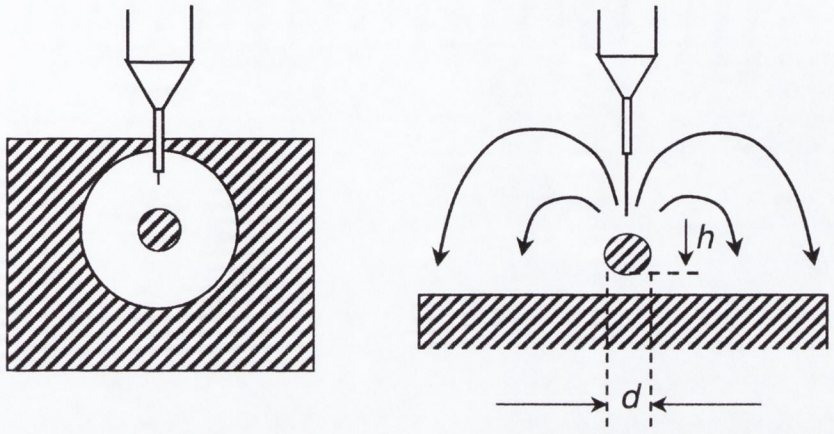

(a) (b)

Figure 4.7: Calibration units:
(a) cylindrical configuration
(b) air-suspended transmission line $d = 1.25\,\text{mm}$, $h = 0.23\,\text{mm}$

- 50 Ω air suspended cylindrical line above a grounding (fig. 4.7 b) for which the field can be calculated using expressions in table 2.2 where the line (and its ground image) can be substituted by a dipole line with separation $2a = \sqrt{h^2 + hd}$.

In both cases the line is terminated by a 50 Ω load to avoid wave reflection. Although the field in coaxial structure is better defined due to lower reflections at plug-in connections to the coaxial cables, the advantage of the second configuration is good antenna access and it allows calibration of wider range of probes including non-vertically positioned probes (see sec. 4.4).

4.3 Position-Difference (PD) method

It appears that only by decreasing the antenna dimensions along with coaxial shielding its spatial resolution capability can be improved. Unfortunately, miniaturization of the antenna to the micrometer range makes its fabrication rather difficult, especially fabrication of the coaxial line of low diameter and the forming of a short protruding central conductor. We would like to introduce here a new scanning method which overcomes the resolution limit determined by the antenna's dimensions and allows to increase its resolution capability without the need for further miniaturization of the antenna.

The design of new probes for PD method is similar to the standard coaxial antennas described in previous section, the only difference is that the protruding wire is significantly longer - about 0.5-1 mm. Additionally there is no need to form the shielding at the input to the coaxial line which makes the probes much easier to manufacture. The measurement method is based on comparing results of two subsequent scans with the antenna displaced by a small distance along its axis. The two positions of the antenna corresponding to different heights above the surface of the device under test are indicated in Fig.4.8 by numbers 1 and 2. We will show that for high density structures, when most of the field gradient is located close to the surface of the structure, the signal difference is determined only by the field strength surrounding the apex of the central conductor. By subtracting the two signals corresponding to two positions of the antenna displaced along its axis by distance Δz, one can cancel the contribution of the field in middle section (between planes $\mathcal{A}$ and $\mathcal{B}$ in the figure 4.8b) of the protruding conductor . Because for high-density structures the field above that region is supposed to be negligible, in this way the field surrounding the conductor apex can be isolated and measured. We will show that this method allows improvement of the spatial

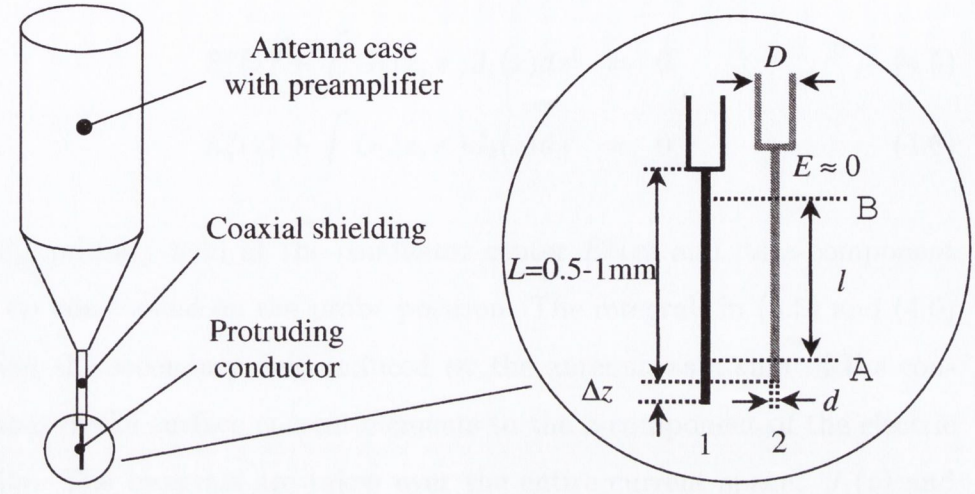

Figure 4.8: Position-difference method. The difference between antenna signals before and after small probe displacement Δz depends on the field surrounding the displaced antenna apex onlu

resolution of mapping of the microwave field.

4.3.1 Analysis of the position-difference method

In order to show that the contribution of the external field from the middle section of the antenna can be removed, we will analyze currents induced by the incident field and their dependence on the antenna geometry. Thanks to axial symmetry of the antenna the analysis can be reduced to investigating the boundary condition at the center of the conductor. As the sum of the primary incident electric field and the secondary electric field induced by the antenna surface currents must vanish inside the conductor, the condition for longitudinal component of the electric field, parallel to the antenna axis,

before and after displacement of the antenna can be written as

$$E_z^p(z) + \int G_1(z,z')J_1(z)dz' = 0 \tag{4.5}$$

$$E_z^p(z) + \int G_2(z,z')J_2(z)dz' = 0 \tag{4.6}$$

Here the primary field at the conductor center $E^p(z)$ and its z-component $E_z^p(z)$ do not depend on the probe position. The integrals in (4.5) and (4.6) represent the secondary field induced by the antenna as a sum of the contributions of the surface current elements to the z-component of the electric intensity. The integrals are taken over the entire current space. $J_1(z)$ and $J_2(z)$ signify currents before and after the displacement respectively. The Green functions $G_{1,2}(z,z')$ represent the weighting coefficients of the contribution of current sources to the secondary field. For the protruding cylindrical conductor the coefficient does not change as a result of displacement along its axis as it depends only on the position of the observation point z relative to the position of the current source z',

$$G_1(z,z') = G_2(z,z') = G(z-z') \tag{4.7}$$

The explicit form of the green functions can be directly derived from table 2.1 using general expression for electric intensity parallel to the current element,

$$G(z-z') = \frac{-iZ_0 \exp(-i\beta r)}{\beta 4\pi r^3} \times$$
$$\times \left[(1+i\beta r)\left(2 - \frac{3}{4}\frac{d}{r}\right) + \beta^2 \frac{d^2}{4}\right] \tag{4.8}$$

where Z_0 is the impedance of vacuum, d is the diameter of the conductor, $r = \sqrt{(z-z')^2 + d^2/4}$ is the distance between the current source and the observation point at the axis of the conductor and $\beta = 2\pi/\lambda$ is the propagation constant.

Let us focus our attention on the middle section of the protruding conductor in order to show that in that section the difference between the currents before and after the displacement is determined only by the currents at its boundaries and therefore the influence of the external field on the current difference can be removed. The section is defined by the planes $\mathcal{A}$ and $\mathcal{B}$ in between which the secondary field, induced by the antenna currents, can be calculated as a result of contribution of currents within protruding conductor, excluding the displaced apex and also excluding the contribution from the currents in the shielding. Because for $r \gg \frac{3}{8}d$ the Green function (4.8) decays proportionally to r^{-3} and the integrals (4.5), (4.6) quickly converge, the distance from the antenna displaced apex to the plane $\mathcal{A}$ can be chosen greater than diameter d so that the secondary induced field in this section is not directly influenced by the currents induced in the displaced apex. For the same reason the separation between the plane $\mathcal{B}$ and the shielding can be chosen greater than diameter D so that the contribution of the shielding to the field induced inside the section can be neglected. The integration space can therefore be effectively limited to the length L of the central conductor. By subtracting (4.5), and (4.6) and by taking into account (4.7) we get a single equation for the difference of currents in that region

$$\int_L G(z-z')\mathcal{J}(z)dz' = 0 \tag{4.9}$$

where $\mathcal{J}(z) = J_1(z) - J_2(z)$. The integral equation (4.9) resembles the boundary condition for the uniform transmission line with no induced longitudinal

electric field component. Its only non-trivial solution can be written in the form of two sinusoidal waves traveling in the two opposite directions,

$$\mathcal{J}(z) = \mathcal{J}_1 \exp(-i\beta z) + \mathcal{J}_2 \exp(i\beta z) \tag{4.10}$$

The current amplitude constants $\mathcal{J}_1$, $\mathcal{J}_2$ must match the field solution for the antenna apex below plane $\mathcal{A}$ and the input to the shielding above plane $\mathcal{B}$. Below plane $\mathcal{A}$ the currents depend on the field solution surrounding the displaced antenna apex. If we choose the origin for the z axis at the plane $\mathcal{A}$, the current difference $\mathcal{J}_\mathcal{A}$ (at $z = 0$) can be written in accordance with (4.10)

$$\mathcal{J}_\mathcal{A} = \mathcal{J}_1 + \mathcal{J}_2 \tag{4.11}$$

Above region $\mathcal{B}$ the strength of the external field is assumed to be negligible and the boundary conditions at the coaxial input front end depend only on its geometry. They can be expressed in terms of the reflection coefficient h_{11} for the currents at the input of the coaxial line for which

$$h_{11} = \frac{\mathcal{J}_2 \exp(i\beta l)}{\mathcal{J}_1 \exp(-i\beta l)} \tag{4.12}$$

The antenna displacement is equivalent to changes in its geometry: reduction of the length of the protruding conductor by Δz and displacement of the front end of the shield by the same value. In principle this should result in change in the value of h_{11} as it depends on the antenna geometry. However as Δz is negligibly small by comparison with wavelength λ, such a change can be neglected and h_{11} can be assumed constant. In practice h_{11} is close to unity due to a large mismatch between relatively low input impedance of the coaxial line and very high impedance of the free conductor, determined by its

residual coupling to the shielding. Using equations (4.10), (4.11) and (4.12) the transfer function of current difference from the the apex to the input of the coaxial line (between planes $\mathcal{A}$ and $\mathcal{B}$) can be be written

$$\mathcal{J}_{\mathcal{B}} = \exp(-i\beta l)\frac{1+h_{11}}{1+h_{11}\exp(-2i\beta l)} \cdot \mathcal{J}_{\mathcal{A}} \tag{4.13}$$

We see that measured current difference $\mathcal{J}_B$ is only a function of the apex currents $\mathcal{J}_A$ and contribution of the incident electric field between planes $\mathcal{A}$ and $\mathcal{B}$ is removed from the overall signal. The difference $\mathcal{J}_A$ depends on the changes in the apex geometry and the boundary conditions in the presence of an external electric field. These changes are limited to the region Δz of the displaced antenna apex, the measured signal - and the resolution of the measurement method - compares to the field intensity in that region.

The apex of the protruding conductor functions as a nearly ideal current source remains the main factors influencing the sensitivity of the system. As the transfer function (4.13) between the apex and the input of coaxial line depends on the length of the conductor, it may seem that it can be adjusted for optimum signal matching for $l \simeq \lambda/4$ for which the antenna operates at its resonance. Unfortunately, the mechanical properties of the conductor do not allow for extension of the length L above 1 mm. The vibrations and lateral bending of such a long and thin wire, mostly caused by air flow fluctuations and accelerations during scanning movement, causes degradation of the resolution. For our frequencies of interest (1-8 GHz) this length is significantly below $\lambda/4$ and the magnitude of the transfer function (4.13) is close to unity. This preserves the high impedance character of the apex current source and to increase the system sensitivity the same matching technique is used as described in section 4.2.

4.3.2 Numerical and experimental verification of the method

To verify the position-difference method we have compared the measured data with numerical antenna simulations and with expected field intensity. The Moment Method (MM) was applied to differentiate the original integral equations (4.5), (4.6). The calculations were performed for a non-symmetrical dipole, with one arm representing thin wire protruding from the shielding and the second arm corresponding to the long antenna coaxial body, placed in a non-homogeneous field as generated by the cylindrical calibration unit. Figure 4.9 compares the measured and calculated signals for different distances between the antenna and the cylindrical transmission line of the calibration unit. Due to the individual character of the probe sensitivity all signal curves were normalized to the values corresponding to the antenna apex placed very close to the signal line (50 μm) with high field gradient. We can observe that the slope of the position-difference curves - both calculated and measured - follow the theoretical field values more faithfully than the full antenna signals, especially for the distances below 1 mm where high field gradients are expected.

The level of detected antenna signal depends on the region where the antenna active part interacts with the external field. As for the position-difference method the active antenna region corresponds to the displaced apex of the conductor, the level of the resulting signal difference depends on the displacement value. Both mathematical simulations and the experimental results (Fig. 4.10) give a highly linear character of this dependency. As a typical preamplifier is also highly linear, the measured voltage U after its conditioning and transmission to the input of the acquisition instrument (VNA) is proportional to the antenna displacement Δz. We can therefore define the sensitivity of the system for a particular frequency by a single

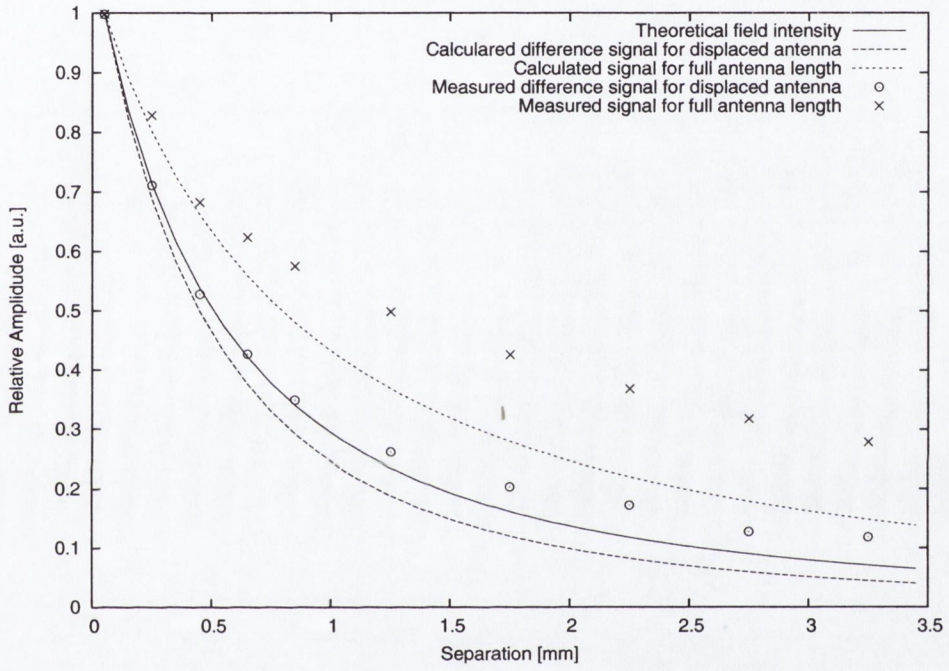

Figure 4.9: Calculated and measured antenna signals above a cylindrical transmission line.

unit-less constant S

$$S = \frac{1}{E}\frac{U}{\Delta l} \tag{4.14}$$

where U is the detected voltage and Δl the displacement between measurements. This constant, determined from the calibration measurement, can then be used during the scanning process for the calculation of real values of the electric field.

Although one can improve the resolution by reducing the displacement z, at the same time this leads to a reduction in the signal level. As the signal level must exceed the noise level, this may effectively limit the resolution of the antenna and make it dependent on the minimal detectable field intensities. The measured sensitivity constant gives us a minimum level of the detectable electric field intensity of about 15 V/m for a displacement 20 μm - and comparable spatial resolution - with noise signal level of about -95 dBm for a bandwidth of 10 Hz at 4 GHz frequency.

4.4 Acquisition of tangential components of the field

Although in many cases the measurement of the vertical electric intensity E_z is the most appropriate method for investigation of the circuit signals - i.e. for microstrip transmission lines, some situations may require examination of other spatial components of the field. Knowledge of the tangential field components E_x, E_y can be useful for description of fields of coplanar transmission lines and other structures with strong fields paralel to the circuits surfaces or for measurements of the field coupling between different parts of a device.

The position-difference method give us an opportunity to measure all

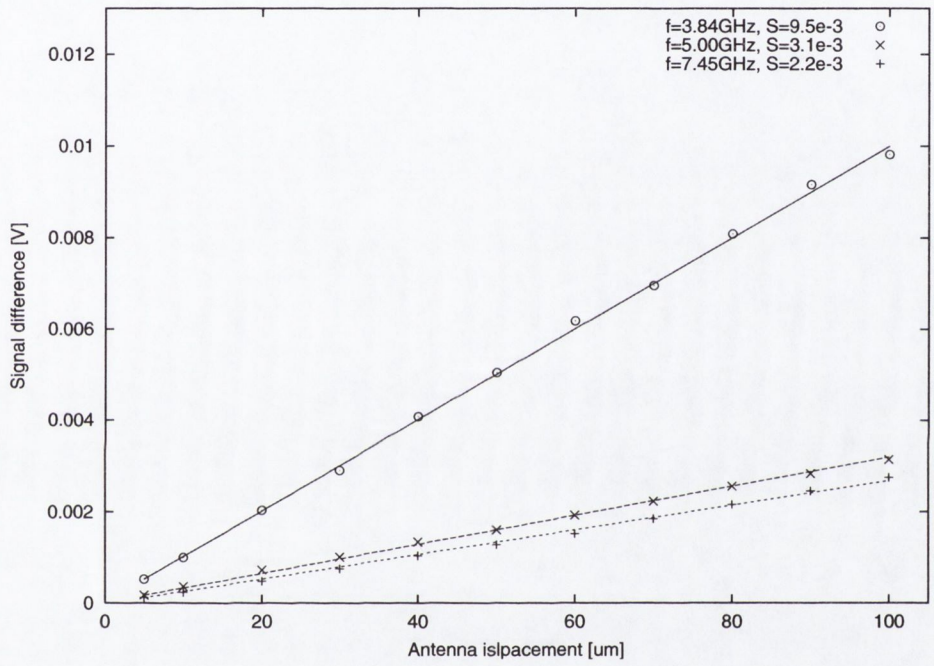

Figure 4.10: Dependency of the signal on antenna displacement

spatial components with a single probe. To accomplish that goal we have modified the configuration of our probes by placing the coaxial antenna with an inclination of about $\alpha = 45°$ relative to the vertical axis (see Fig. 4.11). By rotating such an antenna about the vertical axis different spatial components can be measured, standard Cartesian intensities relative to the circuit surface plane can be then recalculated. In the case of two measurements with the probe rotated by 180° about the normal, vertical and one tangential field intensity can be obtained:

$$\begin{aligned} E_z &= \frac{1}{2\cos\alpha}\left(E_{0°} + E_{180°}\right) \\ E_t &= \frac{1}{2\sin\alpha}\left(E_{0°} - E_{180°}\right) \end{aligned} \tag{4.15}$$

For three measurements with the antenna rotated by 0° , 120° and 240° about z axis all three components can be calculated

$$\begin{aligned} E_x &= \frac{1}{\sin\alpha}\left(2E_{0°} - E_{120°} - E_{240°}\right) \\ E_y &= \frac{1}{\sqrt{3}\sin\alpha}\left(E_{120°} - E_{240°}\right) \\ E_z &= \frac{1}{3\cos\alpha}\left(E_{0°} + E_{120°} + E_{240°}\right) \end{aligned} \tag{4.16}$$

For each antenna direction two measurements are prerformed with the probe displaced along the wire direction, the local intensity is taken as a signal difference. Additional offsets are applied to the probe position with respect to the antenna angle to place the antenna active apex to the same position for all measurements.

In general the field can be elliptically polarized, the phases of spatial components may differ. Therefore both the amplitude and the phase of the signal must be acquired by a VNA, the intensities in (4.15), (4.16) represent

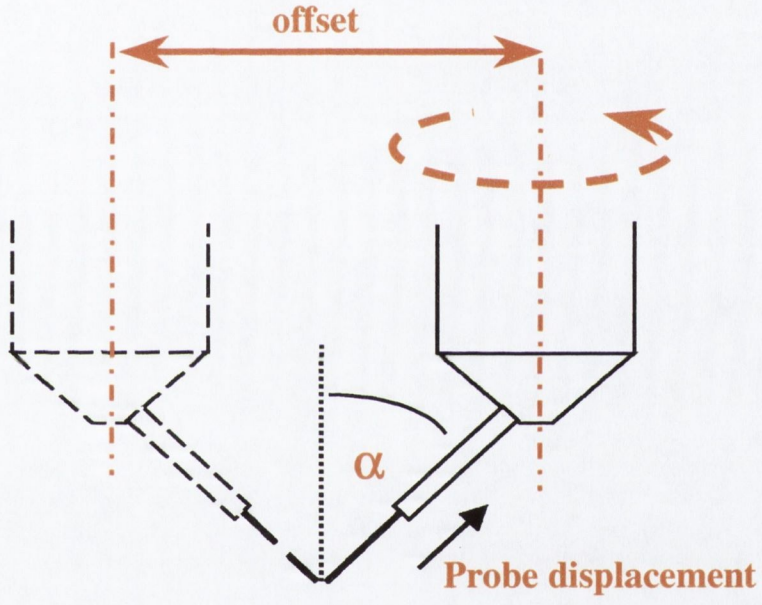

Figure 4.11: Probe configuration for measurement of all spatial components of the field

complex amplitudes of the signal.

Chapter 5

Scanning set-up

5.1 Probe displacement system

The desired scanning range (up to several cm) requires the use of motorized positioners for scanning movement. On the other hand, the rather poor dynamics of motorised stages do not allow sufficient acceleration to be achieved during the scanning process. Also the limited minimum incremental movement can not keep the feedback of topography probes within the range of probe/sample interaction.

The approach we have adopted is the use of motorized positioners for horizontal scanning motion (x and y axes) and combined motorized and piezo positioning stages for movement of the probes in the vertical z direction (see figure 5.1). The scanning is performed at constant horizontal velocities with low accelerations at the beginning and end of each scanning line. The piezo actuator with a range of 90 μm allows fast probe motion to copy the relief of the sample as shown in figure 5.1. The vertical motorized stage is used for probe repositioning when the piezo approaches the limits of its working range. The z coordinate is acquired and stored as a sum of positions of both

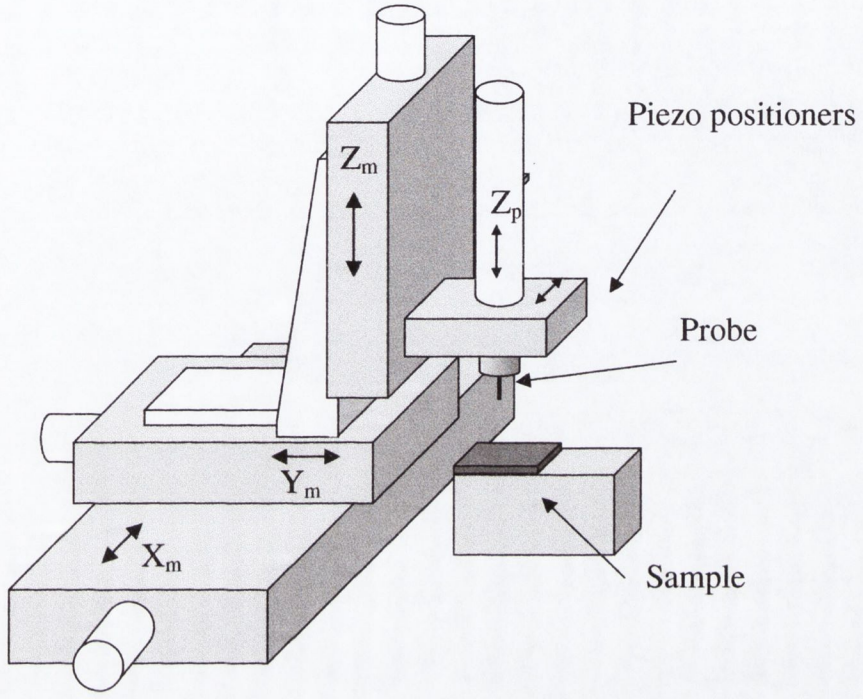

Figure 5.1: Design of the scanning system

actuators. All the scanning movement is performed by the probes keeping the device under testing in fixed position.

We have chosen M-415.DG/M-405.DG [74] DC geared precision positioners with ranges of 150 and 50 mm for x and y positioning, M-415.DG for z-axis movement. The DC servo motors with position encoders have relatively low vibrations, a factor critical for incorporation of SFM topography feedback which was up to this time used only with piezo actuators. They also allow smooth probe motion with relatively low velocities in the range of a few μm/s. To chose the best scanning strategy we have tested the accuracy of the positioners using a Michelson interferometer (figure 5.2) equipped with a He-Ne laser, a photo-detection circuit with a Schmitt trigger and a counter.

As we were counting both falling and rising edges of the trigger when detecting the interference fringes during the motion the precision of our device was comparable with $\frac{\lambda}{4} \simeq 160$nm. The main parameters tested were:

- Unidirectional repeatability: the difference of the stage position when a point is reached from the same direction. This limits the possible lateral resolution as all the lines are scanned from the same direction
  Measured value: 0-1 counts, better than 0.32 μm

- Bidirectional repeatability: the difference of the stage position when a point is reached from the opposite directions. This influences the vertical positioning error when vertical motor positioner adjusts the position to keep the piezo movement within its access range. As the movement is controlled "on-the-fly", it can not be predicted and the backlash errors can not be avoided.
  Measured value: 25-30 counts, 4-5μm, slightly worse than the value of 2μm specified by the producer.

- Linearity: the ratio between the error of the probe motion and the absolute distance. The linearity may distort the acquired image. More important is the influence on the precision of the electric field probe motion after the antenna exchange when additional offset has to be applied to move the antenna to the position of the topography probe. As the typical offset is about 1-2 mm (except the tangential-component probes where it is about 4-6 mm) the errors can be expected to be 1-2μm
  Measured value: 0.001

The piezo-actuator incorporates a friction-less guiding system (see picture A.7). Such a system is essential to avoid lateral probe oscillations and to keep

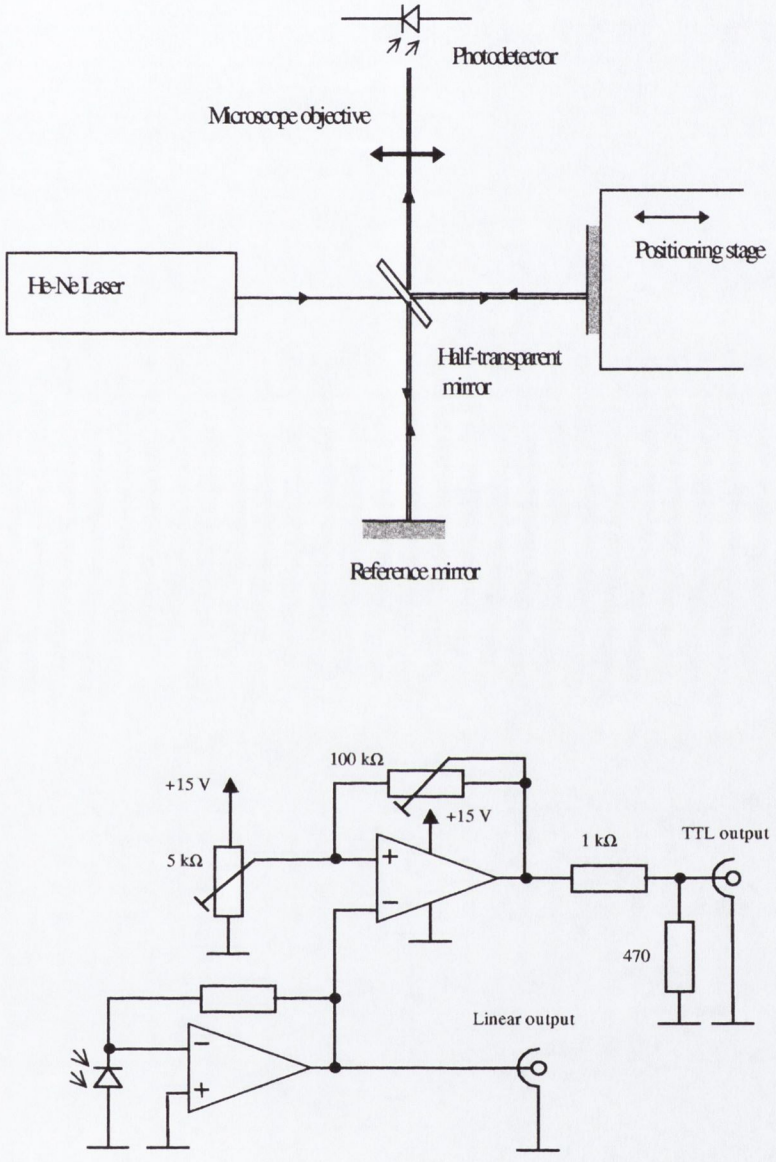

Figure 5.2: Michelson interferometer and photo-detection circuit

the system mechanical resonances at relatively high frequencies - in our case at about 200 Hz . Such resonations would increase the time of position feedback response and limit the topography scanning velocities (section 3.5). Apart from the positioning actuators and the probe holder the system also features a manual adjuster for fine-tuning of the probe vertical axis, the sample holder, the calibration units. The whole set-up is mounted on an optical table placed on a pneumatic vibration damping system.

5.2 Scanning controller

The scanning controller consists of several commercial instruments:

1. low frequency (up to 100 kHz) DSP lock-in amplifier for excitation of the SFM topography probe and its signal conditioning
2. servo-motor controller for driving motorized stages
3. vector network analyzer for generation and acquisition of the microwave signal
4. data acquisition board with precision 16 bit DA/AD converters for acquisition and generation of various system signals such as:
    - acquisition of position signal of the piezo
    - acquisition of feedback signal,
    - switching and control of the feedback during tip approach/withdrawal at the beginning and end of each scanned line
    - control of the speed of probe motion during topography acquisition
    - generation of the waveform for the piezo positioning during the antenna probe motion to copy the sample profile

5. GPIB interface for VNA and lock-in amplifier control

6. standard PC computer for control of the experiment

Apart from those general purpose instruments the set up incorporates a few in-house-built devices and measurement control software[1]

1. integrational feedback amplifier for tip/sample distance control during topography acquisition

2. low voltage (110V) piezo amplifier including DC power supply

3. keypad for manually controlled motorized positioning

4. scanning control software

5. program for data visualization and basic post-processing

The schematics of the control system is presented in figure 5.3.

[1] all those units (including the software) were designed and manufactured by the author

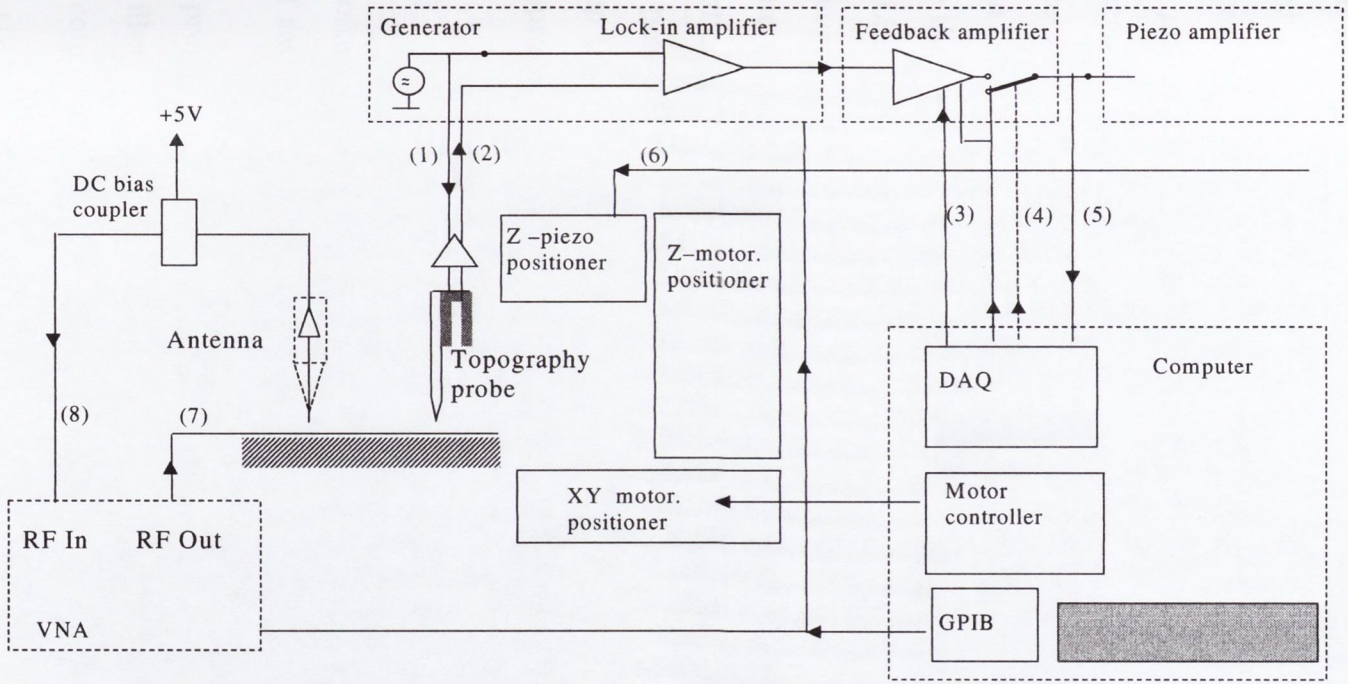

Figure 5.3: Scanning control system schematics. (1),(2): tuning fork excitation and response signals; (3) the scanning velocity control; (4) the direct control of the piezo position; (5) the piezo position signal; (6) the piezo driving; (7) the circuit microwave source, (8) the microwave antenna response

5.2.1 Feedback amplifier

After conditioning by lock-in amplifier the signal from the topography probe is used for piezo positioning to keep the probe response constant. Due to the limited interval of the topography signal response to about 50-100 nm the loop can not be a simple negative proportional circuit: for long range piezo of 90 μm extension the minimal gain expressed in terms of the resulting displacement would be more than 10^3 and with limited frequency response causing phase shift higher than 90 degrees for frequencies above 200 Hz the system becomes unstable. The answer is the use of an electronic integrator where the probe signal drives its velocity - not directly its position (see figure 5.4). Limited gain of the integrator determines maximum velocities of probe motion and allows the system to be kept stable.

Our feedback circuit (figure 5.5) also incorporates an input for direct control of the probes, an electronic switch which also keeps the position to avoid peak impulses during the switching. It also features a position limiter to keep the piezo extension in the middle of its range when the topography tip approaches the sample at the beginning of each line scan.

5.2.2 Scanning control and data visualization software

The software was developed throughout the whole project duration and consist of two independent parts:

- program for the control of the scanning process - about 11 000 lines (48 files) of C code, it uses LabWindows/CVI instrumentation library to communicate with the instruments
- data visualization software - about 5 000 lines, written in C++ and takes an advantage of FLTK [75] windowing toolkit

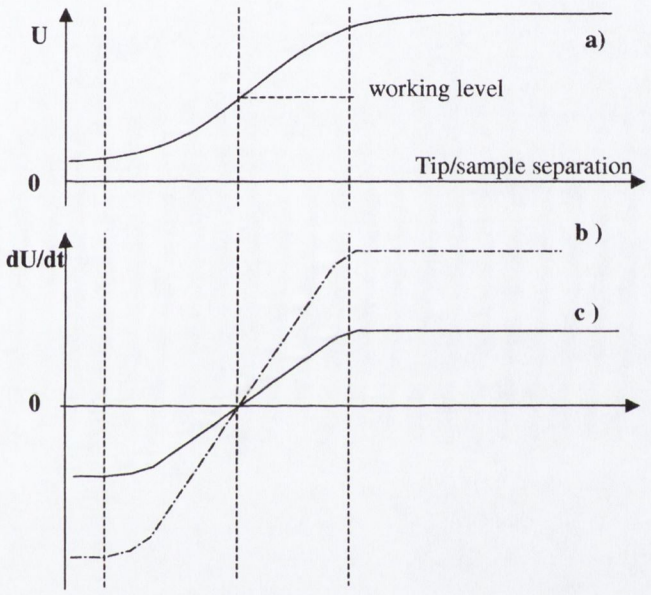

Figure 5.4: Principle of the feedback function: a) signal of the topography detector after lock-in detection; b),c) velocities of probe motion for various circuit gain, those signals are further integrated resulting in probe position signal.

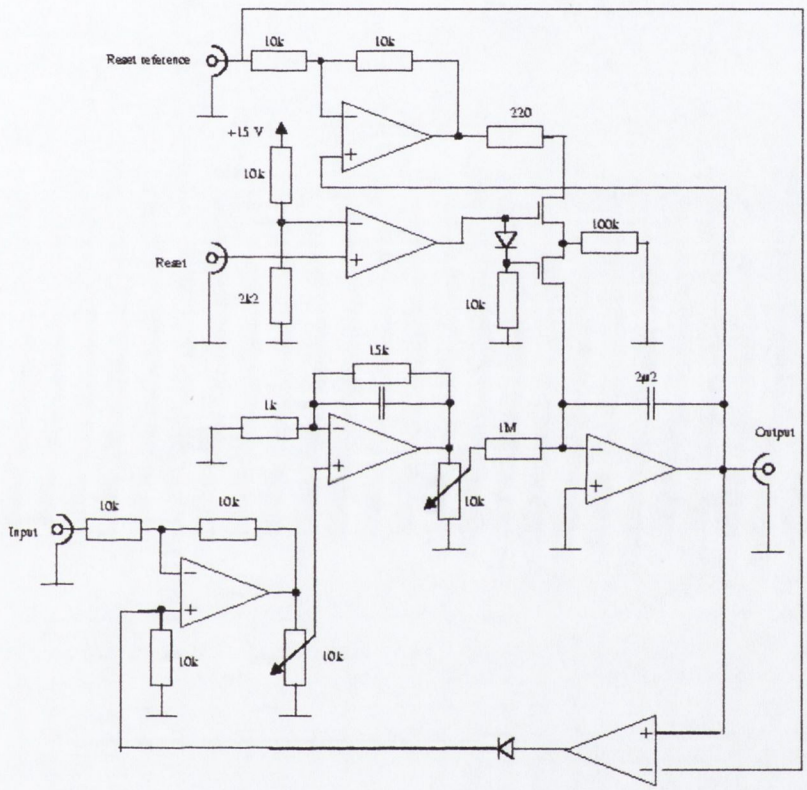

Figure 5.5: Schematics of the feedback amplifier. The potentiometers were in the final version replaced by the electronic multipliers to allow full software control.

From the user point of view, the scanning control program consists of several modules with various functionality:

- Manual control of the probe motion: The probes are driven using a keypad during the definition of the scanning area, for probe alignment relative to a reference point after their exchange and for the placement of the electric field antennas in the calibration unit.

- Measurement of the properties of SFM probes: This module allows one to measure the resonance frequency of the tuning fork system, the quality factor and the tip/sample approach curves. The measurement must be performed once for each probe and it is used to set the feedback parameters and the regime of the topography scanning.

- Topography acquisition module. It performs the topography scanning in defined area with user defined resolution - number of lines and number of points per line

- Field acquisition module: The electric intensity is measured with defined probe separation and offset. The bandwidth is automatically calculated to keep optimal system sensitivity with respect to the resolution and scanning velocity.

- Calibration of the electric probes: The sensitivity constant is calculated according to the probe position in the calibration unit and induced field.

- Data management module. Saves and loads the data files and allow their basic manipulation (multiplication with a calibration constant, their summation/differentiation for use with PD method and acquisition of tangential components)

- Primary data visualization for better user orientation in acquired data sets

The separate data visualization program implements additional data manipulation features such as:

- Cursor enabled inspection of the measured data for particular point of the scan
- Generation of the scan cross-sections
- Saving the PostScript images of the data
- Generation of 3D VRML (Virtual Reality Modeling Language) images

Although not completely finished we believe that the program meets the basic requirements for our scanning measurements.

5.3 Scanning process

The scanning process consists of several steps. First the topography tip is manually driven to a reference point. A fixed sharp tip similar to our topography probes, the probe position is optically controlled under a long focus microscope during the probe motion. After setting the reference the topography is acquired using the parameters measured for particular tuning fork probe. The shear-force head is then exchanged for the field antenna which is again aligned relative to the reference. A number of scannings for various frequencies or probe/sample separation can be performed according to the same topography data set. Whenever the antenna is repositioned (i.e. rotated for acquisition of the tangential components of the field), the process of probe reference adjustment must be repeated.

Chapter 6

Topography acquisition

We have measured the precision of the probe displacement system of our set-up on various structures including semiconductor chips and various PCB structures. Both the shear-force and tapping mode probes were used, the tip apex size, its declination and scanning velocities vary with respect to the sample structure and scanning area.

For sharp probes the resolution achieved was mainly limited by precision of the positioning stages. Figure 6.1 shows a scan of an EPROM memory chip, the scanning area is 400 x 400 μm. The image was acquired by a perpendicular shear-force probe with velocity of about 10 μm/s, the horizontal image resolution was below 1 μm. As the changes of z-coordinate of the sample profile are several μm and does not exceed the range of the piezo, the whole probe vertical movement is performed by that piezo actuator - except for the probe approach and withdrawal at the beginning and end of each line. The precision of acquisition of vertical topography data is then mainly limited by unidirectional repeatability of the motorized stage for z axis.

A Lange coupler[1] (fig. 6.2) was measured with a rather blunt SF probe

[1]The coupler was manufactured by Thomson CSF Microelectronique, a partner of [76] project

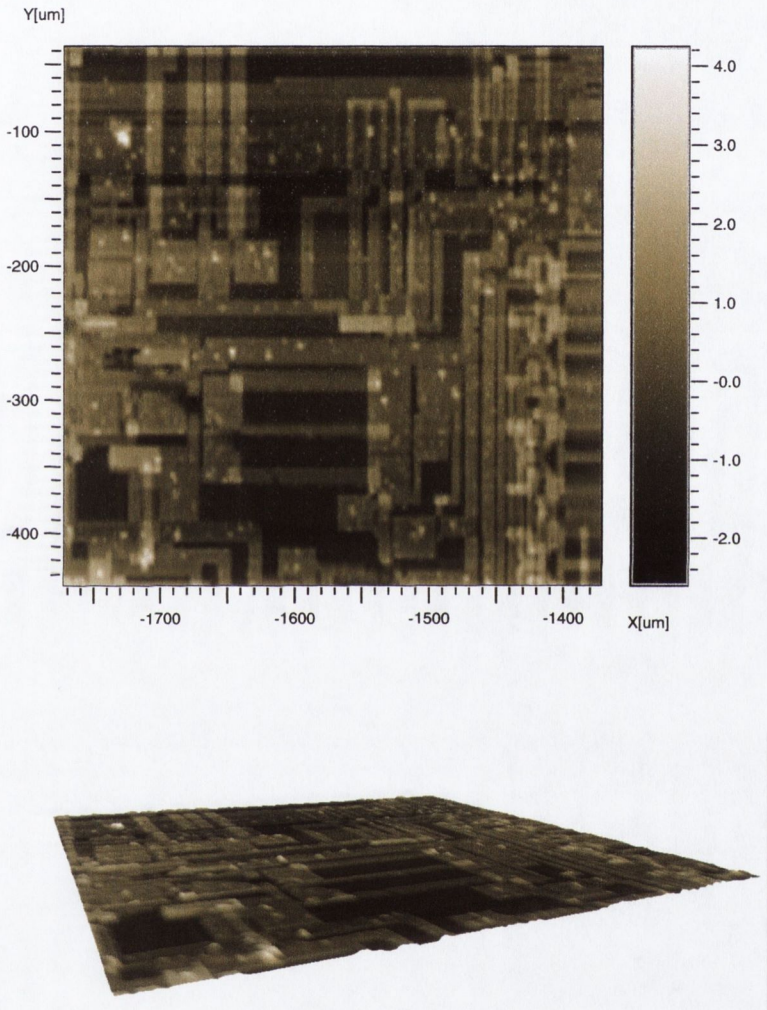

Figure 6.1: Topography scan of an EPROM memory and its 3D image. Scanned area 400x400μm.

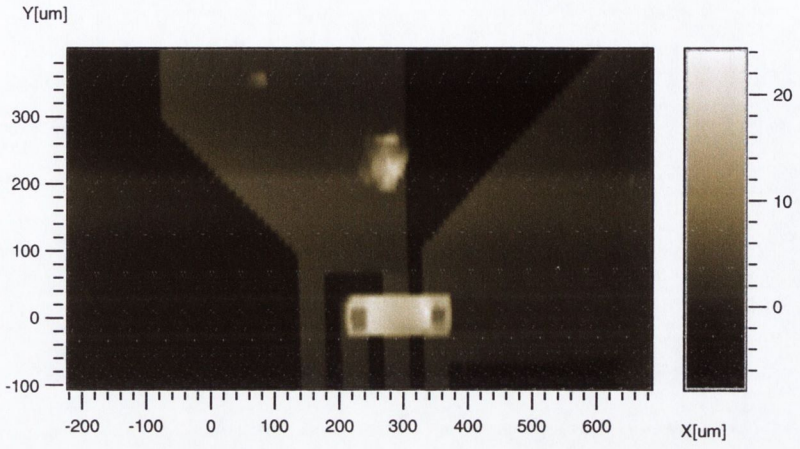

Figure 6.2: Topography of a Lange coupler

with tip apex radius of about 10 μm with relatively low velocity v =15 μm/s to avoid probe bending. The figure 6.3 shows the possibility of fast scanning of large samples with step-like features, the edges of resulting image (fig 6.3 b) are convoluted due to the large angle of tip declination (see section 3.5.2). Nevertheless this image distortion is acceptable as the influenced areas are much smaller than the lateral dimensions of the strips.

The last image - a scan of a PCB distributed filter (figure 6.4) - shows the importance of the topography acquisition before the field measurements. For this relatively large structures the tilt of the sample surface and its bending do not allow simple planar scanning with fixed antenna z-coordinate. Varying separation between the probe and the circuit would cause the probe to collide with the surface or cause degradation of the resolution at higher heights. This is the very reason why the sample profile is always acquired before the field measurements. The terraces, which can be observed at the right bottom corner of the image, are virtual artifacts of the backlash error of the motorized z-stage motion during the adjustment the stage position when the

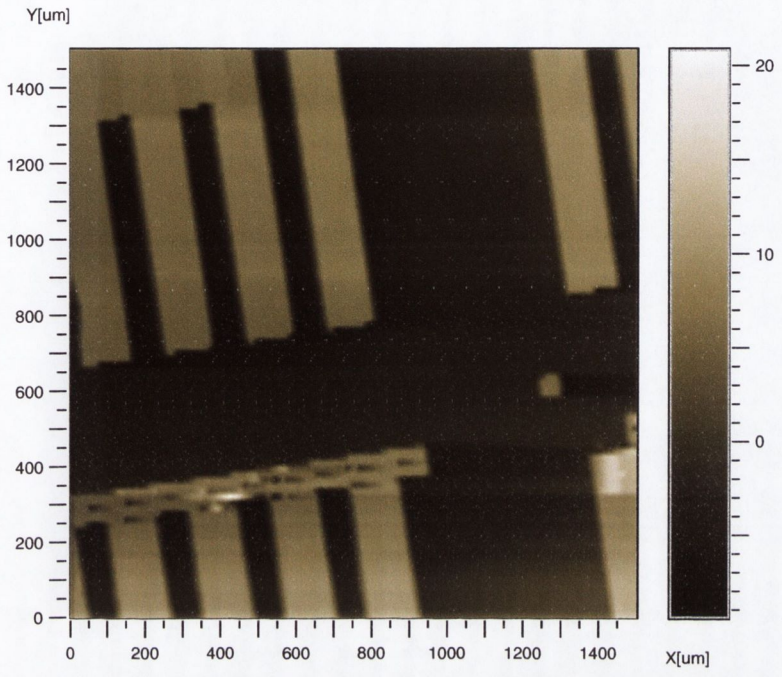

(a) Topography image

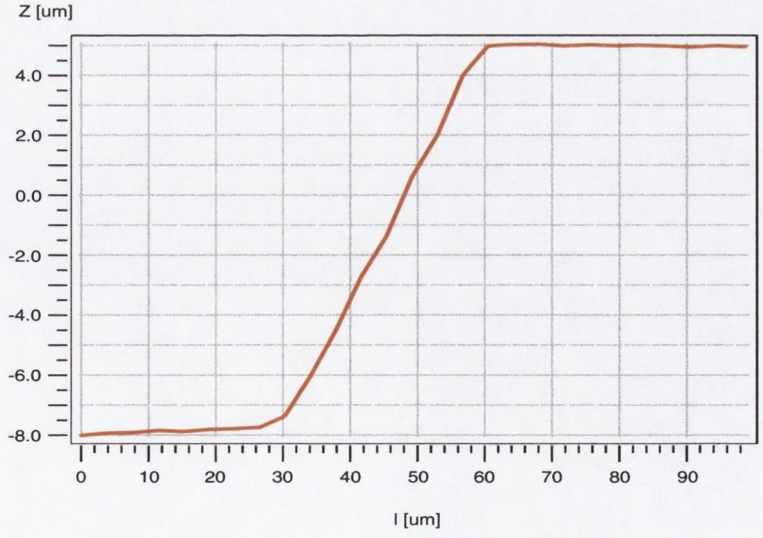

(b) Convolution of the step edge profile corresponds to the angle of the tip declination (70 degree)

Figure 6.3: Fast topography scanning of a silicon wafer with step structures.

piezo actuator is operating close to its limits. Because during field acquisition the stage operates in the same motion regime with the same backlash and the uncertaities in the antenna motion caused by the backlash are mostly compensated.

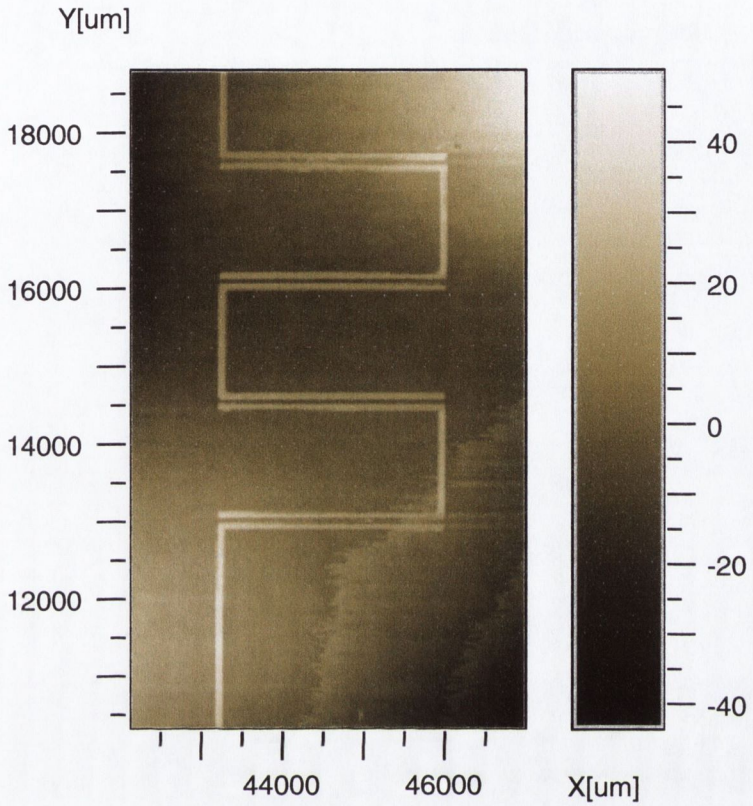

(a)

(b)

Figure 6.4: Topography of distributed PCB filter (a) and its 3D representation (b).

Chapter 7

Electric field intensity measurements

7.1 Testing of the position-difference method

7.1.1 Fields of a strip line

The basic structure on which we have tested the method was standard 50 Ω microstrip transmission line. We have prepared the line by standard lithographic techniques from a microwave PCB of 127 μm dielectric thickness, the copper strip conductor was 110 μm wide with thickness 17 μm. The signal was coupled from the RF output port of the vector network analyzer, the line was terminated by a 50 Ω load to avoid signal reflection. Figures 7.1 (a), (b) shows the signals acquired by a vertically placed antenna for two different distances of its apex from the sample - 40μm and 60μm, figure (c) shows their difference. We can observe a more narrow field image in (c) indicating the increase of the spatial resolution. The effect of resolution enhancement is even more visible on the figure 7.2 representing the signal distribution across

the strip.

Figure 7.3 compares calculated field intensity according to quasi-static strip model presented in section 2.2.3 with the calibrated antenna signal. We see general agreement of the character of the curves, nevertheless, there are two main differences:

1. The measured signal is stronger than would correspond to the calculated values

2. The image appears wider than the predictions for intensity distribution.

The difference for the magnitude of the field intensities is about 4.5 dB. There are several factors which probably caused this relatively large difference between measured and expected field intensities:

- Mismatch of the signal coupling between coaxial cable and the strip line and the impedance mismatch between the strip line and the terminal load. Measured value of signal reflection was -14 dB which corresponds to standing wave ratio SWR=1.5

- Uncertainties during measurement of the antenna sensitivity. Errors when determining the calibration coefficient might be caused by the mismatch of the signal to the calibration unit and also by its limited dimensions.

- Simplification of the theoretical model. For calculation of field intensities we have used quasi-static circuit model and we have assumes infinitesimal thickness of the conductor. Neglecting the thickness of the conductor also causes differences in the field close to the strip edges resulting in a slightly different width of the field pattern. As the maximum charge density is distributed along those edges any changes of

strip thickness will first influence the field in this area. The most appropriate approach would be a comparison of measured results with the full-wave solution of the circuit.

- Relatively large antenna displacement when compared to the antenna/sample separation. The field non-homogeneity at the antenna apex and direct capacitive coupling between antenna apex and the transmission line might also contribute to the differences between measured and calculated field.

7.1.2 Fields of a distributed PCB capacitor

To demonstrate the effect of resolution enhancement by the position-difference method we have prepared a planar capacitor using a similar PCB sheet as in previous case. The topography image of the structure is shown in figure 7.4. As the gap between the fingers is relatively wide (55 μm), the capacitance between them is small and represents rather low coupling between the poles[1]. The microwave signal source was plugged into the structure from the bottom side, the upper pole was connected to a 50Ω transmission line and was terminated by a load at a distance corresponding to electrical length of approximately $\lambda/4$ for frequency 4 GHz.

The input reflection coefficient S_{11} was measured for two different loads of impedances $Z_L = 50\Omega$ and $Z_L = 0\Omega$ (see fig. 7.5). We can observe that the reflection is relatively high, most of the signal is reflected back. The exception is the situation for the circuit operating at a frequency of about 3.85 GHz with a short load plugged at the line termination. In that case the transmission line operates at its resonance: its electrical length corresponds to phase shift

[1]The structure should be rather represented by three capacitors as the poles have relatively high capacitance relative to the grounding

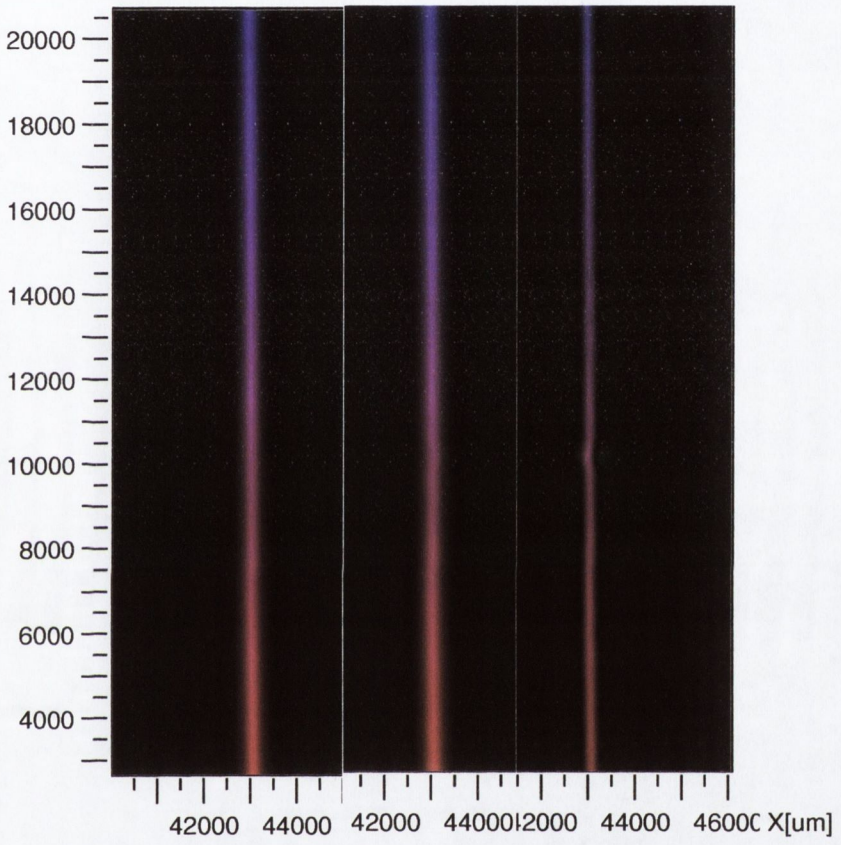

(a) (b) (c)

Figure 7.1: Electric field of a microstrip transmission line. Figures (a), (b) represent signals acquired for 40μm and 60μm, figure (c) is their difference. There is also a small structure defect (approximately at the line center) revealed by the subtraction of images.

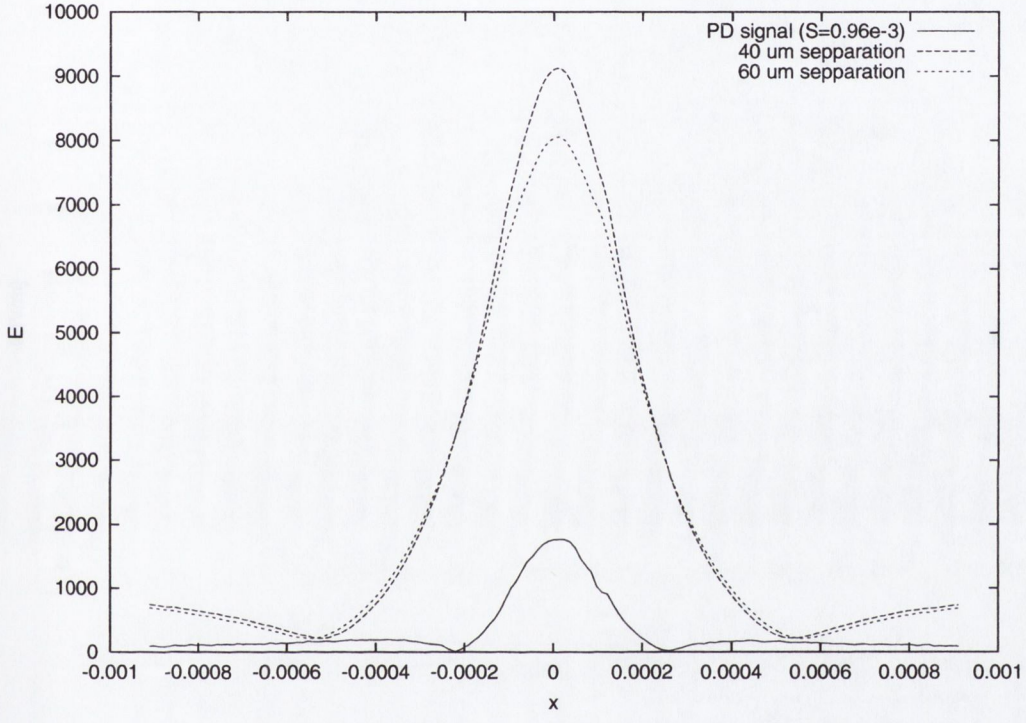

Figure 7.2: Distribution of the signals across the microstrip

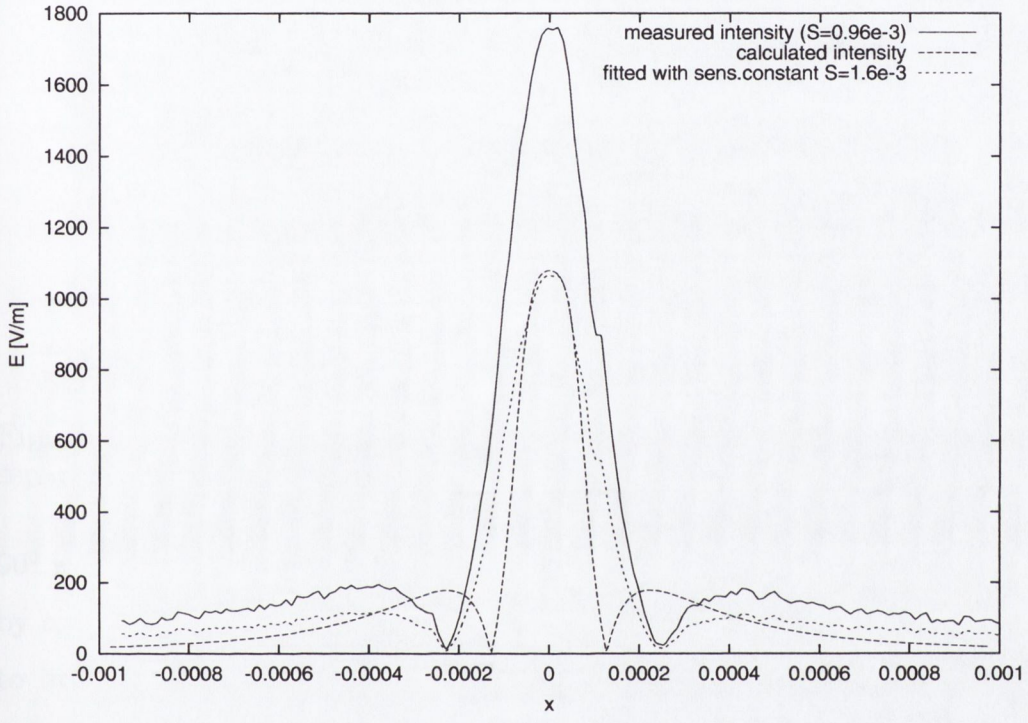

Figure 7.3: Comparison of the measured field with calculated electric intensity

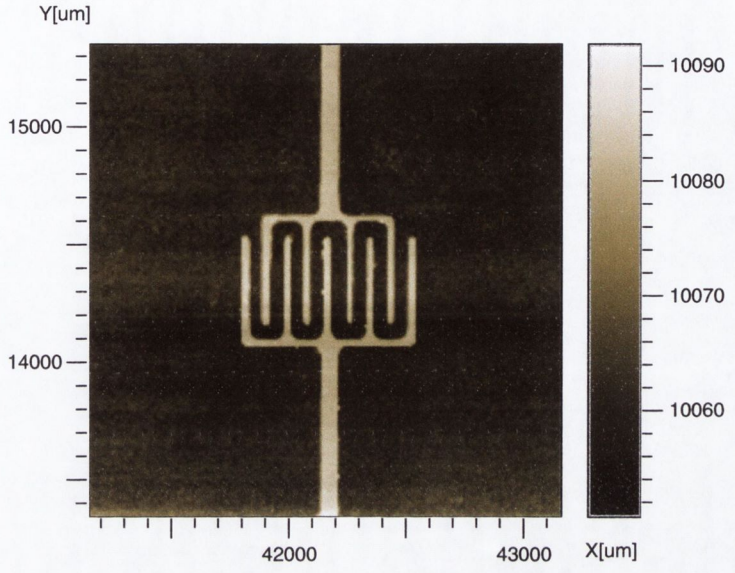

Figure 7.4: Topography of the capacitor. The width of the fingers is 45 μm, separation gap between them is about 55 μm.

90° with one open and one short end. The energy dissipation is caused mainly by resistive connection close to the short load (this impedance was measured to be about 3Ω) where the currents are high and also by radiation of the excited line.

The field presented in figure 7.6 was acquired for two different probe/sample separations - 5 μm and 12 μm (a,b) above the structure excited at its resonance. We can clearly observe significant resolution enhancement for the difference signal in figure (c). This difference signal corresponds to the local electric intensity surrounding the antenna apex, the field background acting on the whole length of the protruding conductor is suppressed. The method also reveals the differences in the phase of electric field, this differences are indicated by different colors in the field map. The resolution enhancement is also illustrated in figure 7.7 (a) which represents cross-section $(A - A')$ of the

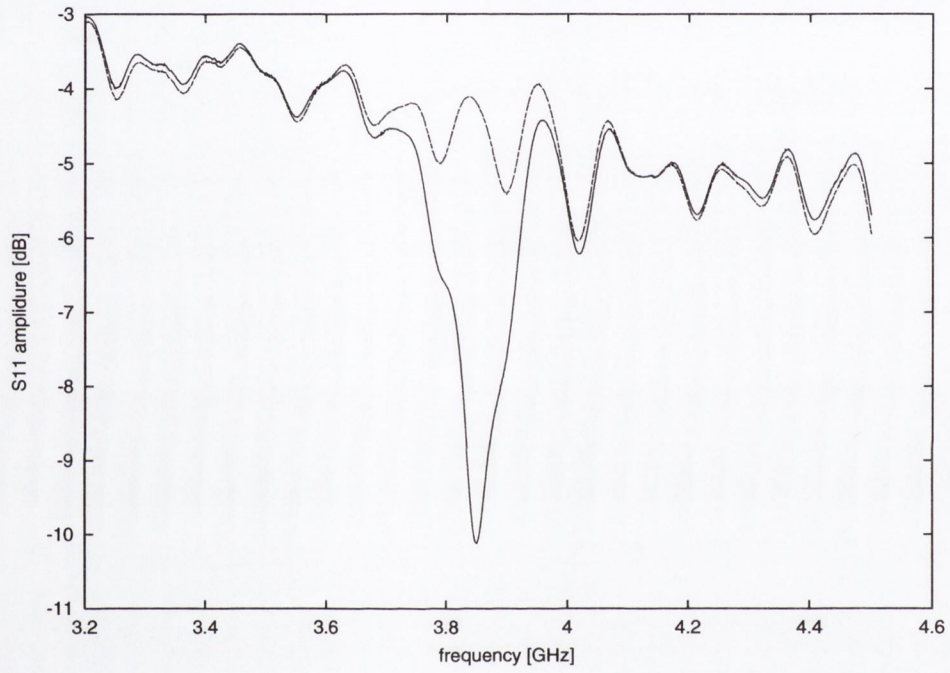

Figure 7.5: S_{11} scattering coefficient of the structure with a PCB capacitor

signal amplitude across the fingers of the capacitor. Figure 7.7 (b) exposes the phase difference of about 55° between fields surrounding fingers belonging to the two different ports of the capacitor. This phase difference is nearly indistinguishable for original full-length signals of the antenna.

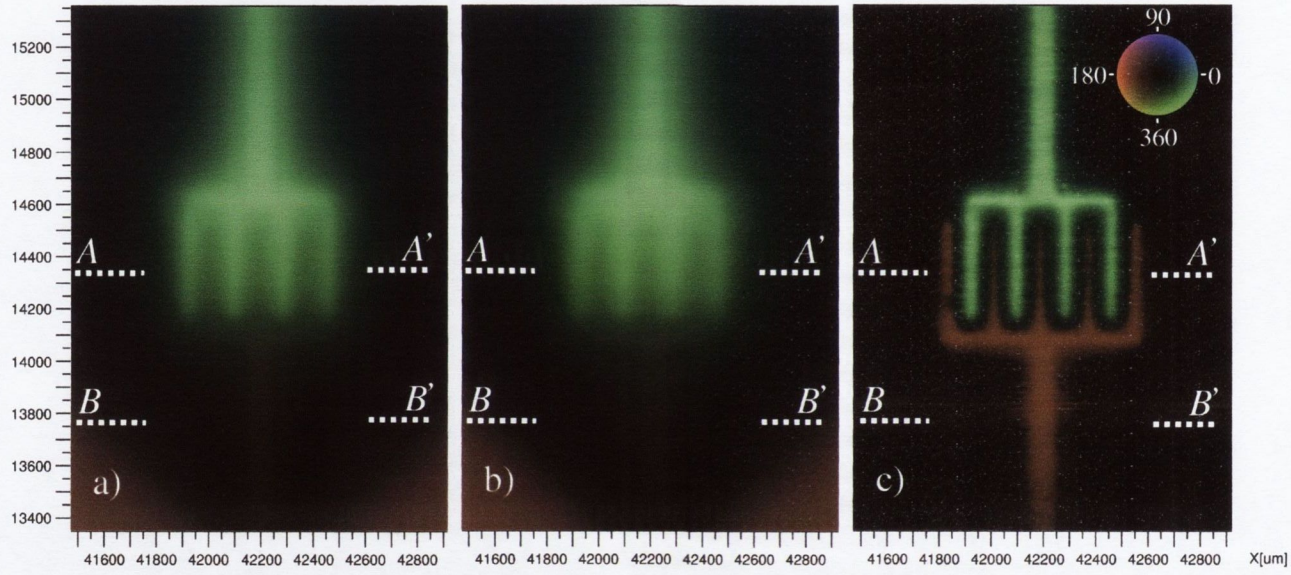

Figure 7.6: The effect of resolution enhancement as a result of signal differences acquired for different antenna/sample separation
a) Signal induced in the antenna for separation 5μm
b) Signal induced in the antenna for separation 12μm
c) Difference of signals (a) - (b)

The cross-section through the signal feeding transmission line $B-B'$ (Fig. 7.8) demonstrates the suppression of the field background acquired by the whole unshielded wire. This background field is induced by the presence of the strong field source - the large area of the capacitor operating at high potentials due to circuit excitation. The suppression of the background allows local field inspection close to the signal line which directly corresponds to the conductor charges and potentials. The last figure (Fig. 7.9) shows the field above the capacitor for non-resonant frequency 3 GHz with low signal coupling to the upper part of the circuit. The different color indicates the different phase shift for different frequency after the signal transmission through the coupling lines.

7.2 Acquisition of tangential field components

The tangential components in the figure 7.10 were acquired using a 45° inclined antenna using method described in section 4.4. The measurements were performed above a 50Ω microstrip with antennas at opposite directions perpendicular to the strip line. For each direction two measurements were performed with antenna displaced by 50 μm along its axis to measure the local field using PD method. Normal (a) and transverse (b) field components were calculated according to equation (4.15) as a sum and difference of the signals. The tangential components vanish at the line center, the phase at the line sides are shifted by 180 degree due to the opposite direction of the field vector.

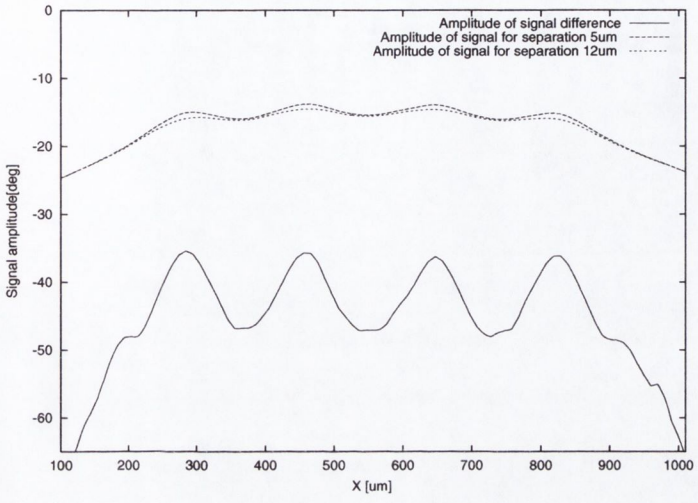

(a) $A - A'$

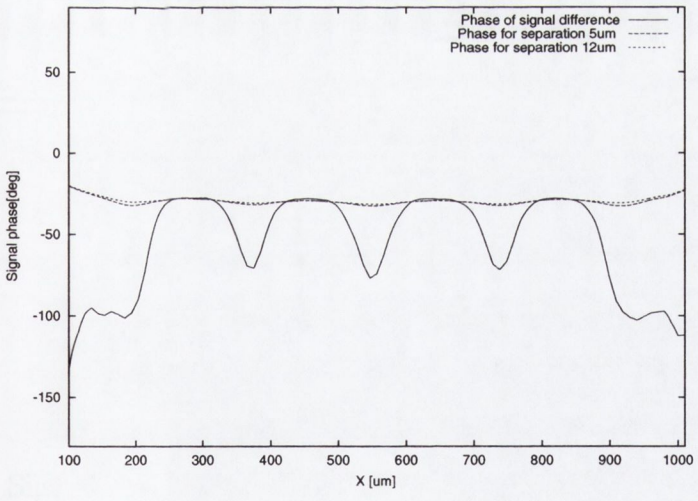

(b) $B - B'$

Figure 7.7: Signal intensities across the fingers of the capacitor. Increase in the amplitude (a) and the phase (b) contrasts using PD method

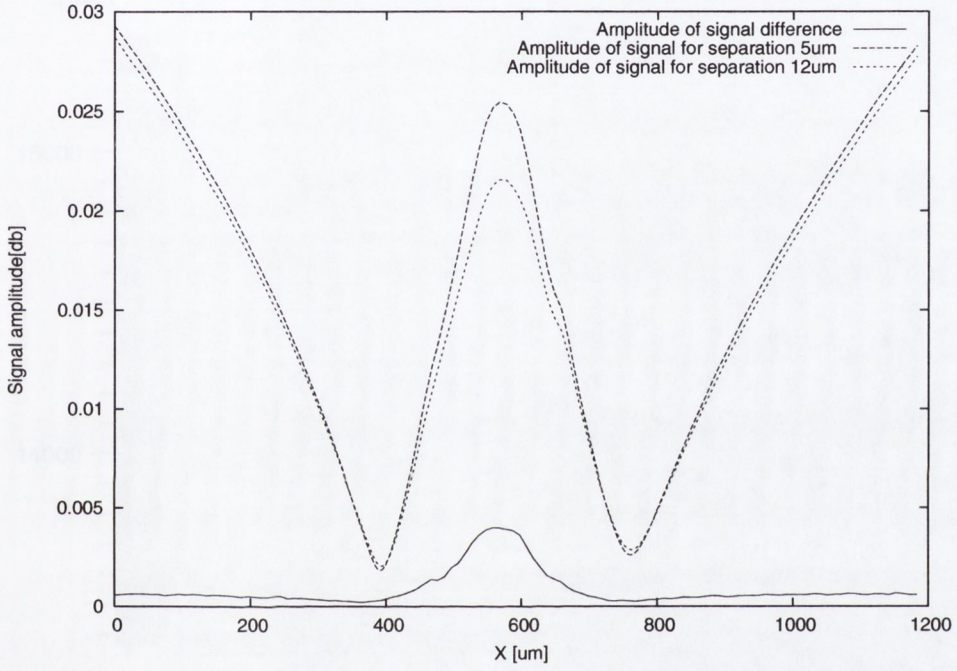

(a) $B - B'$

Figure 7.8: Signal intensities across the signal feeding line of the capacitor

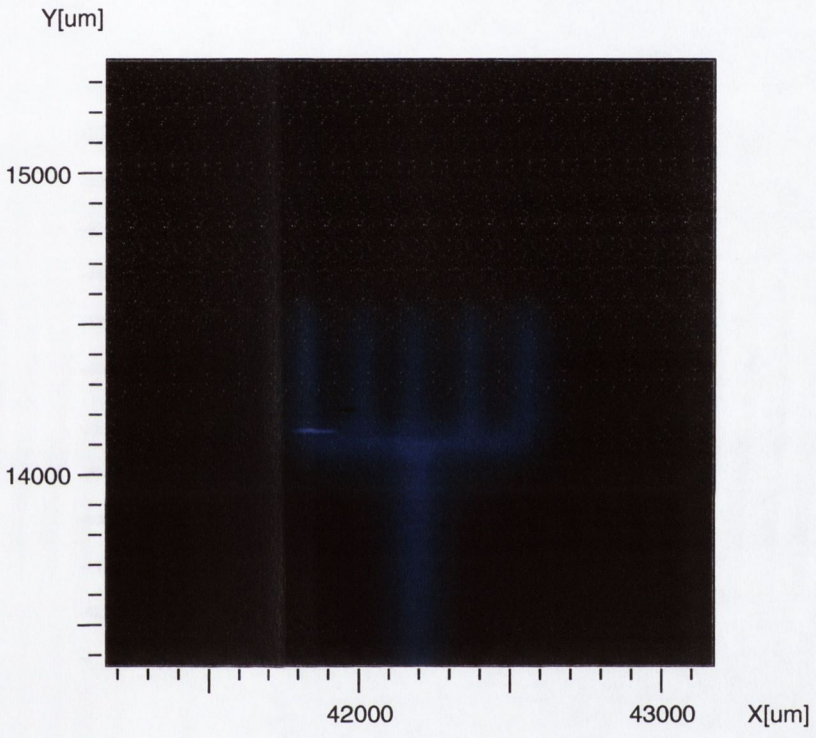

Figure 7.9: The capacitor fields for non-resonant excitation frequency f =3GHz. Due to low coupling between the poles, the signal transmission to the second part of the circuit is negligeable.

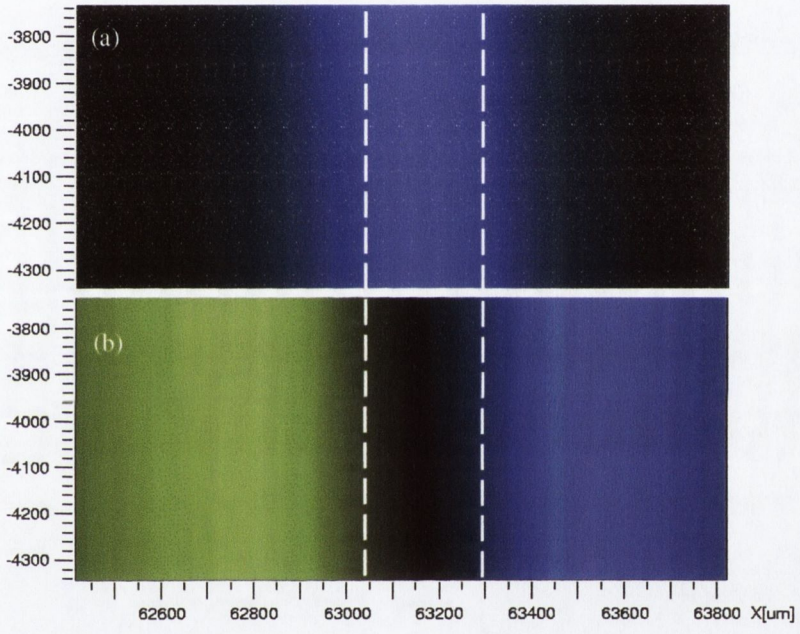

Figure 7.10: Normal (a) and x tangential (b) field components 600 μm above a 250 μm wide transmission line. The strip edges are highlighted by dashed lines.

7.3 Scanning of various samples

Microstrip filter

The next image (Fig. 7.11) represents the field distribution above a 3-stage microstrip filter for which the topography can be found in figure 6.4. The filter operates as a narrow band by-pass filter at frequency 7.45 GHz. For by-pass frequency the length of the strips corresponds to $\lambda/2$, the strips are excited at their resonance. Different colors at the ends of each strip illustrate the opposite phases of standing waves.

Large strip meander [77]

Although we were mostly focusing our attention on scanning of high resolution samples, the system was also capable to perform measurements over large areas. These large samples were scanned by traditional antennas without the use of position-difference method. The following meander represents a microstrip structure with certain filtering capabilities. Normal electric intensity was measured for two different frequencies - 5 and 10 GHz. We can see nearly perfect signal guiding for 5 GHz, the colors indicate phase change during the signal propagation. For 10 GHz - for which the meander size is comparable with the wavelength -the signal transmission between ports was attenuated by about 12 dB. The structure for that frequency spreads the field in relatively large area.

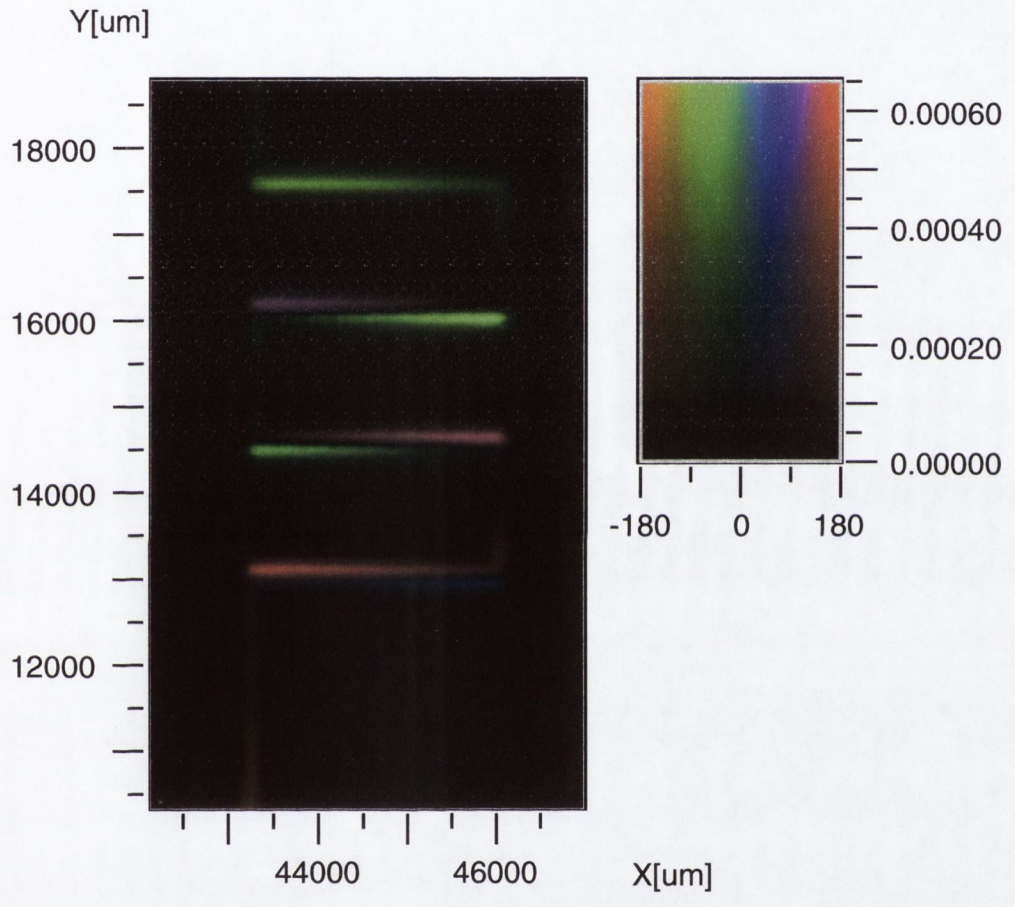

Figure 7.11: Microstrip filter. Normal component of electric field intensity at a distance of approx. 30 μm (difference of the signals at 20 and 40 μm) above circuit. The attenuation for the by-pass frequency 7.45 GHz is about -4 dB.

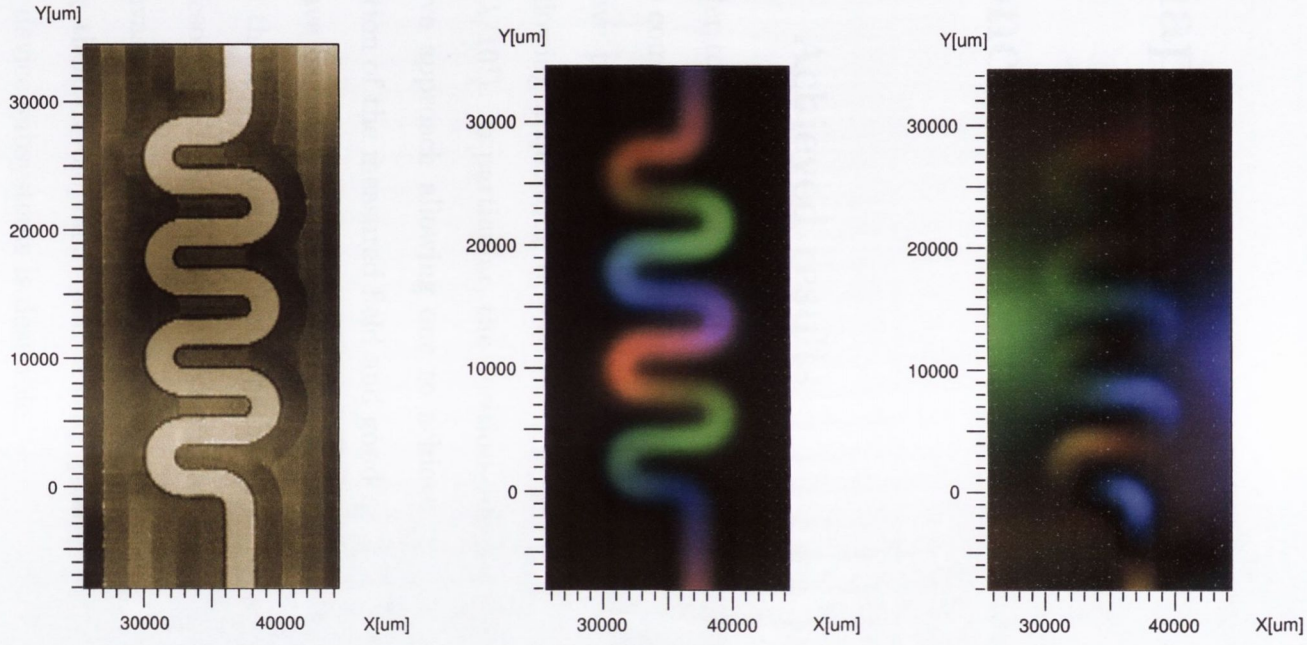

(a) Topography (b) 5 Ghz (c) 10 GHz

Figure 7.12: Microstrip meander. Line width is 2mm, scanning was performed for separation 0.5mm from the sample surface. The line was terminated by a 50Ω load (at the top of the images)

Chapter 8

Conclusion

8.1 Achieved results

In order to measure electric field intensities with high resolution a scanning set-up combining topography and microwave field acquisition was developed. We have presented miniaturized field probes and new measurement methods allowing acquisition of electric field intensity in the deep near-field region ($\lambda/10^4$). In particular, the position-difference method appears to be an effective approach allowing one to achieve exceptional resolution with low distortion of the measured field and good quantitative field characterization. We have tested the methods on some standard PCB circuits, the results indicate the high potential of the method for practical use. We believe that high resolution near-field measurement can become an attractive method for non-invasive investigation functionality of the microwave devices, especially during their development and testing phase, when maximum information about device subsystems is desirable.

The project by its nature contains a lot of development of new instrumentation. We have used some of the techniques of scanning probe microscopy

and adopted them for incorporation into our system. Many improvements presented in the work - such as the single-oscillating design and touching mode oscillation coupling, self-oscillation plug-in of the tuning fork with simple separation of the excitation/response signals - can be successfully adopted in these related fields.

8.2 Further work and improvement of the developed methods

In the future we would like to perform more testing of the measurement set-up, especially on active microwave circuits such as MMIC amplifiers. Although the results indicate that the measurement set-up have the capability to achieve a resolution of below 10 μm, further development would require additional miniaturization of the field probes with a diameter of the active antenna wire below 8 μm. Incorporation of independent position sensors in a feedback to control probe motion would allow one to avoid some uncertainties caused by mechanical limits of the displacement system and to increase the precision of the probe motion.

The scanning set-up in its recent configuration is only capable of measuring the microwave devices without shielding cases. Because the absence of the case may significantly change the working regime and the field distribution of the device, incorporation of the circuit shielding case during the measurement process would be desired. Unfortunately the case limits the access of the probes and special covers with small holes for the probes or movable shielding lids have to be designed for eacch particular microwave device.

Although we have focused our attention on acquisition of the electric field

components, the scanning set-up and most of the described techniques may also by used for magnetic field measurements by utilizing small loop antennas. Such measurements would give us complementary information about current sources of the device being tested.

Appendix A

Components of the scanning system

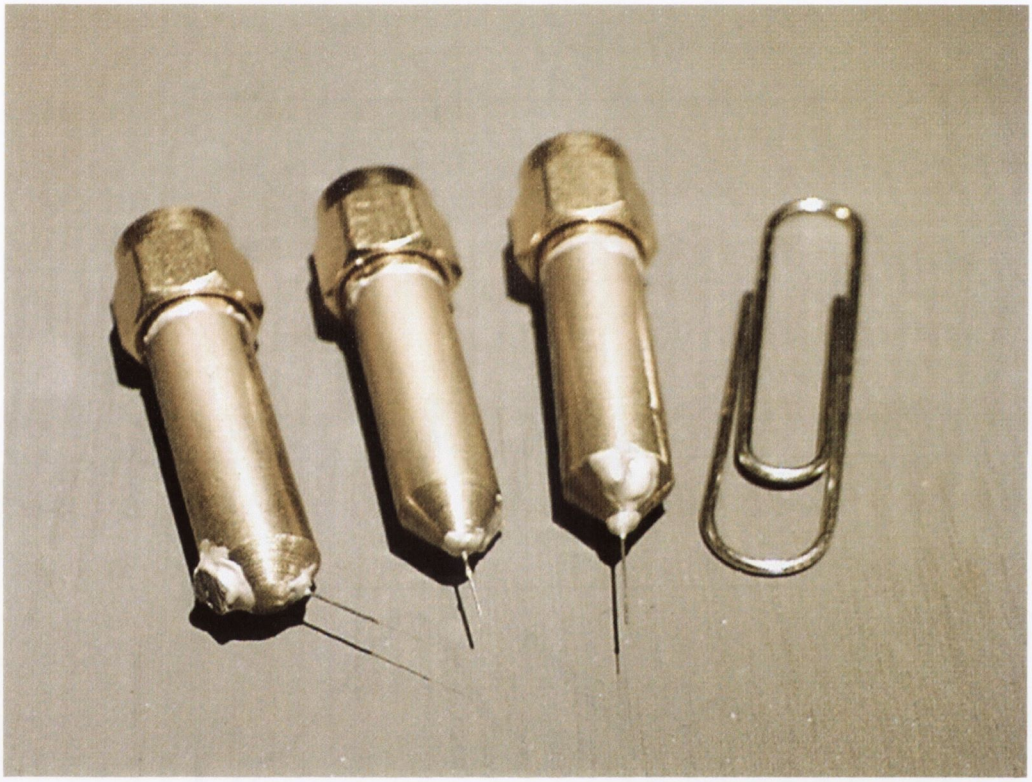

Figure A.1: Various antennas including configuration for tangential component measurements (left)

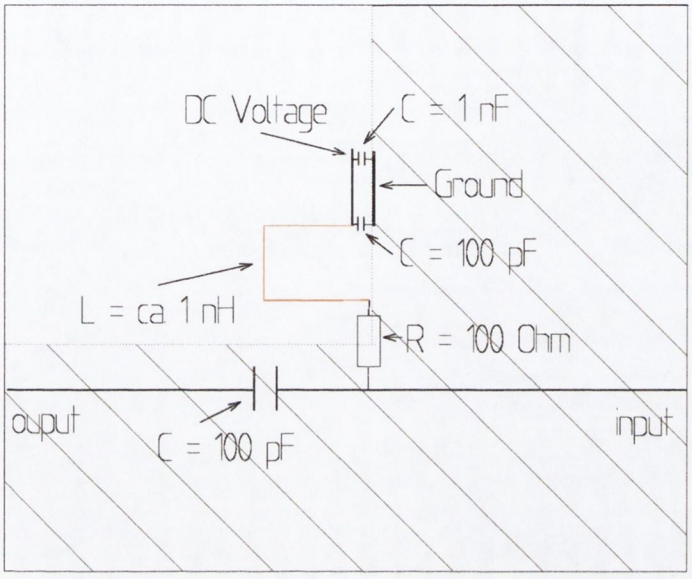

(a) Bias coupler outline

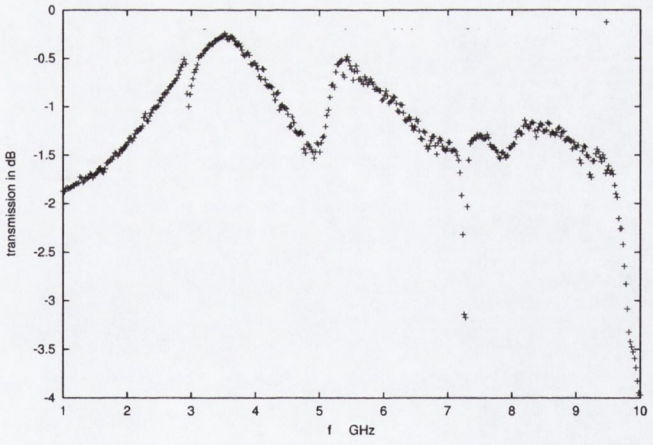

(b) Bias coupler S_{21} transmission

Figure A.2: Bias coupler design

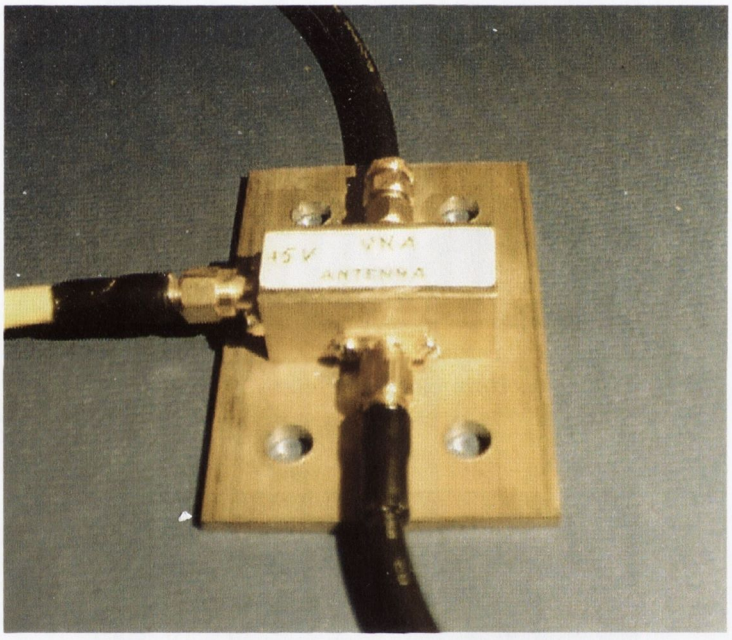

Figure A.3: DC bias coupler

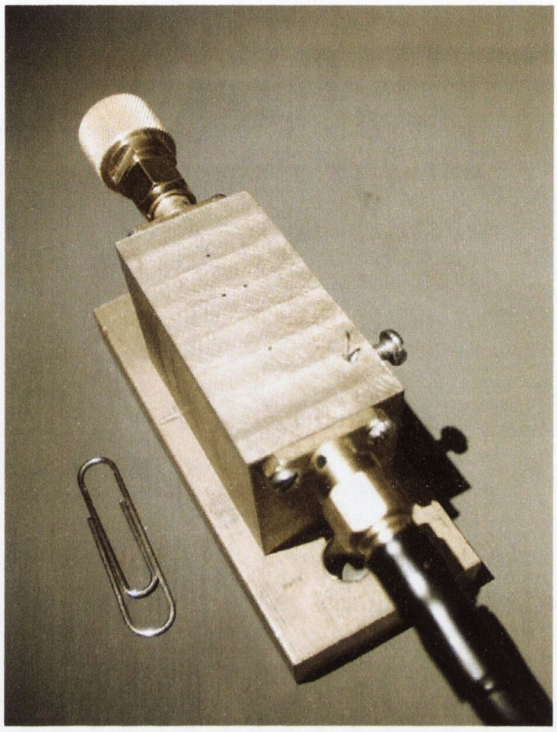

(a) Coaxial line configuration

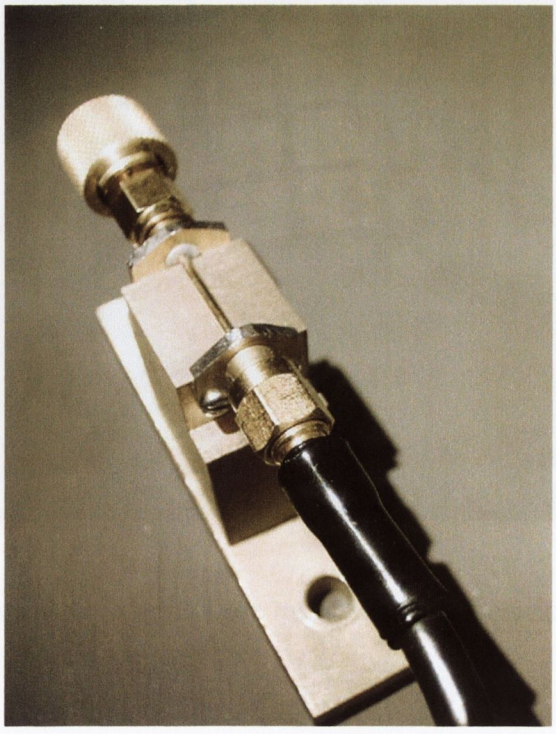

(b) An air-suspended line configuration

Figure A.4: Calibration units

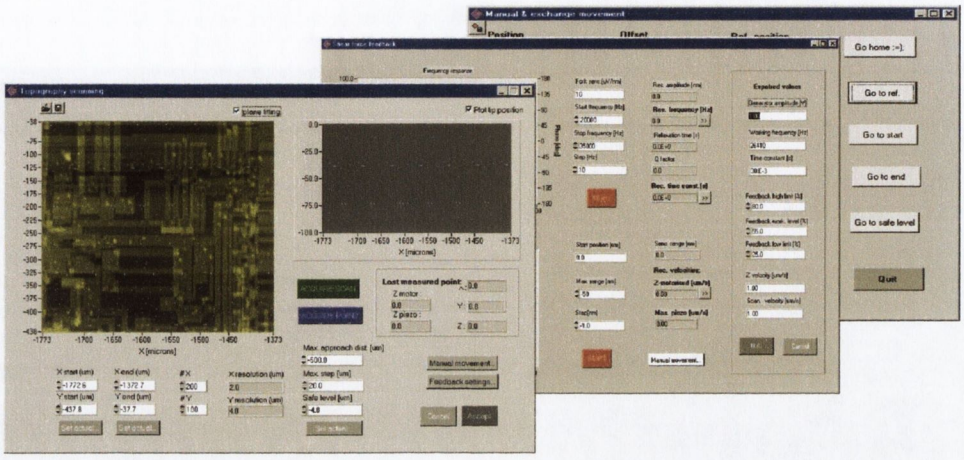

Figure A.5: User interface of scanning control software

Figure A.6: Keypad for manual probe positioning

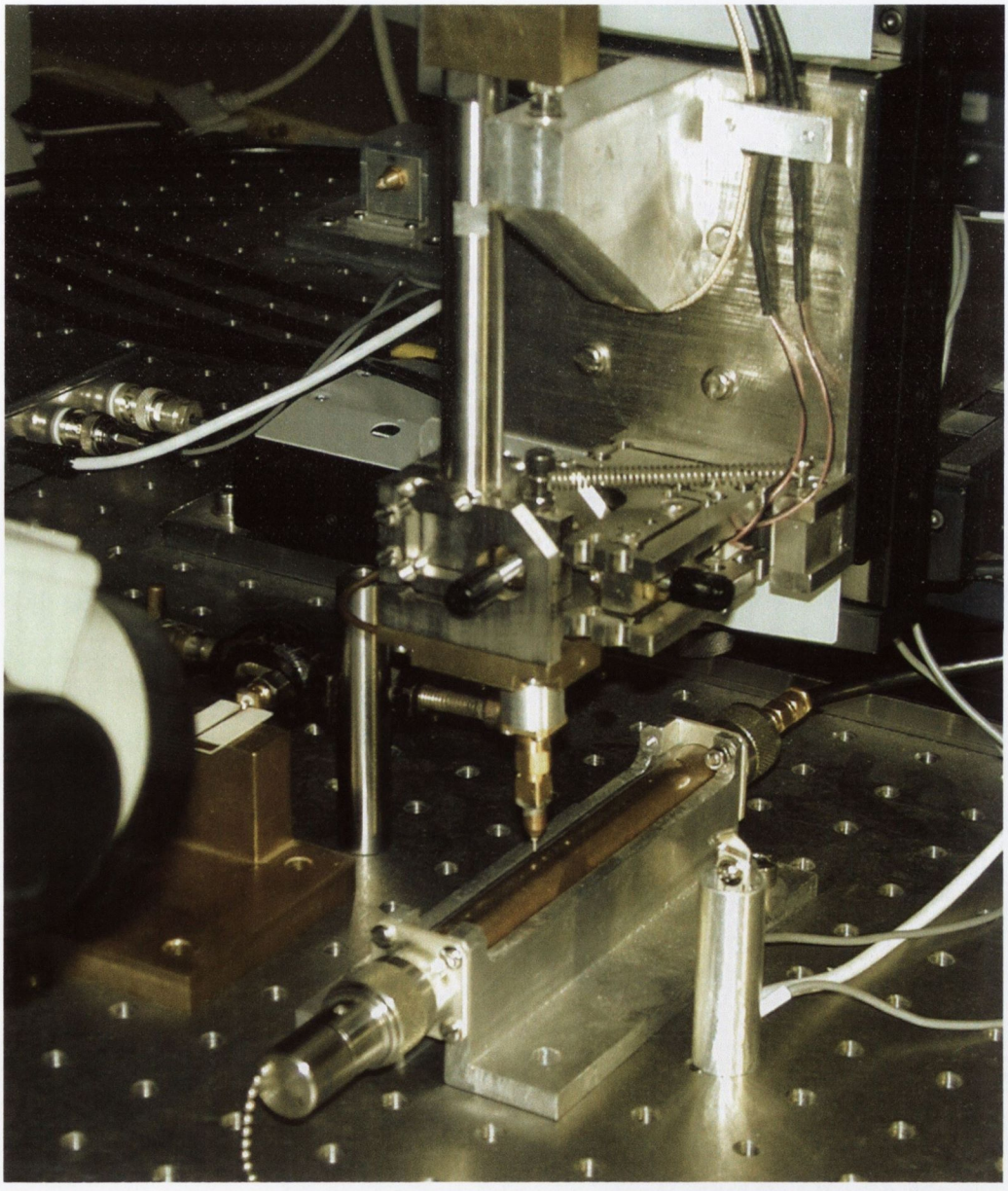

Figure A.7: Scanning set-up

Bibliography

[1] Dahele J. S., Cullen A. L., IEEE Trans. Mic. Theory Tech. 28 (7), p. 752

[2] Spreitzer W., Herzer E., Fassler G., Landstorfer F. M., Proceedings of the COST 243 Workshop, Paderborn, p. 53

[3] Ash E. A., Nicholls G., Nature, Vol 237, p. 510

[4] Islam N. M., Zhao X. K., Said A., Mickel S., Vail C. F., Appl. Phys. Lett. 71(20), p. 2886

[5] Bae J., Okamoto T., Fulii T., Mizuno K., Appl. Phys. Lett 71(24), p. 3581

[6] Koglin J., Fisher U. C., Fuchs H., Physical Review B 55(12), p. 7977

[7] Yatsui T., Kourogi M., Ohtsu M., Appl. Phys. Lett. 71(13), p. 1756

[8] Yatsui T., Kourogi M., Ohtsu M., Appl. Phys. Lett. 73(15), p. 2090

[9] Fee M., Chu S., Hashsch T. W., Opt. Commun. 69, p. 219

[10] Wei T., Xiang X.-D., Wallace-Friedman W. G., Schultz P. G., Appl. Phys. Lett. 68. p_3506

[11] Nozokido T., Bae J., Mizuno K., IEEE Trans. Mic. Theory Tech. 49 (3), p. 491

[12] Golosovsky M., Lann A., Davidov D., Ultramicroscopy 71, p. 133

[13] Fee M., Chu S., Hansch T. W., Opt. Commun. 69, p._219

[14] Dutta S. K., C. P. Vlahacos, D. E. Steinhauer, A. S. Thanawalla, Feenstra B. J., Wellstood F. C., Anlage S. M., Appl. Phys. Lett. 74 (1), p. 156

[15] Gao J., Lauder A., Ren Q., Wolf I. IEE Trans Mic Theory Tech 46 (11), p. 1694

[16] Gao Y. J., Wolf I., IEEE Trans. Mic. Theory Tech. 44, p. 911

[17] Agrawal V., Neuzil P., van der Weide D. W., Appl. Phys. Lett. 71 (16), p. 2343

[18] Budka T. P., Waclawik D., Rebeitz G. M., IEEE Mic. Theory tech. Symp. proceedings (1996), p. 1703

[19] Budka T. P., Tentzeris M., Scott D., Waclawik D., Dib N. I., Katehi L. P. B., Rebeitz G. M. Microwave Journal March 98, p. 94

[20] Yang K., Marshall T., Forman M., Hubert J., Mirth L., Popovic Z., Katehi L. P. B., Whitaker J. F., IEEE Trans. Mic. Theory Tech. 49 (5), p. 849

[21] Kramer A., Kielmann F.,Knoll B., Guckenberger R., Micron **27** (6), p. 413

[22] Lann A. F., Golosovsky M., Davidov D., Appl. Phys. Lett. 73 (19), p. 2832

[23] Vlahacos C. P., Steinhauer D. E., Dutta S. K., Feenstra B. J., Angale Steven M., Appl. Phys. Lett. 72 (14), p. 1778

[24] Duever Fred, Gao C., Takeuchi I., Xiang X.-D., Appl. Phys. Lett. 74 (18), p. 2696

[25] Steinhauer D. E., Vlahacos C. P., Dutta S. K., Wellstood F. C., Anglage Steven M., Appl. Phys. Lett 71 (12), p. 1736

[26] Knoll B., Keilmann F., Kramer A., Guckenberger R., Appl. Phys. Lett. 70 (20), p. 2667

[27] Chang K., Handbook of Microwave and Optical Components, John Wiley & Sons Inc., New Your 1989

[28] Stutzman W. L., Thiele G. A., Antenna theory and Design, John Wiley & Sons Inc., New Your 1998, p. 19

[29] Vanderlinde J., Classical Electromagnetic Theory, John Wiley & Sons, New York 1993, p. 179

[30] Chang K., Microwave solid-state circuits and applications, John Wiley & Sons, 1994, New York, chaprer 2

[31] Truncer E., Neikirk P., IEEE Microwave and Guided Wave Lett. 2, p. 409

[32] Bahl I. J., Bhartia, Microwave solid state circuit design, John Wiley & Sons, New York, 1988

[33] Edwards T.C., Foundation of Microstrip Circuit Design, John Wiley & Sons, New York, 1987

[34] More J., Pizer R., Moment methods in Electromagnetics, Research Studies Press Ltd., Lethworth England and Wiley New York, 1984

[35] Vlahacos C. P., Black R. C., Anlage S. M., Amar A., Wellstood F. C., Appl. Phys. Lett 69(21), p. 3272

[36] Williams C.C., Hough W. P., Rishton Appl. Phys. Lett. 55, p. 203

[37] De Wolf P., Geva M., Hantschal T., Vandervorst W., Bylsma R., Appl., Phys., Lett.73, p. 2155

[38] Wiesendanger R., Scanning probe microscopy and spectroscopy, Cambridge University Press, Cambridge, 1994

[39] Wolff Edwadr A., Antenna analysis, Artech House Inc., Nordwood, 1988

[40] Harrington R. F., Field computation bu moment methods, Macmillian 1968

[41] Betzig E., Finn P. L., Weiner J. S., Appl. Phys. Lett. 60 , p. 2484

[42] Toledo-Crow R., Yang P. C., Chen Y., Varez-Iravani M., Appl. Phys. Lett. 60, p. 2957

[43] C. Durkan, I.V. Shvets, Appl. Optics 36 (1997) 8173.

[44] Vaez-Iravani M., Toledo-Crow R., Appl. Phys. Lett. 62 , p. 1044

[45] Pfeffer M., Lambelet P., Marquis-Weible F., Rev. Sci. Instrum. 68, p. 4478

[46] Karrai K., Grober R. D., Appl. Phys. Lett. 66, p. 1842

[47] Zhu X., Huang G. S., Zhou H. T., Dai Y. D., Solid State Commun. 98, p. 661

[48] Brunner R., Bietsch A., Hollrichter O., and Marti O., Rev. Sci. Instrum. 68, p. 1769

[49] Leong J. K., Williams C. C., Appl. Phys. Lett. 70, p. 1500

[50] Hsu J. W., Lee M., Deaver B. S., Rev. Sci. Instrum. 66, p. 3177

[51] Lee M., McDaniel E. B., Hsu J. P., Rev. Sci. Instrum. 67, p. 1468

[52] Kelly S. G., Fundamentals of mechanical vibrations, McGraw Hill, New York 1993

[53] Tsai D. P., Yuan Y. L., Appl. Phys. Lett. 73 , p. 2724

[54] Kantor R., Lesnak M., Beredunov N., Shvets I. V., Appl. Surf. Sci 144-146, p. 510

[55] C. Durkan, I.V.Shvets, J. Appl. Phys. 80, p. 5659.

[56] Gregor M. J., Blome P. G., Schöfer J., Ulbrich R. G., Appl. Phys. Lett. 68, p. 307

[57] Bozhevolnyi S., Smolyaninov I. I., Keller O., Appl. Opt. 34, p. 3793

[58] Durkan C., Shvets I. V., J. Appl. Phys. 79, p. 1219

[59] Davy S., Spajer M., Courjon D., Appl. Phys. Lett. 73, p. 2594

[60] Salvi J., Chevassus P., Mouflard A., Davy S., Spajer M., Courjon D., Hjort K., Rosengren L., Rev. Sci. Instrum. 69, p. 1744

[61] Durkan C., Reflection mode Scanning Near-Field Optical Microscopy, PhD Thesis, Trinity College, Dublin 1996

[62] SNOM Aurora-2, Topometrix (http://topometrix.com)

[63] Wright O. B., Nishiguchi N., Appl. Phys. Lett. 71 , p. 626

[64] Cretin B., Stahl F., Appl. Phys. Lett. 62, p. 829

[65] Giessibl F. J., Appl. Phys. Lett. 73, p. 3956

[66] Hartmann U., Phys. Rev. B 43, p. 2404

[67] Wei C. C., Wei P. K., Fann W., Appl. Phys. Lett. 67, p. 3835

[68] Crystal Product Data Book 1997, IQD ltd.

[69] Chuang Y. H., Wang C. J., Huang J. Y., Pan C. L., Appl. Phys. Lett. 69, p. 3312

[70] Kraus J. D., Antennas, MsGraw-Hll Inc., New York 1976/1988

[71] Progress Report May 1998, EU-Project PL96-230

[72] MGA-86576, Agilent Technologies Semiconductor Products Catalog.

[73] Crawford M. L., IEEE Trans Magn. Comp., EM16

[74] MP 35E M-400 Series Operating Manual, Physik Instrumente,Waldbroon, Germany

[75] http://fltk.org

[76] EU-project contract SMT4-CT2189

[77] The sample was prepared by Mr Arcambal, Thomson SNCF, Toulouse.

Published papers

1. J. Pitora, D. Ciprian, R. Kantor, K. Postava, J. Sobta,Dark Mode Spectrocsopy of Magnetic Thin Films, J. Magn. Mag. Matter., vol. 157/158 (1996), p. 283-284.

2. R. Kantor, K. Postava, J. Pitora, Tuning of guided modes in magnetooptical Sandwiches, J. Magn Soc. Jpn, vol. 20, No. S1 (1996) p. 125-127.

3. R. Kantor, M. Lesnak, N. Berdunov, I. V. Shvets, Method of Increasing sensitivity of shear-force distance control for scanning near-field microscopy, Appl. Surf. Sci 1445-145 (1999) p. 510-513

Conference proceedings and digests

1. J. Pistora, D. Ciprian, R. Kantor, K. Postava, J. Sobota, Guided modes in three-layered sandwich structures, PIERS'95 (Progress in Electromagnetic Research Symposium) - Seatle, USA, Proceedings p. 696

2. R. Kantor, K. Postava, D. Ciprian, J. Pistora, Optics of anisotropic media: Jones 2x2 matrix method for description of multilayered structures, VSB-TU International conference 1995, Ostrava, Czech Rep., p. 49

3. Pistora, D. Ciprian, K. Postava, R. Kantor, Dark mode spectroscopy of magnetic thin films, VSB-TU International conference 1995, Ostrava, Czech Rep., p. 79

4. D. Ciprian, J. Pistora, K. Postava, R. Kantor, Light propagation in multilayered waveguides, Proceedings of ISAP 1996, Chiba, Japan, Vol. 3 p. 633

5. Pitora, R. Kantor , N. Negre, K. Postava, R. Anyzova, J. Seidl, Analysis of polarised light in multilayers, SPIE Proceedings, Vol. 3094, p. 25

6. K. Postava, J. Pistora, R. Kantor, A. R. Fert, Permeability tensor effect and light propagation in magnetically ordered ultrathin structures, PIERS '96 (Progress in Electromagnetic Research Symposium), Innsbruck, Austria, Proceedings p. 501

7. Pistora, D. Ciprian, R. Kantor, R. Anyzova, J. Seidl, K. Postava, P. Necka, Degenerate points and guided modes in magnetooptical waveguides, PIERS'97, Hong Kong, Proceedings p. 298.